

# Dynamic Modeling of Drug Transport in Solid Tumors and Optimal Chemotherapy Regimen

by

Mohammad Mohammadi

A thesis  
presented to the University of Waterloo  
in fulfillment of the  
thesis requirement for the degree of  
Doctor of Philosophy  
in  
Chemical Engineering

Waterloo, Ontario, Canada, 2015

© Mohammad Mohammadi 2015

I hereby declare that I am the sole author of this thesis. This is a true copy of the thesis, including any required final revisions, as accepted by my examiners.

I understand that my thesis may be made electronically available to the public.

## Abstract

One of the most common therapies for treatment of cancer patients is chemotherapy. Therapeutic agents (drugs) can kill cancer cells by damaging their DNA and interrupting their extensive proliferation. Successful chemotherapy depends on the injected drug dosages and their timings. A high dosage of the therapeutic agents is toxic to normal cells, whereas a low dosage leads to an unsuccessful treatment. Distribution of drugs within solid tumors and their efficacy depend on the drug biophysical properties as well as physiological properties of solid tumor under treatment; therefore, the chemotherapy regimen should be determined and personalized for a specific patient and drug. Finding the optimal scheduling of chemotherapy for a specific drug and tumor condition using clinical or preclinical studies is almost impossible, as many parameters are involved and examining all of them is costly and lengthy. Mathematical models, instead, can be used to overcome these limitations. The objective of this study is to introduce a method for finding the optimal chemotherapy regimen that can be applied to a wide range of tumor microenvironments. We first use transport phenomena equations such as Darcy's law, the continuity equation, and Starling's equation to model the fluid flow within a tumor microenvironment. Two main mechanisms of drug transport is convection and diffusion; thus, an advection-diffusion equation is utilized to calculate spatio-temporal distribution of chemotherapeutic drugs. Then, a novel algorithm is developed to calculate the distribution of fluid and drug within an ideal image of a solid tumor, in which the tumor boundary and vasculature are perfectly recognized. Using this computational framework, we study the effects of important features of tumor microenvironment such as microvascular density and vessel locations on the drug macromolecule distribution. Finally, built upon these computations, we develop an algorithm for finding the optimal regimen for injection of drug nanoparticles to a specific tumor microenvironment. Firstly, different drug delivery steps including traveling within blood vessels, penetration from vessel walls to tumor tissue, distribution within tumor tissue, binding to cancer cell receptors, and internalization within cancer cells are mathematically modeled. Then, an objective function is defined based on the efficiency of drug macromolecules in killing cancer cells. We use an optimization algorithm to find an optimal dosage regimen that maximizes the eradication of cancer cells over treatment period while satisfying specific constraints. Constraints are set to make sure the toxicity level of drugs is tolerable by the patient. This computational framework is applied to conventional chemotherapy and chemotherapy using drugs encapsulated in liposomes. Moreover, the efficacy of two delivery approaches, bolus injection and continuous infusion, when optimal dosages are applied is investigated.

## Acknowledgements

I would like to particularly thank my supervisor Professor Pu Chen for being a great supportive advisor. A very patient supervisor who grants his students a lot of freedom that cultivates creativity in them. He was an amazing teacher in navigating me passionately and patiently toward right goals throughout my PhD study. I would like to thank him for being such an incredible supervisor.

I am grateful to all members of my dissertation committee, Professor Brian Ingalls from Applied Mathematics Department, Professor Ali Elkamel and Professor Nasser Mohieddin Abukhdeir from Chemical Engineering Department, and Professor Argyrios Margaritis from Chemical and Biochemical Engineering Department at University of Western Ontario, for agreeing to be on my defence committee.

I take this opportunity to express my gratitude to all of the faculty and staff members at University of Waterloo, Chemical Engineering Department for their help and support and to make here such a wonderful environment to study and enjoy. I especially would like to thank Judy, Rose, Liz and Dennis. I would like to express my profound gratitude to Mary in Writing Center for all helps she gave me in editing my works.

Over past four years, my friends in University of Waterloo have made here a memorable place for me. I would like to thank them all for their support and friendship. Special thanks to Hamed and Javad!

Last, but not the least, I would like to thank my family. My special thanks to my mom and dad for their unconditional love and support. I would like to express my gratitude to my brother and sisters who have always helped and encouraged me. I am very blessed to have all of you in my life. Thank you all.

## **Dedication**

*To my parents, Zobeideh and Gholamabbas  
for their unconditional love and support  
I love you*

# Table of Contents

List of Tables	ix
List of Figures	x
Nomenclature	xv
<b>1 Introduction</b>	<b>1</b>
<b>2 Mathematical Modeling of Tumor Microenvironment and Transport of Drug particles</b>	<b>4</b>
2.1 Introduction . . . . .	4
2.2 Vascular network modeling . . . . .	7
2.3 Interstitial pressure calculation . . . . .	9
2.3.1 Method . . . . .	9
2.3.2 Results and Discussion . . . . .	13
2.4 Transport of drug molecules to a solid tumor . . . . .	18
2.4.1 Method . . . . .	18
2.4.2 Results and Discussion . . . . .	21
<b>3 Effect of Microvascular Distribution and its Density on Interstitial Fluid Pressure and drug distribution in Solid Tumors: A Computational Model</b>	<b>31</b>
3.1 Introduction . . . . .	31

3.2	Methods . . . . .	33
3.2.1	Vascular network modeling . . . . .	33
3.2.2	Transport of fluid and drug macromolecules . . . . .	34
3.3	Results . . . . .	36
3.3.1	Interstitial fluid pressure and macromolecule transport in a solid tumor	36
3.3.2	Effect of microvascular density on interstitial fluid pressure . . . . .	37
3.3.3	Effect of tumor size with constant MVD on IFP, IFV, and drug concentration distribution . . . . .	42
3.3.4	Effect of vascular location with constant MVD on IFP, IFV, and distribution of drug macromolecules . . . . .	44
3.4	Discussion . . . . .	47
3.5	Conclusions . . . . .	49
<b>4</b>	<b>Determination of Optimal Chemotherapy Dosage in Solid Tumors</b>	<b>50</b>
4.1	Introduction . . . . .	50
4.2	Tumor microenvironment model . . . . .	52
4.3	Case I: Optimal regimen of conventional chemotherapy . . . . .	53
4.3.1	Methods . . . . .	53
4.3.2	Results . . . . .	58
4.3.3	Discussion . . . . .	68
4.3.4	Conclusions . . . . .	70
4.4	Case II: Optimal regimen of liposomes . . . . .	71
4.4.1	Methods . . . . .	71
4.4.2	Results . . . . .	72
4.4.3	Discussion . . . . .	82
4.4.4	Conclusions . . . . .	84

<b>5 Summary and Future Works</b>	<b>86</b>
5.1 Summary . . . . .	86
5.2 Limitations . . . . .	88
5.3 Future work . . . . .	89
<b>APPENDICES</b>	<b>91</b>
<b>A Videos from Simulation Results</b>	<b>92</b>
<b>References</b>	<b>97</b>

# List of Tables

2.1	Physiological parameters used in the numerical simulation, as taken from [5]	14
2.2	Physical properties used in simulation, as taken from [5]	21
4.1	Model parameter values used in our computation	56
4.2	The value of parameters used in optimization problem	57
4.3	The optimal dosages (normalized to $u_{max}$ ) applied for bolus injections for different blood half-life values of drugs	59
4.4	The optimal dosages (normalized to $u_{max}$ ) applied for bolus injections for different drug diffusion coefficients	66
4.5	The optimal dosages (normalized to $u_{max}$ ) applied for bolus injections for different drug binding rates	68
4.6	Parameter values employed in model equations	72
4.7	The parameter values used in optimization problem	73
4.8	The optimal liposome dosages applied for bolus injections for different blood half-life values of drugs	82
4.9	The optimal liposome dosages applied for bolus injections for different liposome diffusion coefficients	82

# List of Figures

2.1	Schematic model of tumor microenvironment . . . . .	8
2.2	Vascular network with tumor and normal tissue for a lattice $30 \times 30$ . Vessels inside the tumor are red, in normal tissue are blue, and white space is tissue, both normal and tumorous . . . . .	9
2.3	Vascular flow rate (red) and transvascular flow rate (blue) for each vessel . . . . .	12
2.4	Generated adaptive mesh to solve IFP equation coupled with blood flow equation . . . . .	14
2.5	Blood pressure $P_V(mmHg)$ distribution within the vascular network . . . . .	15
2.6	Dimensionless IFP ( $P_i^*$ ) distribution within tumor microenvironment . . . . .	16
2.7	Interstitial fluid velocity ( $\mu m/s$ ) distribution in tumor and normal tissue . . . . .	16
2.8	Transvascular velocity ( $\mu m/s$ ) distribution in the network . . . . .	17
2.9	The intravascular velocity ( $\mu m/s$ ) distribution inside the network . . . . .	18
2.10	Dimensionless IFP $P_i^*$ for different values of $K, L_P, S/V$ . . . . .	19
2.11	Dimensionless concentration profile within the vascular network for continuous injection . . . . .	22
2.12	The distribution of maximum normalized concentration within the vascular network for continuous injection during 64 hours . . . . .	23
2.13	Dimensionless concentration gradient profile within the vascular network for continuous injection . . . . .	24
2.14	Dimensionless maximum concentration gradient profile within the vascular network for constant plasma concentration during 64 hours . . . . .	25
2.15	Dimensionless concentration profile within the vascular network for bolus injection of Fab drug . . . . .	26

2.16	Dimensionless maximum concentration of drug molecules for bolus injection of Fab drug during 64 hours . . . . .	27
2.17	maximum dimensionless concentration of drug molecules for bolus injection and different residence times during 64 hours . . . . .	27
2.18	maximum dimensionless concentration gradient of drug molecules for bolus injection and different residence times during 64 hours . . . . .	28
2.19	Maximum dimensionless concentration of drug molecules for continuous injection for different values of drug diffusion coefficient . . . . .	29
2.20	Maximum dimensionless concentration of drug molecules for continuous injection and for different values of tumor tissue hydraulic conductivity . . . . .	29
2.21	Maximum dimensionless concentration of drug molecules for continuous injection and for different values of vascular hydraulic conductivity . . . . .	30
2.22	Maximum dimensionless concentration of drug molecules for continuous injection and for different values of vascular permeability . . . . .	30
3.1	A typical solid tumor microenvironment surrounded by normal tissue and its vasculature. Blue lines are vessels in normal tissue and red lines are vessels within the tumor. . . . .	34
3.2	Adaptive mesh generated for the tumor model presented in Fig. 3.1. . . . .	36
3.3	(a) IFP and (b) IFV distribution for the tumor in Fig. 3.1. Arrows in (a) show the direction and magnitude of interstitial fluid flow. . . . .	37
3.4	Concentration profile of Fab drug within tumor microenvironment presented in Fig. 3.1 at different times. . . . .	38
3.5	Dimensionless maximum concentration profile within the solid tumor over 75 hours. . . . .	39
3.6	Tumors with different MVD values. The MVD values are: (a) 0.14, (b) 0.26, (c) 0.39, (d) 0.56, (e) 0.83, and (f) 0.99. . . . .	39
3.7	Maximum and average Dimensionless IFP for tumors with the same shape and size but different MVDs. . . . .	40
3.8	Maximum and average IFV ( $\mu m/sec$ ) for tumors with the same shape and size but different MVDs. . . . .	40
3.9	Average dimensionless concentration for tumors with different MVDs but the same shape and size. . . . .	41

3.10	Different tumor sizes with the same MVD, vascular network structure, and tumor shape. . . . .	42
3.11	Maximum and average dimensionless IFP for tumors with the same MVD, vascular network structure, and tumor shape but different tumor size. . . .	43
3.12	Maximum and average IFV ( $\mu m/sec$ ) for tumors with the same MVD, vascular network structure, and tumor shape but different tumor size. . . . .	43
3.13	Average dimensionless concentration for tumors with different tumor sizes but the same MVDs, shape and vascular structure. . . . .	44
3.14	(a)–(c) Tumors with different locations of vessels but the same MVD, tumor size and shape, (d)–(f) show IFP, and (g)–(i) show IFV ( $\mu m/sec$ ) distribution for each tumor. . . . .	45
3.15	Maximum and average dimensionless IFP distribution for tumors with the same size, shape and MVD but different vessel locations. . . . .	46
3.16	Maximum and average IFV ( $\mu m/sec$ ) distribution for tumors with the same size, shape and MVD but different vessel locations. . . . .	46
3.17	Average dimensionless concentration for tumors with the same size, shape and MVD but different vessel locations. . . . .	47
4.1	A typical tumor microenvironment, including solid tumor, normal tissue and vasculature. Vessels are blue in normal tissue and red within tumor. . . . .	53
4.2	Normalized concentration profile of free drugs ( $C_f^*$ ) when optimal bolus injections are applied; injection times ( <i>hour</i> ) are $t_i = \{0, 30, 60, 90, 120, 150\}$ . . . . .	60
4.3	Normalized concentration profile of bound drugs ( $C_b^*$ ) when optimal bolus injections are applied; injection times ( <i>hour</i> ) are $t_i = \{0, 30, 60, 90, 120, 150\}$ . . . . .	61
4.4	Normalized concentration profile of internalized drugs ( $C_{int}^*$ ) when optimal bolus injections are applied; injection times ( <i>hour</i> ) are $t_i = \{0, 30, 60, 90, 120, 150\}$ . . . . .	62
4.5	Fraction of killed cancer cells when optimal bolus injections are applied; injection times ( <i>hour</i> ) are $t_i = \{0, 30, 60, 90, 120, 150\}$ . . . . .	63
4.6	Results from optimal regimens for bolus and continuous infusion strategies . . . . .	64
4.7	Results from optimal regimens for different $\tau$ values of drugs: (a) drug normalized concentration within plasma, (b) drug normalized concentration within tumor tissue, (c) normalized concentration of bound drugs, (d) normalized concentration of internalized drugs, and (f) fraction of killed cancer cells . . . . .	65

4.8	Results from optimal regimens for different diffusivity values of therapeutic agents: (a) drug normalized concentration within plasma, (b) drug normalized concentration within tumor tissue, (d) normalized concentration of bound drugs, (e) normalized concentration of internalized drugs, and (f) fraction of killed cancer cells . . . . .	67
4.9	Results from optimal regimens for different binding rates of therapeutic agents: (a) drug normalized concentration within the plasma, (b) drug normalized concentration within tumor tissue, (d) normalized concentration of the bound drugs, (e) normalized concentration of the internalized drugs, and (f) fraction of killed cancer cells . . . . .	69
4.10	Normalized concentration profile of liposome nanoparticles ( $C_n^*$ ) when optimal bolus injections are applied; injection times ( <i>hour</i> ) are $t_i = \{0, 30, 60, 90, 120, 150\}$ .	74
4.11	Normalized concentration profile of free drugs ( $C_f^*$ ) when optimal bolus injections are applied; injection times ( <i>hour</i> ) are $t_i = \{0, 30, 60, 90, 120, 150\}$ .	75
4.12	Normalized concentration profile of bound drugs ( $C_b^*$ ) when optimal bolus injections are applied; injection times ( <i>hour</i> ) are $t_i = \{0, 30, 60, 90, 120, 150\}$ .	76
4.13	Normalized concentration profile of internalized drugs ( $C_{int}^*$ ) when optimal bolus injections are applied; injection times ( <i>hour</i> ) are $t_i = \{0, 30, 60, 90, 120, 150\}$ .	77
4.14	The fraction of killed cancer cells ( $1 - S_F$ ) when optimal bolus injections are applied; injection times ( <i>hour</i> ) are $t_i = \{0, 30, 60, 90, 120, 150\}$ . . . . .	78
4.15	Results from optimal regimens for bolus and continuous infusion strategies: (a) liposome concentration within plasma, (b) liposome concentration within tumor tissue, (c) concentration of free drugs, (d) concentration of bound drugs, (e) concentration of internalized drugs, and (f) fraction of killed cancer cells . . . . .	80
4.16	Results from optimal regimens for different $\tau$ values of liposome nanoparticles: (a) liposome normalized concentration within plasma, (b) liposome normalized concentration within tumor tissue, (c) normalized concentration of free drugs, (d) normalized concentration of bound drugs, (e) normalized concentration of internalized drugs, and (f) fraction of killed cancer cells . . . . .	81

4.17 Results from optimal regimens for different diffusivity values of liposome nanoparticles: (a) liposome normalized concentration within plasma, (b) liposome normalized concentration within tumor tissue, (c) normalized concentration of free drugs, (d) normalized concentration of bound drugs, (e) normalized concentration of internalized drugs, and (f) fraction of killed cancer cells . . . . .	83
---	----

# Nomenclature

$\Delta P$	pressure difference between two ends of a vessel
$\Delta t$	time interval between injections
$\delta t$	short time of injection in bolus
$\mu$	blood flow viscosity
$\Omega$	boundary between tumor tissue and surrounding normal tissue
$\phi$	fraction of tumor volume accessible by drugs
$\phi_L$	fluid sink originated from lymphatic system
$\phi_R$	amount of drug consumed by reacting with interstitium
$\phi_S$	source term for drug molecules extravasating from the vessel walls
$\phi_V$	fluid source originated from vasculature
$\pi_i$	interstitial fluid osmotic pressure
$\pi_V$	plasma osmotic pressure
$\tau$	blood half-life of drug molecules
$\xi$	rate of drug injection
$C$	interstitial concentration of drug
$C_b$	concentration of bound drugs to cancer cell receptors
$C_e$	concentration of cancer cell receptors

$C_f$	concentration of free drugs in tumor tissue
$C_{int}$	concentration of internalized drugs within cancer cells
$C_n$	concentration of liposome nanoparticles
$C_{p0}$	drug's initial concentration in plasma
$C_p$	plasma concentration of drug
$D$	diffusion coefficient of drug in interstitium
$D_f$	diffusion coefficient of free drugs within tumor tissue
$D_n$	diffusion coefficient of liposome nanoparticles
$K$	hydraulic conductivity of tumor
$K_{int}$	rate of drug internalization within cancer cells
$K_{off}$	unbinding rate of drugs from cancer cell receptors
$K_{on}$	binding rate of drugs to cancer cell receptors
$K_{rel}$	release rate of encapsulated drugs within liposome nanoparticles
$L_P$	hydraulic conductivity of vessels
$P$	vascular permeability
$P_i$	interstitial fluid pressure
$P_V$	blood pressure in vasculature
$Pe$	Peclet number across vessel wall
$Q$	volume flow rate of blood in vascular network
$r$	radius of blood vessel
$S/V$	surface area of the vessels per unit volume within the tumor
$S_F$	fraction of surviving cells
$T$	total period of treatment

$u_{accum}^{max}$  maximum allowable the accumulation of drug within tumor and normal tissue

$u_i$  interstitial fluid velocity

$u_{max}$  maximum allowable drug dosages to be injected

# Chapter 1

## Introduction

Cancer is the one of the foremost cause of death. Although many anticancer drugs have been developed, they are often ineffective. The ineffectiveness of cancer drugs is related to complex solid tumors' microenvironments, properties of the drugs, and the amount of their use in chemotherapy regimens. Therefore, better understanding of the complex microenvironment and mechanisms of drug delivery to solid tumors is crucial in designing an effective treatment strategy. Another problem in chemotherapy is that although solid tumors' properties vary extensively from one case to another, treatment protocols are not highly flexible; the ideal strategy would be to design specific treatment protocols for specific patients. Since many factors are involved in the delivery of drug molecules, it is almost impossible to experimentally and economically investigate all factors thorough clinical and preclinical studies. In contrast, mathematical modeling can play a very effective role. Thus using mathematical modeling, the aim of this work is to comprehensively investigate variables that affect chemotherapy, and then to propose a strategy that can determine optimal treatment conditions, personalized to a specific patient.

First, in [Ch. 2](#), a physically relevant tumor microenvironment, surrounded by a vascular network is modeled. Then, to model fluid flow within both tumor and normal tissue, the continuity equation and Darcy's law with appropriate boundary conditions are applied. Starling's equation is applied to model the fluid extravasating from vessel walls into the tumor interstitium. To solve these equations accurately in this complex environment, we have employed the finite element method with an adaptive mesh generation that combines high accuracy with a high calculation speed. Furthermore, by using advection-diffusion equation in normal and tumor tissue, the spatio-temporal concentration of drug molecules in the complex microenvironment of a tumor is calculated. Finally, we analyze how different

properties of tumors, their vasculature, drug molecules affect drug movements within tumor microenvironments.

Various solid tumors show a variety of tumor shapes and sizes with different vascular structures. A novel approach is developed in [Ch. 3](#) to address this diversity in tumor microenvironments and extend the basics introduced in [Ch. 2](#) to a personalized approach that can be applied to a specific tumor image, and thus to a specific patient. In these chapters, the computational framework developed in [Ch. 2](#) to model fluid flow and drug transport within tumor and normal tissue are applied to an idealized tumor image model, where tumor and vasculature are completely detectable. This image presents a typical tumor model with a general vascular structure, which can come from a high-resolution image taken from a patient under treatment. Furthermore, several tumor models are created to investigate the effect of microvascular density (MVD), tumor size, and the vessel locations on fluid flow and drug transport within tumor microenvironments. Some parts of this chapter is already published in the *Journal of Microvascular Research* [[67](#)].

Choosing the right dosages and right times of injection are important factors that determine the efficacy of chemotherapy. In [Ch. 4](#), an algorithm is developed to address how to determine optimal drug dosages to be injected in specific times. This optimization approach is built upon the computational frameworks presented in [Ch. 3](#). The goal of this optimization approach is to find a series of drug dosages which satisfies two constraints related to the toxicity and maximize the fraction of killed cancer cells at the end of treatment. This approach is applied to bolus injection and continuous infusion strategies for two cases of conventional therapeutic and liposome drugs. Finally, we have investigated the effect of different tumor microenvironment and drug properties on the optimal regimen and the treatment outcome.

The objectives of this work are:

- To calculate the distribution of drug macromolecules in a tumor microenvironment with a heterogeneous vascular network and investigate the effect of tumor and vasculature physiological properties on drug delivery.
- To develop an algorithm that is able to calculate spatio-temporal distribution of drug macromolecules in a generic tumor model, which can come from a high resolution tumor image with specified tumor boundary and vasculature.
- To analyze the effect of crucial features of tumor microenvironment such as microvascular density and vessel locations on the distribution of drugs.

- To develop an algorithm for finding the optimal chemotherapy dosages that can be applied to a specific patient. This algorithm takes into account the drug and tumor properties as well as drug toxicity.

# Chapter 2

## Mathematical Modeling of Tumor Microenvironment and Transport of Drug particles

### 2.1 Introduction

The most important limitation of therapeutic drugs is their inability to reach most of the cancer cells because of the physiological barriers such as elevated Interstitial Fluid Pressure (IFP) in tumors, clearance by blood flow, and compact media of solid tumors. In addition to this difficulty, most of the anticancer drugs have toxicity effects on normal cells and even they cannot prevent regrowth of tumors if they reach cancer cells [56].

Tissue space consists of three parts, which have important roles in drug delivery: the vascular network, the interstitium and cellular space. the vascular network comprises of blood vessels and capillaries. The interstitium is a gel-like space between vasculature and cells and includes collagen that gives structural stability to proteins located in interstitium [6, 7, 8]. To reach cancers cells, drug molecules should permeate from vasculature and pass through vessel wall to enter tumor interstitium. However, the elevated IFP blocks this transportation and results in a heterogeneous distribution of drug molecules in solid tumors.

High IFP in solid tumors is one of the main barriers to drug delivery [55, 5]. Lack of lymphatic drainage in solid tumors and leaky abnormal vasculature contribute to the elevated IFP [6]. For the first time, Boucher et al.[10] experimentally confirmed that for an

isolated tumor, IFP is very high and close to the microvascular pressure within the tumor, whereas it decreases suddenly at the tumor periphery. In contrast, in normal tissue, due to the existence of the lymphatic system, the IFP value is almost zero [55]. It is shown a dependency between the blood flow and IFP [70, 71], and IFP in the center of a tumor detached from the host tissue, follows the dynamic of blood pressure with a small delay in order of 10 seconds. Elevated IFP produces Interstitial Fluid Flow (IFF) outward from the tumor center and conveys tumor-produced macromolecules such as Vascular Endothelial Growth Factors (VEGFs) toward the normal tissue and also hinders drugs reaching most of the cancerous cells [54]. Studied by Jain et al. [55], IFP may cause metastasis and intensify tumor invasion by conducting cancerous cells toward the leaky vessels. Baxter and Jain [7] modeled IFP for a radially symmetric solid tumor with a homogeneously distributed vasculature. In their model, leaky vessels are distributed everywhere in the tumor and distributed uniformly, which are a source for fluid and macromolecules in the tumor interstitium. They mathematically confirmed that IFP plateaus in the tumor center at its maximum value, equal to the blood pressure, but decreases suddenly to zero at the tumor periphery, a finding in agreement with experimental data for an isolated tumor, a tumor detached from the normal tissue[10].

In contrast to the homogenous vascular model, real tumors show a complicated heterogeneous vascular structure: a high density of weak and leaky microvasculature at the tumor periphery owing to angiogenesis, creation of new vessels from the normal vessels surrounding tumor tissue [16, 17], and a lack of functional vasculature and the presence of a few dilated vessels inside the tumor [46, 47, 25, 24]. Due to the important role of vasculature in drug delivery, many researchers have developed different models for vascular network. Many of these researchers have modeled the formation of neo-vasculature in response to the molecular factors produced by tumor cells[18, 14]; however, these models capture only macroscopic features of tumor vasculature and are unable to consider microscopic phenomena such as branching and anastomosis. To consider microscopic features, Anderson and Chaplain[2] have modeled angiogenesis as a discrete lattice of endothelial cells. In this model, neo-vasculature growth from a parent vessel is shaped by certain probabilities. Tip cells in each lattice migrate to the adjacent tumor cells according to these probabilities, which are calculated as a function of different cellular phenomena such as branching rules, VEGF concentration, and endothelial cell density. Welter et al.[94, 96, 95] have proposed a more-realistic vascular remodeling that includes relevant physiological phenomena such as vessel co-option and regression. They use an arterio-venous vascular structure [39] as their pre-existing vasculature and as tumor grows, this structure is remodeled by the following phenomena: 1) based on the VEGF concentration, the tumor co-opts its vascular structure to form new vessels by the process of angiogenesis; 2) inside the tumor, high VEGF

concentration causes vessel dilation rather than angiogenesis; 3) the proliferation of cancer cells inside the tumor exerts mechanical forces on vessels inside the tumor. These vessels may collapse if the normal stress exerted by blood flow on their vessel walls cannot stand up to the normal stress applied by the tumor cells.

In addition to works on the modeling of IFP in a homogenous vasculature in solid tumors, which means vessels are located uniformly everywhere in the solid tumor [5, 6, 55], some recent studies have investigated the effect of physiological properties of tumor microenvironment surrounded by vascular network on IFP [101]. Wu et al. [99, 15] have calculated the IFP in a network of vasculature that grows toward the tumor from two parent vessels. Recently, Wu et al. [101] have calculated IFP in a continuous growth model of solid tumor with a dynamic formation of angiogenesis. Then, they studied the effect of IFP on oxygen extravasation from the vasculature and its consequent effects on tumor growth.

Although extensive studies have been done on tumor growth modeling, and recently, on dynamic vasculature modeling and calculation of IFP, just few studies have been conducted on the transport of drug molecules into solid tumors. The first formulation to calculate the concentration distribution in solid tumors is presented by Baxter et al. [5, 6, 7, 8]. They have studied the concentration distribution of two drugs, Fab and IgG, in an isolated circular tumor with uniform distribution of vasculature. In a very recent work, Welter et al. [97], for the first time, have studied the transportation of drug in a very sophisticated tumor microenvironment model that dynamically evolves. This complex microenvironment model includes the various parameters such as oxygen concentration distribution, VEGF and network of vasculature.

This study proposes a modeling framework to calculate the IFP, IFF, filtration rate of drug molecules from tumor vasculature and the blood flow vascular velocity within an environment of tumor tissue surrounded by normal tissue and located in a heterogeneous vascular network. In addition, the transport of drug molecules and drug concentration distribution has been simulated.

First, a physically relevant tumor microenvironment, surrounded by a vascular network is modeled. Then, the continuity equation, Darcy's law and Starling's equation with appropriate boundary conditions for normal and tumor tissues are developed to calculate the IFP and IFF. To solve these equations accurately in this complex environment, we have employed the finite element method with an adaptive mesh generation that combines high accuracy with a high calculation speed. Furthermore, by using advection-diffusion equation in normal and tumor tissue, dynamic concentration profile of drug molecules in the complex microenvironment of tumor is calculated. Finally, the effect of physiologi-

cal properties of tumor and vasculature and physical properties of drug molecules on the transportation of drug in tumor microenvironment are analyzed.

## 2.2 Vascular network modeling

Neovascularization of the tumor during angiogenesis is based on physiological conditions of tumor microenvironment, such as oxygen concentration and vascular endothelial growth factors (VEGFs). Proposed by Welter et al. [94, 95, 96, 50], the model involves a network of vasculature around and inside the tumor. To grow beyond  $1\text{mm}^3$ , a tumor releases some growth factors, mainly VEGFs, to provide more nutrients and oxygen [16, 33]. These VEGFs diffuse to the periphery of the tumor and stimulate the production of the neovascularization from the pre-existing vessels [46, 60]. Based on this model, at the center of a vascular network, the tumor is modeled as a circle whose radius increases linearly over time. This vascular network is modeled as a network of pipes with the laminar Poiseuille flow inside it [36]; therefore, the pressure difference between two ends of each vessel,  $\Delta P$  is calculated by

$$\Delta P = \frac{8\mu LQ}{\pi r^4} \quad (2.1)$$

where  $\mu$  is fluid viscosity,  $Q$  is volume flow rate of the fluid inside the vessel, and  $L, r$  are length and radius of the vessel, respectively. It has been assumed that the top-left corner of vascular network is connected to the artery at the pressure  $15\text{ mmHg}$  and the bottom-right corner is connected to the vein at the pressure  $0\text{ mmHg}$ , as shown in Fig. 2.1.

The algorithm for vascular network remodeling is composed of the following steps: Initial configuration of the model consists of blood vessels with the same size and radius arranged as a square lattice with a circular tumor at its center. Having set the initial configuration for the tumor and vasculature, the following steps remodel the vasculature in each time step:

1. By assuming sufficient oxygen in the tumor neighborhood, the tumor radius increases by one lattice site at each time step.
2. Due to the lack of oxygen inside the tumor, tumor cells start to produce VEGFs. The maximum concentration of the VEGFs is at the tumor center, and then they diffuse to the tumor periphery as a consequence of the concentration gradient. It is assumed that the distance of the diffusion region outside the tumor is  $\Delta_{\text{angio}}$ , which is equal to half of the initial tumor radius. Angiogenesis is modeled as an addition of

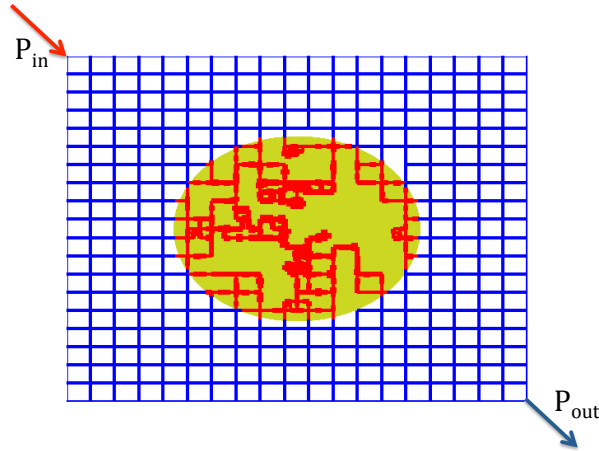


Figure 2.1: Blood fluid enters the network at the relative pressure  $P_{in} = 15 \text{ mmHg}$  and exits at the relative pressure  $P_{out} = 0 \text{ mmHg}$

“+” vessel to the pre-existing vasculature in the angiogenesis region by a pre-defined probability.

For the vessels inside the tumor, two scenarios are possible:

3. Instead of new blood vessel formation, VEGFs contribute to an increase of the vessel radius, dilation.
4. Vessels collapse if they cannot resist against the stress applied by the tumor cells

Criteria 3 and 4 depend on the amount of blood fluid flow rate through a vessel, which causes normal stress on the vessel wall. Less blood flow in the vessel causes less normal stress against normal stress exerted by tumor cells, and consequently, the more likelihood of vessel collapse [46, 3]; in contrast, more blood flow results in greater likelihood of vessel dilatation inside the tumor.

Fig. 2.2 shows the final vascular network after tumor growth, angiogenesis, vasculature collapse and dilation for a 30 by 30 square lattice. Vessels within the tumor are presented in red and vessels within normal tissue are blue. The white background represents both normal and tumor tissues. Irregularity of the vascular network inside the tumor and its periphery is shown in this figure; the highest density of vessels is in the tumor periphery, while most of the vessels close to the tumor center are collapsed because of the tumor cell

stress. This result also demonstrates that except a few thick vessels inside the tumor, the other functional vessels are collapsed due to the high stress from tumor cells. Moreover, the diffusion of VEGFs toward the tumor periphery initiates the formation of new blood vessels and causes high microvascular density at the tumor periphery. Unlike the regular network in normal tissue, regression, angiogenesis and dilation together create an irregular network of vessels at the periphery and within the tumor.

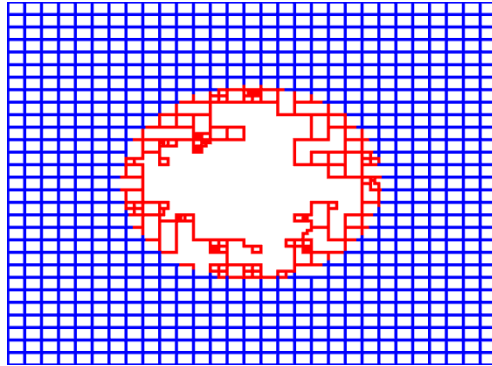


Figure 2.2: Vascular network with tumor and normal tissue for a lattice  $30 \times 30$ . Vessels inside the tumor are red, in normal tissue are blue, and white space is tissue, both normal and tumorous

## 2.3 Interstitial pressure calculation

### 2.3.1 Method

Like the real situation for tumors, the presented model consists of three parts each with different physiological properties: the vascular network, tumor tissue and normal tissue [60, 103]. The vascular network has a regular shape within the normal tissue but is irregular at the tumor periphery, where the high density of vasculature occurs, and there are a few functional vessels inside the tumor [32]. Considering these different regions, first developed by Baxter and Jain[5], we can calculate Interstitial Fluid Pressure (IFP) using transport phenomena equations. Since normal and tumor tissues are porous media, Darcy's law can explain fluid transport in this media:

$$u_i = -K \nabla P_i \tag{2.2}$$

where  $u_i$  [ $cm/sec$ ],  $K$  [ $cm^2/mmHg.sec$ ] and  $P_i$  [ $mmHg$ ] are Interstitial Fluid Velocity (IFV), hydraulic conductivity and IFP, respectively. Assuming a steady-state flow inside the media, we can utilize the continuity equation to calculate  $u_i$ :

$$\nabla \cdot u_i = \phi_V - \phi_L \quad (2.3)$$

where  $\phi_V$  [ $sec^{-1}$ ] is the tumor's fluid source originated from the vasculature and  $\phi_L$  [ $sec^{-1}$ ] is the fluid sink that arises because of the lymphatic system. Different values exist for  $\phi_V$  according to the different regions: vasculature region and interstitium. Since there is no accumulation of fluid in normal tissue, we can assume that in this region, considering its vasculature, the amount of fluid source and fluid sink are equal. Inside the tumor, each vessel acts as a source term for fluid and macromolecules; however, there is no sink inside the tumor due to the lack of a lymphatic drainage. Consequently, the modified continuity equation is

$$\nabla \cdot u_i = \begin{cases} \phi_V & \text{for vasculature} \\ 0 & \text{elsewhere} \end{cases} \quad (2.4)$$

where the source term,  $\phi_V$ , can be calculated using Starling's equation given by

$$\phi_V = \frac{L_p S}{V} (P_V - P_i - \sigma(\pi_V - \pi_i)) \quad (2.5)$$

where  $L_p$  [ $cm/mmHg.sec$ ] is hydraulic conductivity of the vessels inside the tumor;  $S/V$  [ $cm^{-1}$ ] is surface area of the vasculature per unit volume within the tumor;  $P_V$  [ $mmHg$ ] is blood pressure in vasculature;  $P_i$  [ $mmHg$ ] is IFP;  $\sigma$  is average osmotic reflection coefficient for plasma proteins;  $\pi_V$  [ $mmHg$ ] is plasma osmotic pressure; and  $\pi_i$  [ $mmHg$ ] is interstitial fluid osmotic pressure. Combining [Eq. 2.4](#) and [Eq. 2.2](#) gives us

$$-\nabla \cdot (K \nabla P_i) = \begin{cases} \phi_V & \text{for vasculature} \\ 0 & \text{elsewhere} \end{cases} \quad (2.6)$$

Assuming constant hydraulic conductivity for tumor tissue ( $K$ ), [Eq. 2.6](#) can be simplified to

$$\nabla^2 P_i = \begin{cases} -\phi_V/K & \text{for vasculature} \\ 0 & \text{elsewhere} \end{cases} \quad (2.7)$$

Substitution of  $\phi_V$  from Eq. 2.5 into Eq. 2.7 gives

$$\nabla^2 P_i = \begin{cases} -\frac{L_P S}{KV} (P_V - P_i - \sigma(\pi_V - \pi_i)) & \text{for vasculature} \\ 0 & \text{elsewhere} \end{cases} \quad (2.8)$$

Then the effective pressure,  $P_e$ , can be defined as a pressure at which fluid is extravasated from a vessel:

$$P_e = P_V - \sigma(\pi_V - \pi_i) \quad (2.9)$$

The dimensionless variables can be defined as  $x^* = x/L_{eq}$ ,  $y^* = y/L_{eq}$ , and  $P_i^* = P_i/P_e$  where  $L_{eq} = 5mm$ , the size of lattice edge, and  $x^*$ ,  $y^*$ ,  $P_i^*$  are dimensionless variables for axis  $x$ ,  $y$ , and  $P_i$ , respectively. Plugging these variables into Eq. 2.8 gives

$$\nabla^2 P_i^* = \begin{cases} \frac{L_P S}{KV} L_{eq}^2 (P_i^* - 1) & \text{for vasculature} \\ 0 & \text{elsewhere} \end{cases} \quad (2.10)$$

By defining  $\alpha = L_{eq} \sqrt{L_P S / KV}$ , this equation can be written as

$$\nabla^2 P_i^* = \begin{cases} \alpha^2 (P_i^* - 1) & \text{for vasculature} \\ 0 & \text{elsewhere} \end{cases} \quad (2.11)$$

To solve this equation for  $P_i^*$ , dimensionless IFP, the boundary conditions are necessary. The first such condition is the continuity of IFP and the interstitial fluid flux at the periphery of the tumor:

$$P_i^*|_{R^-} = P_i^*|_{R^+} \quad (2.12)$$

$$-(K \nabla P_i^*)|_{R^-} = -(K \nabla P_i^*)|_{R^+} \quad (2.13)$$

Second boundary condition is the IFP at the edges of the lattice, which is assumed to have a value equal to that in normal tissue:

$$P_i^*|_{x=0,L} = P_i^*|_{\text{normal tissue}} = 0 \quad (2.14)$$

$$P_i^*|_{y=0,L} = P_i^*|_{\text{normal tissue}} = 0 \quad (2.15)$$

To calculate  $P_i$ , based on Eq. 2.8, the only unknown variable is blood pressure inside the vascular network ( $P_V$ ), which changes throughout the network and should be calculated properly to reflect those changes. Having set these values at two corners, blood pressure

can be computed at the other nodes of the network using mass balance for each node:

$$\sum_{m=1}^k Q^{m,n} = 0 \quad 1 \leq k \leq 4 \quad (2.16)$$

where  $k$  is the number of connected vessels to node  $n$ , and  $Q^{m,n}$  is the net flow rate of the fluid from node  $m$  to node  $n$ . As shown in Fig. 2.3, for each vessel connected to node  $n$ , two flow rates exist: the vascular flow rate,  $Q_V^{m,n}$ , which comes from the adjacent node  $m$  and the transvascular flow rate,  $Q_t^{m,n}$ , which is due to the leaky permeable vessel and shows the flow rate of the fluid leakage from the vessel to the tumor interstitium. Therefore, the net fluid rate  $Q^{m,n}$  is given by

$$Q^{m,n} = Q_V^{m,n} - Q_t^{m,n} \quad (2.17)$$

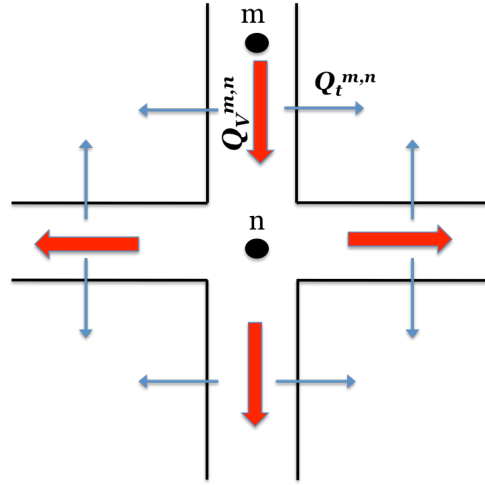


Figure 2.3: Vascular flow rate (red) and transvascular flow rate (blue) for each vessel

The vascular flow rate  $Q_V^{m,n}$  can be calculated by Poiseulles's law as follows:

$$Q_V^{m,n} = \frac{\pi r_{m,n}^4 (P_V^m - P_V^n)}{8\mu l_{m,n}} \quad (2.18)$$

where  $P_V^m$  is the vascular pressure at node  $m$ ;  $P_V^n$  is the vascular pressure at the node  $n$ ; and  $r_{m,n}$ ,  $l_{m,n}$  are the radius and the length of the vessel that connects node  $m$  to node

$n$ . In addition, the transvascular flow rate  $Q_t^{m,n}$  can be calculated by Starling's law:

$$Q_t^{m,n} = L_P(2\pi r_{m,n}L_{m,n})(\bar{P}_V^{m,n} - \bar{P}_i^{m,n}) \quad (2.19)$$

where  $\bar{P}_V^{m,n}$  and  $\bar{P}_i^{m,n}$  are the average values of the vascular pressure and the IFP between node  $m$  and node  $n$  respectively. Combining Eq. 2.16, Eq. 2.17, Eq. 2.18, and Eq. 2.19 results in

$$\sum_{m=1}^k \left( \frac{\pi r_{m,n}^4 (P_V^m - P_V^n)}{8\mu l_{m,n}} - L_P(2\pi r_{m,n}L_{m,n})(\bar{P}_V^{m,n} - \bar{P}_i^{m,n}) \right) = 0 \quad 1 \leq k \leq 4 \quad (2.20)$$

Eq. 2.8 and Eq. 2.20 are coupled and should be solved simultaneously. Using an iterative method, first an initial value for  $P_i$  in all nodes is guessed and then  $P_V$  for all nodes in the network is calculated using Eq. 2.20. Then, we update  $P_i$  by solving Eq. 2.8 until the convergence for both of  $P_i$  and  $P_V$  for all nodes in the network occurs. Finally, the vascular flow velocity,  $U_V^{m,n}$ , and transvascular velocity,  $U_t^{m,n}$ , as two important physiological factors, can be calculated by the following equations:

$$U_V^{m,n} = \frac{Q_V^{m,n}}{\pi r_{m,n}^2} \quad (2.21)$$

$$U_t^{m,n} = \frac{Q_t^{m,n}}{2\pi r_{m,n}l_{m,n}} \quad (2.22)$$

The parameters used in these equations has been measured experimentally by Baxter and Jain [5] and listed in Tab. 2.1.

### 2.3.2 Results and Discussion

Coupled equations for IFP have been solved numerically using the finite element method. Fig. 2.4 shows the mesh generated for this vascular structure where the mesh density is very high at the vessel locations inside the tumor because the IFP equation depends on the vascular structure located in the tumor region. Due to the complexity of tumor microenvironment, to solve coupled equations of IFP and the mass conversation in each node of the network, an adaptive mesh generation for numerical calculations has been used. Using uniform mesh to solve this PDE may result in different answers for different mesh sizes because the size of mesh affects the value of the source term, as in Eq. 2.8. Using adaptive mesh is essential, especially when vessels are sparse, which is the case inside the

Table 2.1: Physiological parameters used in the numerical simulation, as taken from [5]

Parameter	Tissue	Baseline value	Reference
$L_p [cm/mmHg.s]$	Normal	$0.36 \times 10^{-7}$	[76]
	Tumor	$2.8 \times 10^{-7}$	[5]
$K [cm^2/mmHg.s]$	Normal	$8.53 \times 10^{-9}$	[84]
	Tumor	$4.13 \times 10^{-8}$	[5]
$S/V [cm^{-1}]$	Normal	70	[74]
	Tumor	200	[45]
$\pi_B [mmHg]$	Normal	20	[11]
	Tumor	20	[11]
$\pi_i [mmHg]$	Normal	10	[98]
	Tumor	15	[5]
$\sigma$	Normal	0.91	[4]
	Tumor	0.82	[23]

tumor and close to its center. Using an iterative method allows blood pressure and IFP

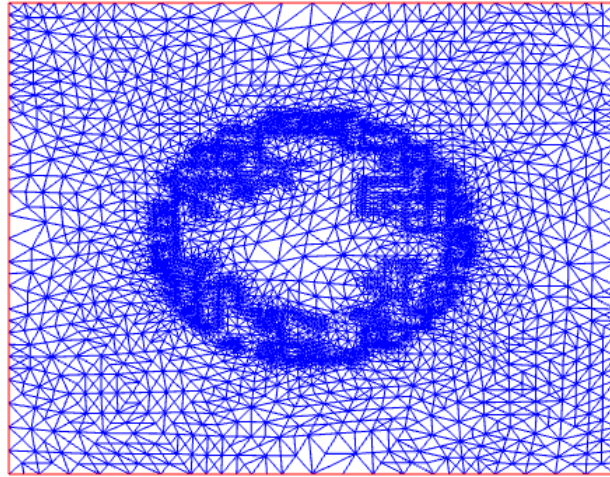


Figure 2.4: Generated adaptive mesh to solve IFP equation coupled with blood flow equation

to be computed. Blood pressure distribution is shown in Fig. 2.5, in which the maximum pressure occurs at the artery source, the top-left corner, but it gradually decreases until drops to zero at the vein connection point, the right-bottom corner. Obviously, in the

tissue where there are no vessels, vascular pressure is zero. Vascular pressure, as shown in Fig. 2.5, changes very slowly at the tumor periphery, where angiogenesis happens. In this region, the value for vascular pressure is  $7.4 \pm 1.6$ , which is about 10% of all changes in network. At the angiogenesis region, the high number of vessels causes the blood flow rate to be divided to the many branches; thus, the flow rate in each vessel decreases significantly, which results in considerable reduction in vascular pressure gradient.

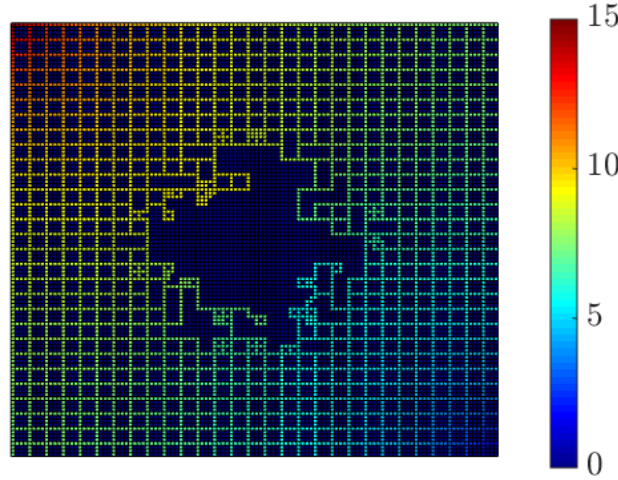


Figure 2.5: Blood pressure  $P_V(mmHg)$  distribution within the vascular network

IFP distribution, shown in Fig. 2.6, demonstrates that the dimensionless maximum IFP with value 0.784 occurs inside the tumor where vasculature density is the highest. This figure also shows that IFP plateaus at the tumor tissue and decreases from the center toward the normal tissue. We found that vascular morphology affects IFP distribution, where a strong correlation exists between them, as shown in Fig. 2.6. Moreover, comparing IFP distribution in this figure with the homogenous case presented in the literature[5, 55] shows that the maximum dimensionless IFP in heterogeneous vasculature, 0.78, is less than that in homogenous case which is 1. In the homogenous vasculature, it has been assumed that vessels exist everywhere inside the tumor; however, in the heterogeneous one, just a few vessels are inside the tumor and most of them are collapsed due to the tumor cell stresses. Consequently, the less the vasculature, the less source is for extravasated fluid, and therefore, the less IFP in the tumor. After calculation of IFP, interstitial fluid velocity (IFV) can be obtained using Darcy's law (Eq. 2.2). As shown in Fig. 2.7, IFV is the highest at the tumor periphery,  $0.022 \mu m/sec$ , due to the high gradient of IFP at this region. In contrast, its value is almost zero inside the tumor. High IFV, shown in Fig. 2.7, at the tumor periphery causes most of drug molecules to accumulate at the periphery of the tumor

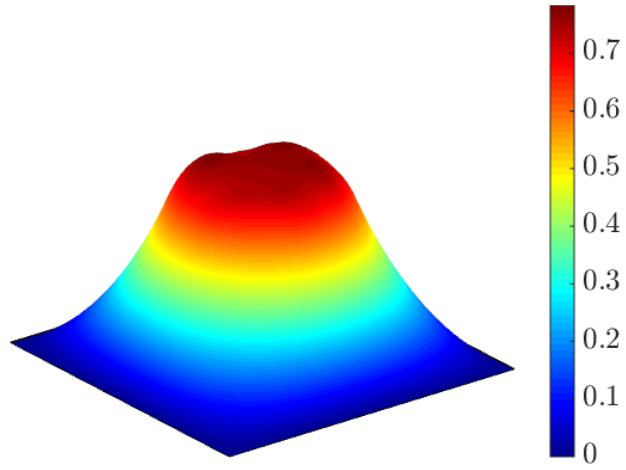


Figure 2.6: Dimensionless IFP ( $P_i^*$ ) distribution within tumor microenvironment

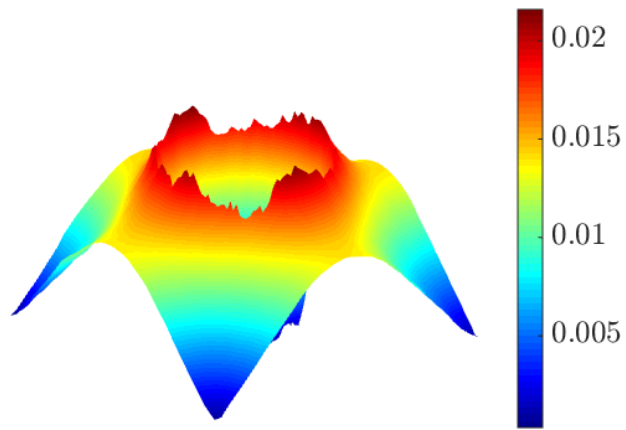


Figure 2.7: Interstitial fluid velocity ( $\mu m/s$ ) distribution in tumor and normal tissue

and so they cannot reach the tumor center. However, drug molecules can reach the tumor center and stay there if there is functional vasculature in it because the IFV is almost zero and there is no driving force to repel the drug molecules. Here, the maximum IFV is  $0.022 \mu\text{m}/\text{sec}$  compared with the homogenous vasculature inside the tumor, which is  $0.17 \mu\text{m}/\text{sec}$  [5, 55]. This difference in IFV is due to the less number of vessels in this case, which results in less gradient of pressure and consequently less IFV in tumor periphery.

Fig.2.8 presents transvascular velocity distribution, the velocity in which macromolecules can pass through vessel wall and perfuse to the interstitium. The maximum value for transvascular velocity is  $0.01 \mu\text{m}/\text{sec}$  and happens in the peripheral to the tumor where vessels are leaky and weak, IFP is relatively low, and pressure difference between vessel and interstitium as a driving force for transferring of materials from vessels is high. Furthermore, in normal tissue, for vessels close to the artery, transvascular velocity is higher than that of vessels in the vein's neighborhood. Differing from transvascular velocity intravas-

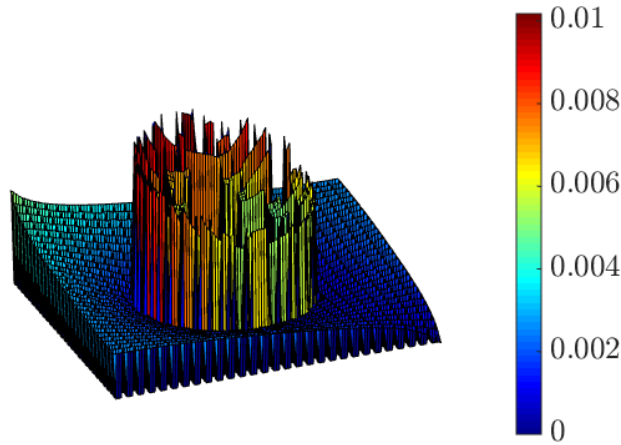


Figure 2.8: Transvascular velocity ( $\mu\text{m}/\text{s}$ ) distribution in the network

cular velocity, shown in Fig. 2.9, -the velocity of blood inside the vessels- is very high in the vessels in the vicinity of artery and vein connection points, whereas it decreases toward the tumor. The maximum intravascular velocity is  $6200 \mu\text{m}/\text{sec}$ , which is much higher than the maximum value for transvascular velocity,  $0.01 \mu\text{m}/\text{sec}$ . The effects of parameters used in this modeling on IFP are shown in Fig. 2.10. This figure demonstrates that IFP increases when the hydraulic conductivity of the tumor interstitium decreases. Hydraulic conductivity of a porous media represent the degree of compactness of that media. Denser media have lower hydraulic conductivity. When hydraulic conductivity a tumor is higher, interstitial fluid easier flows through the tumor, leading to lower IFP. In contrast, IFP increases with the increase of the hydraulic conductivity of microvascular walls. In higher

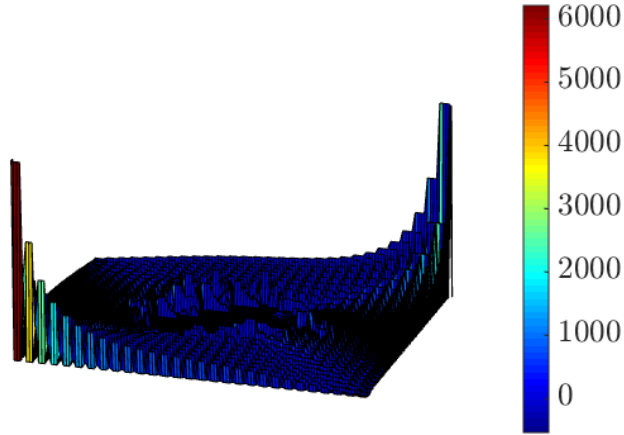


Figure 2.9: The intravascular velocity ( $\mu m/s$ ) distribution inside the network

hydraulic conductivity of a vessel, blood flow easier perfuse through the vessel wall to the tumor tissue resulting higher IFP in tumor. Finally, increasing the surface area of vessels per tumor volume conveys higher amount of blood fluid from vessel media to the tumor tissue contributing to elevation of IFP.

## 2.4 Transport of drug molecules to a solid tumor

### 2.4.1 Method

Drug molecules transport from microvasculature to tumor tissue with two mechanisms of diffusion and convection. In diffusion transportation mechanism, size and shape of drug are important factors. However, convection is affected by blood flow pressure, interstitial pressure, and interstitial fluid velocity. The transportation of drugs to the interstitial space of the tumor can be obtained using this advection-diffusion equation:

$$\frac{\partial C}{\partial t} + \nabla \cdot (u_i C) = \nabla \cdot (D \nabla C) + \phi_S - \phi_R \quad (2.23)$$

where  $C$  [ $g/ml$ ] is the interstitial concentration of drug;  $t$  [ $sec$ ] is time;  $D$  [ $cm^2/sec$ ] is the diffusion coefficient of drug in interstitium;  $u_i$  [ $cm/sec$ ] is the IFV, which can be calculated from the IFP value by utilizing Darcy's law;  $\phi_R$  [ $g/ml.sec$ ] is the amount of drug that is consumed by reacting with interstitium; and  $\phi_S$  [ $g/ml.sec$ ] is the source term for drug

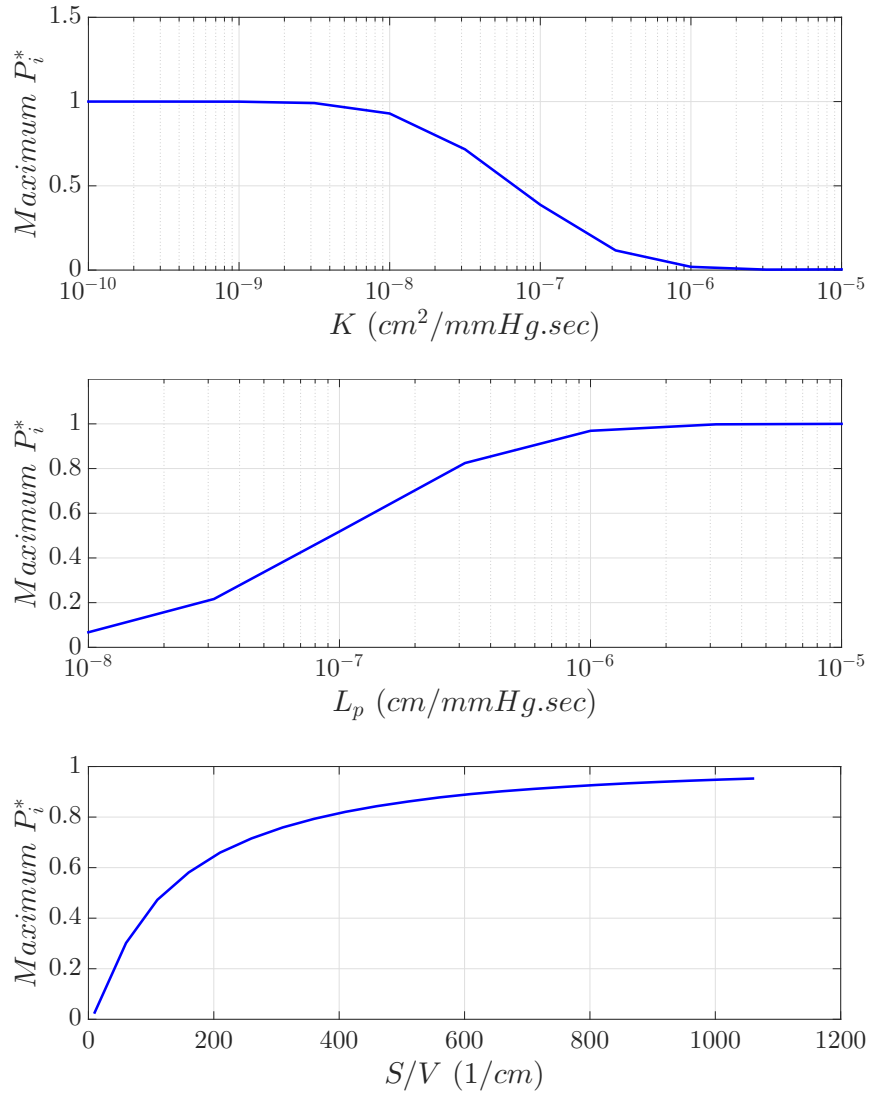


Figure 2.10: Dimensionless IFP  $P_i^*$  for different values of  $K$ ,  $L_p$ ,  $S/V$

molecules extravasating from the vasculature, which is given by the following equation:

$$\phi_S = L_P S(P_V - P_i)(1 - \sigma) \frac{C_p e^{Pe} - C}{e^{Pe} - 1} \quad (2.24)$$

where  $Pe = L_P(1 - \sigma) \frac{(P_V - P_i)}{P}$  is the Peclet number across the vessel wall;  $P$  is the vascular permeability ( $cm/sec$ ); and  $C_p$  is the plasma concentration of the drug macromolecules. This equation demonstrates that the amount of perfused drug molecules to tumor tissue depends on the permeability of vessel wall and difference between concentration of plasma and drug concentration in tissue next to the vessel wall. By combining [Eq. 2.23](#) and [Eq. 2.24](#) and neglecting the reaction of drug macromolecules with the tumor interstitium result in:

$$\frac{\partial C}{\partial t} + \nabla \cdot (u_i C) = \begin{cases} D \nabla^2 C + L_P S(P_V - P_i)(1 - \sigma) \frac{C_p e^{Pe} - C}{e^{Pe} - 1} & \text{for vasculature} \\ D \nabla^2 C & \text{elsewhere} \end{cases} \quad (2.25)$$

Since the drug concentration in plasma decreases over time, it can be assumed that the reduction happens exponentially and depends on the residence time of a drug in vasculature ( $\tau$ ):

$$C_p / C_{p_0} = \exp(-t/\tau) \quad (2.26)$$

To solve this partial differential equations and obtain the concentration profile of macromolecules, it is necessary to set the initial condition and boundary conditions. For the initial condition, the concentration at the time of drug injection is zero:

$$C|_{t=0} = 0 \quad (2.27)$$

Two types of boundary conditions exist for both. First, the drug concentration and its flux are continuous at the boundary ( $\Omega$ ) between tumor and normal tissue :

$$C|_{\Omega^-} = C|_{\Omega^+} \quad (2.28)$$

$$\{-D \nabla^2 C + \nabla \cdot (u_i C)\}|_{\Omega^-} = \{-D \nabla^2 C + \nabla \cdot (u_i C)\}|_{\Omega^+} \quad (2.29)$$

It can be assumed that at a sufficient distance from the tumor the concentration is zero:

$$C|_{x=0,L} = C|_{y=0,L} = 0 \quad (2.30)$$

As a case study, Fab (fragment-antigen binding) drug [\[5\]](#), which is widely used in monoclonal antibody therapy, is utilized for simulation and calculation of concentration distribution. The physical properties for Fab drug, listed in [Tab. 2.2](#).

Table 2.2: Physical properties used in simulation, as taken from [5]

Parameter	Tissue	Baseline value	Refrence
$D$ [ $cm^2/sec$ ]	Normal	$1.2 \times 10^{-8}$	[38]
	Tumor	$4.4 \times 10^{-8}$	[38]
$P$ [ $cm/sec$ ]	Normal	$19.1 \times 10^{-7}$	[38]
	Tumor	$149 \times 10^{-7}$	[38]
$\tau$ [ $hr$ ]	Plasma	3	[21]

## 2.4.2 Results and Discussion

Two case studies for calculation of drug concentration distribution have been considered: 1) constant drug concentration within plasma (in case of continuous injection) 2) drug concentration in plasma decays exponentially over time (bolus injection). To calculate the concentration profile in solid tumor surrounded by a normal tissue with vasculature (Fig. 2.2), Eq. 2.25 should be solved with the boundary conditions introduced in Eq. 2.28, and Eq. 2.29, Eq. 2.30.

Fig. 2.11 shows the concentration profile inside the solid tumor for different times when the injection is continuous, first case study. This figure reveals a strong correlation between vascular morphology and concentration distribution of the drug molecules shortly after injection.

At the early times of injection the maximum concentration of drug molecules occurs at the place of maximum density of vessels. The profile shows for the continuous injection of drug the ratio of maximum concentration to the plasma concentration is 0.9 that happens in a region close to maximum vascular density. However, the parameter analysis, as shown in Fig. 2.19, Fig. 2.20, Fig. 2.21, and Fig. 2.22 proves that this value depends on the physiological properties of tumor tissue and drug.

Fig. 2.11 also shows that the concentration profile of the drug does not change after 20 hours, which means, at this time, the amount of penetrated drug from vasculature to the tumor is equal to the amount of drug molecules washed away by interstitial fluid flow in normal tissue. To compare the change of concentration profiles over time, the maximum value of normalized concentration is shown in Fig. 2.12. This figure shows maximum dimensionless concentration ( $C^*$ ) of drug in the solid tumor increase over time and plateaus at time 20 and at the value 0.93.

Fig. 2.13 shows the concentration gradient of drug over time, which illustrates the share of diffusion in drug distribution. Shortly after injection, there is a high drug concentration

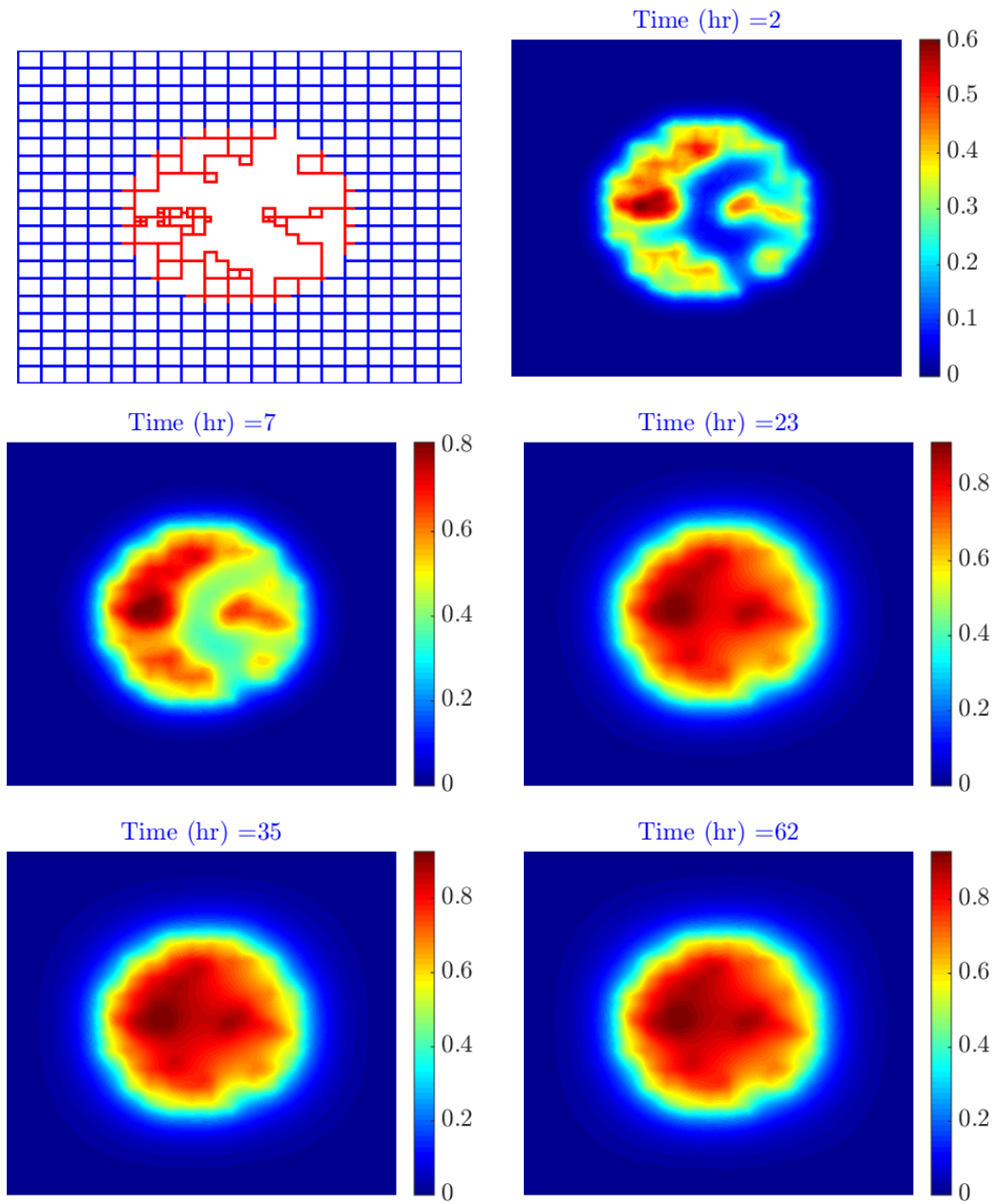


Figure 2.11: Dimensionless concentration profile within the vascular network for continuous injection

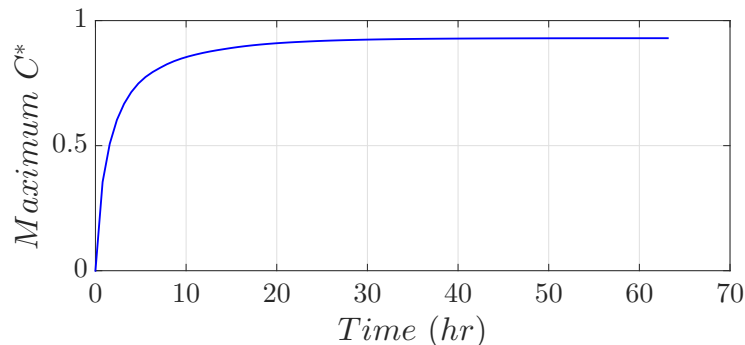


Figure 2.12: The distribution of maximum normalized concentration within the vascular network for continuous injection during 64 hours

gradient between vasculature and tumor tissue. However, after about 20 hrs, the concentration of drug in the tumor is constant and consequently the concentration gradient is close to zero. In contrast, at the tumor boundary, drug molecule permeated from vasculature wash away towards normal tissue by interstitial fluid flow. Consequently, high concentration gradient remains around at the tumor's boundary. Fig. 2.14 shows the maximum concentration of drug over time. Based on this figure, after the time 20 hrs the maximum of drug concentration gradient in tumor which implicates no change in diffusion rate after this time and steady-state of drug concentration profile.

For the second case study, exponential decay in drug molecules concentration in plasma, simulation is implemented for Fab drug. The data for Fab drug, obtained experimentally by Baxter et al. [6], shows the residence time ( $\tau$ ) of 3 hours, which means after 3 hrs the concentration of drug in plasma decreases to 37% of its initial value. For Fab drug, solving Eq. 2.25 with  $\tau = 3$  results the drug concentration distribution in the tumor over time, which is shown in Fig. 2.15. As this figure shows, drug concentration in tumor tissue increases at first, but it decreases eventually when the concentration of drug decreases in plasma.

Fig. 2.15 shows the asymmetry profile of concentration in the early times because of the heterogeneity of vasculature, but concentration profile changes to a symmetry behaviour after 30 hours. The reason is that after 14 hours the amount of drug in plasma drops below 1% of its initial value; therefore, practically there is no source after this time. This reduction in drug concentration in plasma results in drug concentration reduction due to its penetration from tumor tissue towards the neighbouring normal tissue and to the center of tumor, leading to a symmetry concentration profile after 30 hours.

Fig. 2.16 presents the maximum concentration of drug molecules during 64 hours after

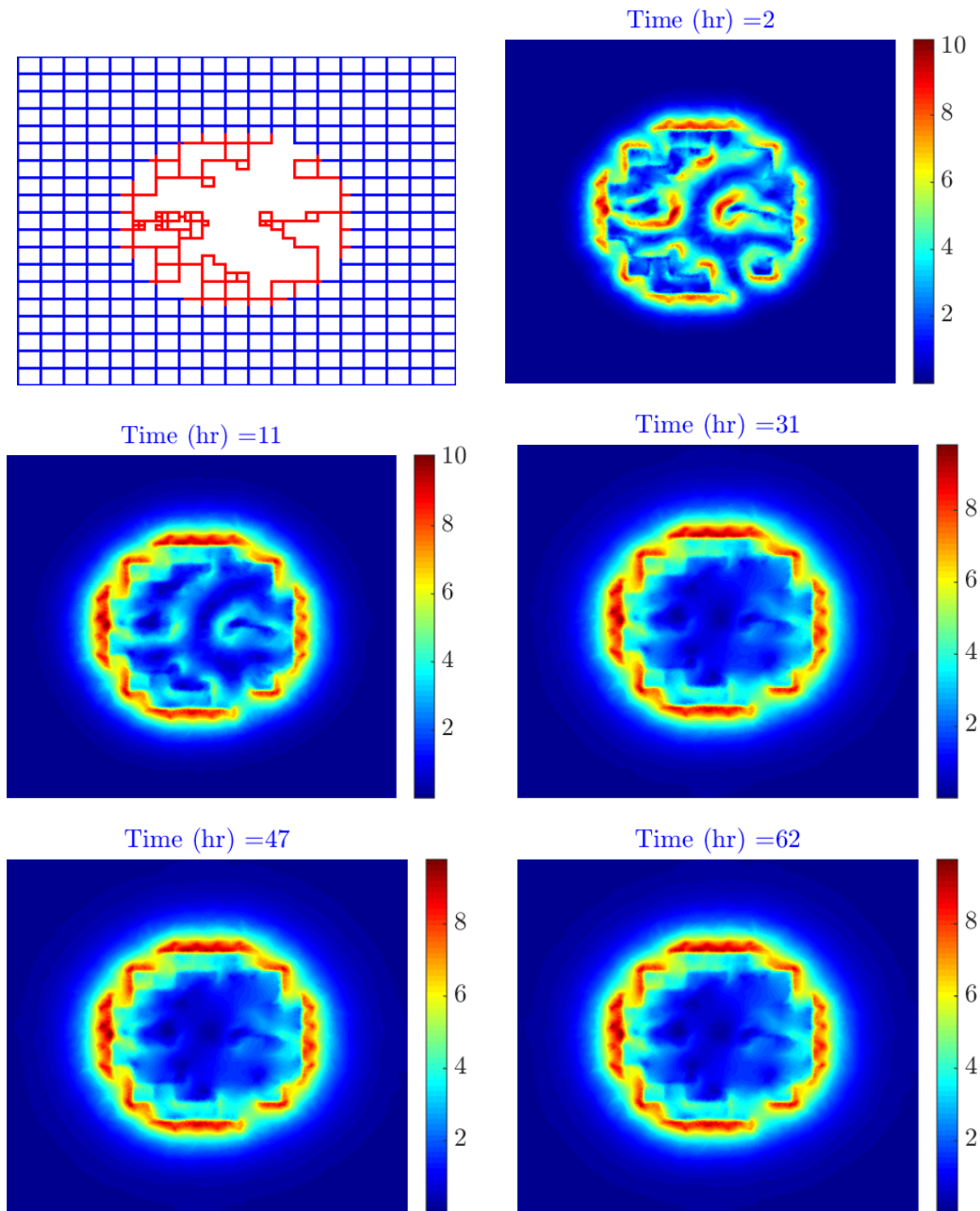


Figure 2.13: Dimensionless concentration gradient profile within the vascular network for continuous injection

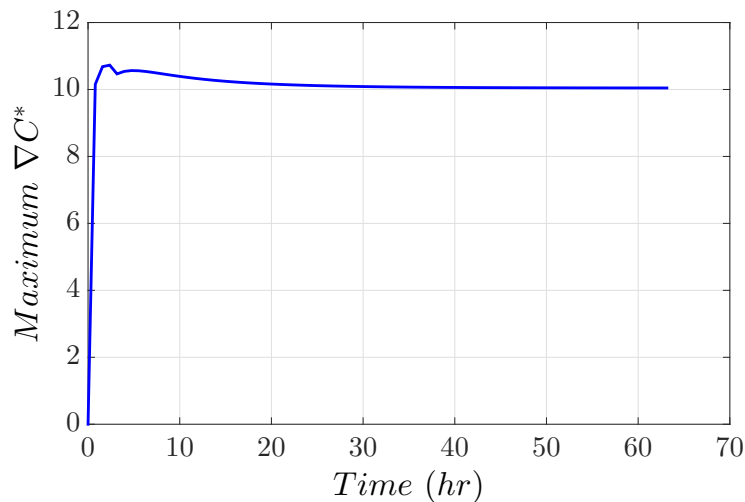


Figure 2.14: Dimensionless maximum concentration gradient profile within the vascular network for constant plasma concentration during 64 hours

injection. The drug concentration reaches its maximum value after 5 hours and then decays exponentially over time such that after 35 hours the maximum value is less than 10% of the its initial concentration in plasma.

It should be noted that the concentration profile changes for drugs with different value of  $\tau$ . Fig. 2.17 shows the effect of residence time of a drug on the maximum concentration distribution. Presented in this figure, drugs with residence time more than 20 hours reach the maximum concentration value after 15 hours. This figure also shows that the increase in drug residence time results in longer time in which drug has its maximum concentration. The drug's residence time in plasma( $\tau$ ) depends on the size and shape of drug. The smaller drugs have smaller clearance time by blood flow and consequently smaller value of  $\tau$ .

The maximum Concentration gradient of drug for different residence time is shown in Fig. 2.18. This figure illustrates that increase in residence time of drugs ( $\tau$ ) leads to being more effective for a longer time, that means drugs with bigger size (bigger  $\tau$ ) have longer effective time to kill cancerous cells.

The effect of different parameters on concentration distribution of drugs has been investigated. Fig. 2.19 shows the maximum normalized concentration of drug molecules for different values of drug diffusion coefficient. As shown in this figure, increase in diffusion coefficient causes drug molecules to diffuse easier to normal tissue and be washed away by interstitial fluid flow and results in lower concentration but more homogenous profile in the solid tumor. Thus, increase in diffusivity of drugs results in two opposite effects:

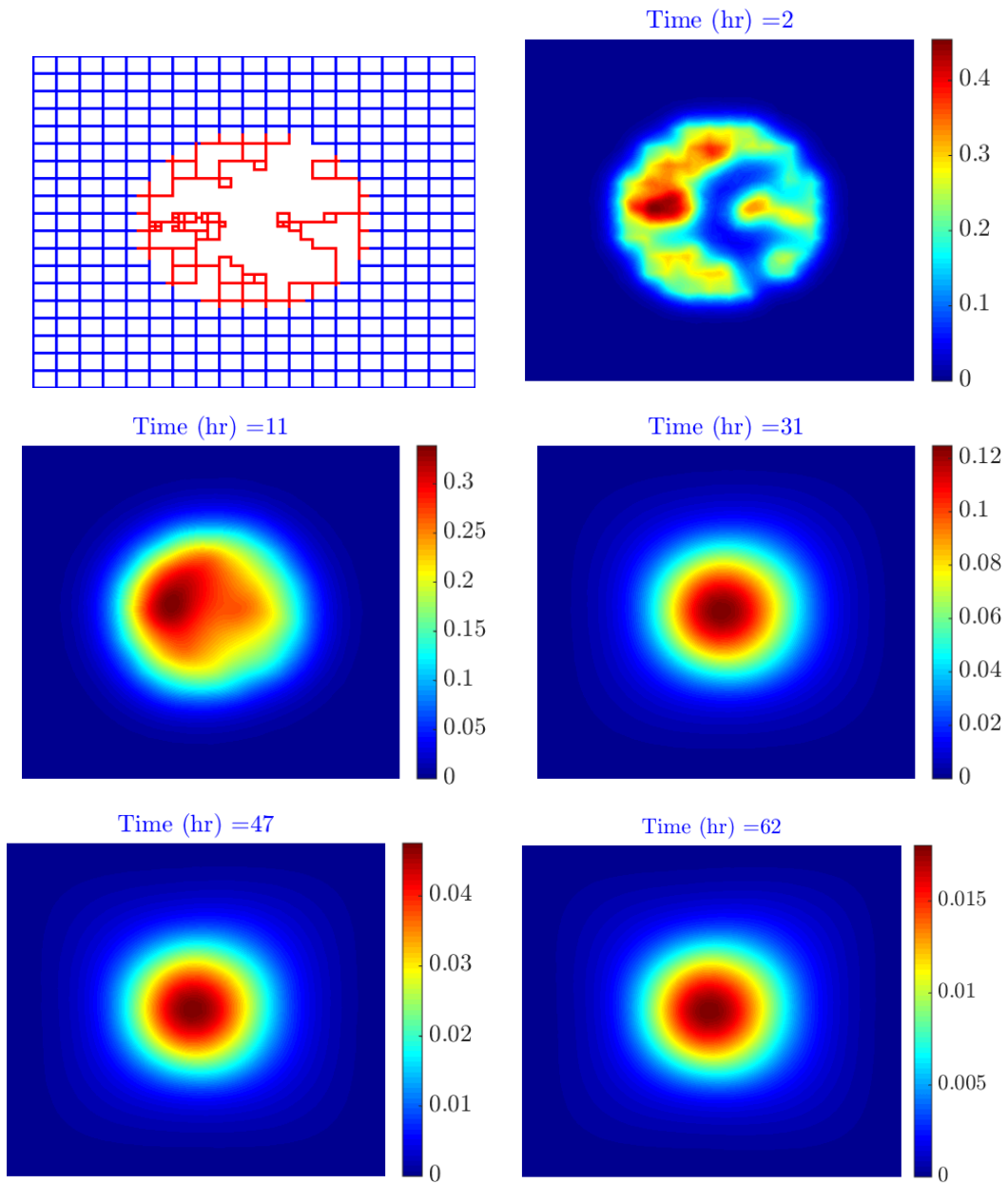


Figure 2.15: Dimensionless concentration profile within the vascular network for bolus injection of Fab drug

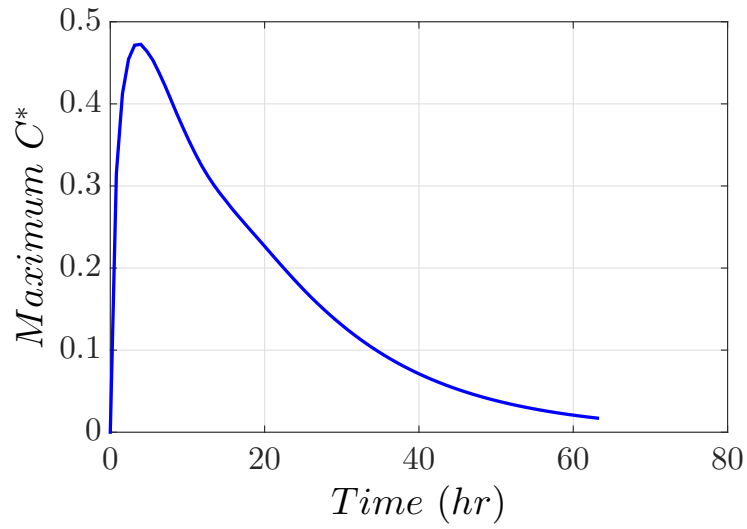


Figure 2.16: Dimensionless maximum concentration of drug molecules for bolus injection of Fab drug during 64 hours

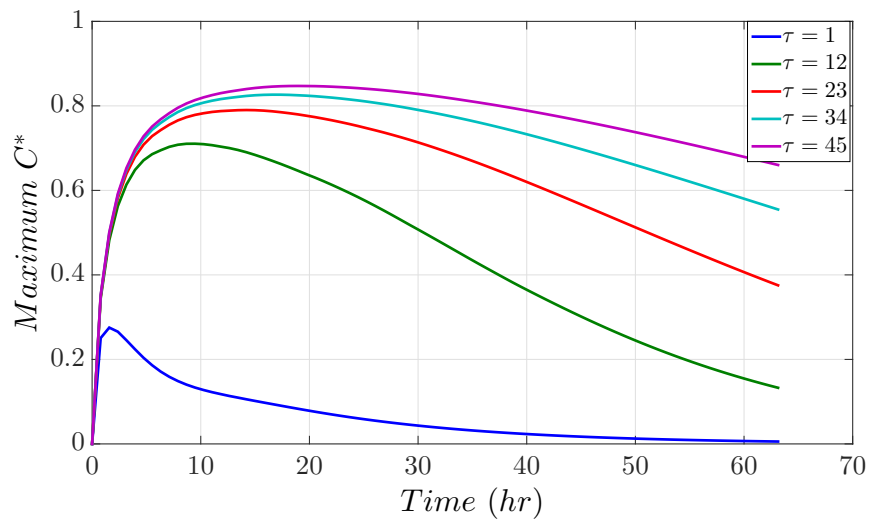


Figure 2.17: maximum dimensionless concentration of drug molecules for bolus injection and different residence times during 64 hours

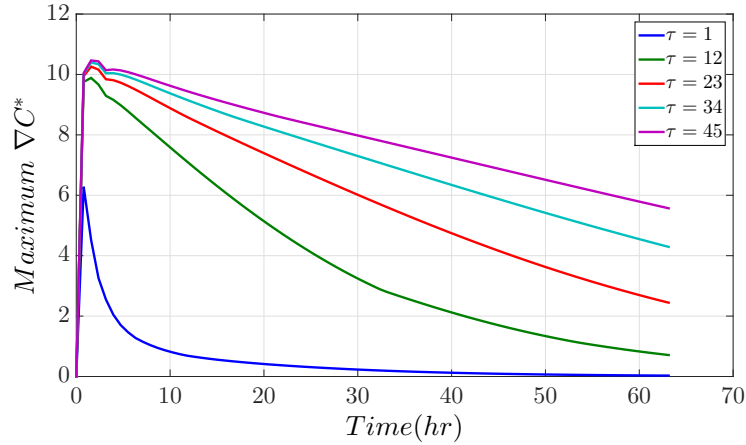


Figure 2.18: maximum dimensionless concentration gradient of drug molecules for bolus injection and different residence times during 64 hours

positive side that is homogenous distribution in solid tumors, which means drug molecules can reach most of the cancerous cells; and its negative side, which is its high clearance rate due to the faster diffusion towards normal tissue.

In addition to the drug properties, tumor microenvironment physical properties also have significant effects on drug concentration distribution. Fig. 2.20 shows the effect of tumor hydraulic conductivity on maximum drug concentration. Hydraulic conductivity illustrates the degree of easiness of fluid to move through a porous media, here solid tumor. If porous media is very compact flowing of fluid to pass through it is difficult, so hydraulic conductivity would be low. Drugs and other macromolecules can be transferred through the solid tumor easier, traveled by interstitial fluid flow, when hydraulic conductivity of tumor tissue is higher, resulting in lower concentration in solid tumor, as demonstrated in Fig. 2.20.

Physical properties of tumor vasculature also affect the drug distribution in solid tumors. Shown in Fig. 2.21, higher vascular hydraulic conductivity ( $L_p$ ) results in lower maximum concentration of drug molecules in the solid tumor. Higher  $L_p$ , as explained in Fig. 2.10, results in higher IFP, and consequently higher interstitial fluid flow repels drug toward the normal tissue.

Finally, the effect of vascular permeability is displayed in Fig. 2.22. As shown in this figure, increase in vascular permeability results in increase in drug concentration in the solid tumor. Higher permeability leads to higher penetration of drug from vessels to the tumor tissue and consequently higher drug concentration.

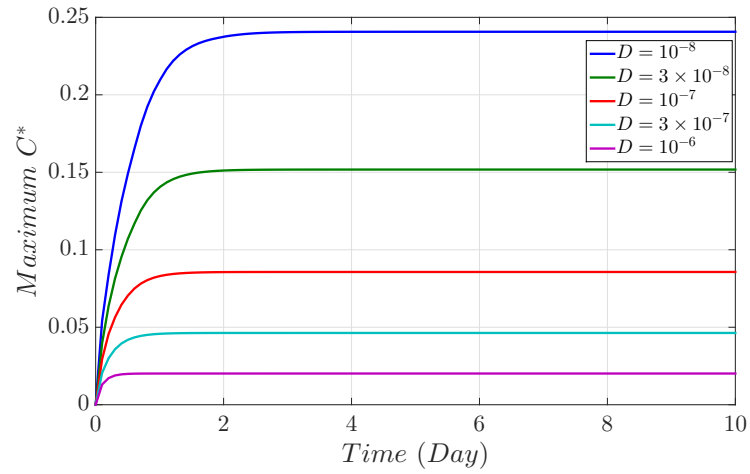


Figure 2.19: Maximum dimensionless concentration of drug molecules for continuous injection for different values of drug diffusion coefficient

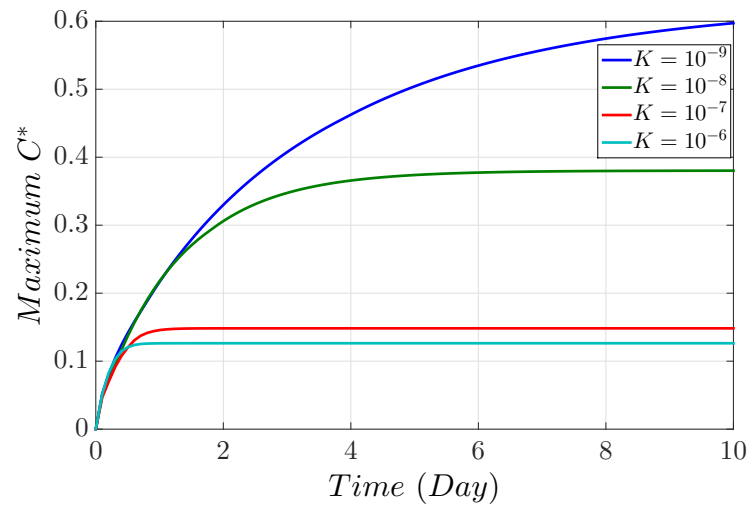


Figure 2.20: Maximum dimensionless concentration of drug molecules for continuous injection and for different values of tumor tissue hydraulic conductivity

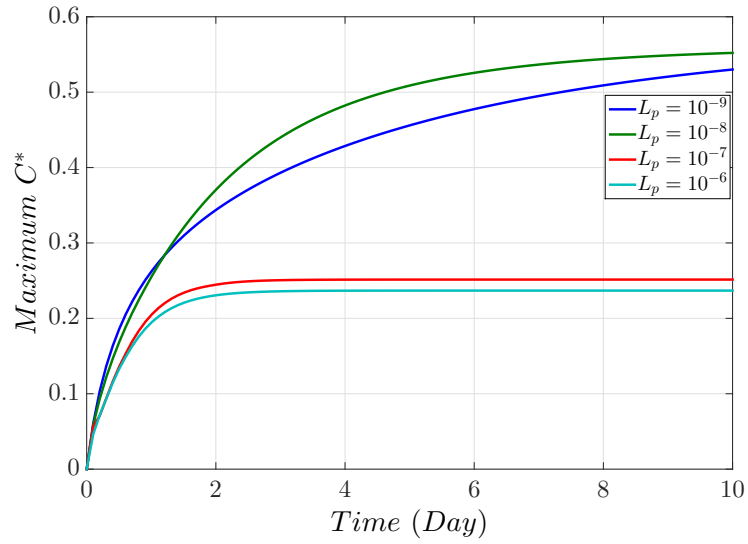


Figure 2.21: Maximum dimensionless concentration of drug molecules for continuous injection and for different values of vascular hydraulic conductivity

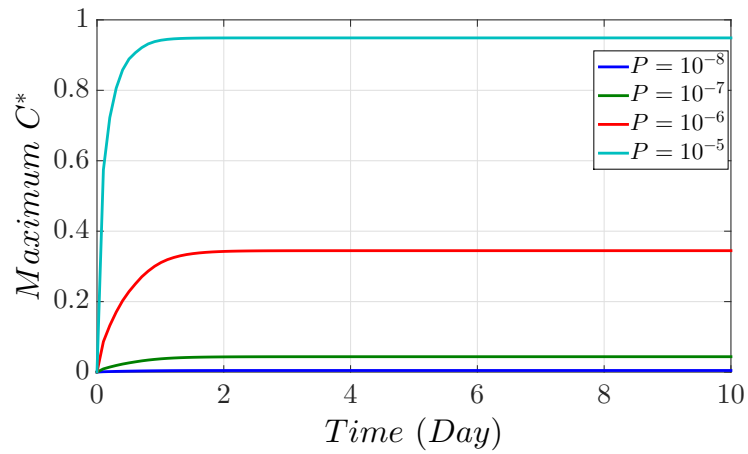


Figure 2.22: Maximum dimensionless concentration of drug molecules for continuous injection and for different values of vascular permeability

## Chapter 3

# Effect of Microvascular Distribution and its Density on Interstitial Fluid Pressure and drug distribution in Solid Tumors: A Computational Model

### 3.1 Introduction

Elevated interstitial fluid pressure (IFP) in solid tumors has been recognized as one of the main barriers to drug delivery [55, 5]. Angiogenesis, formation of neovasculature from pre-existing vessels, forms an abnormal and leaky vascular structure in solid tumors. This abnormal vascular accompanied by the lack of a lymphatic system leads to elevated IFP in solid tumors [5, 6, 87, 55]. Unlike in tumor tissue, in normal tissue, the lymphatic system acts as a sink for interstitial fluid, and the value of IFP is low, close to zero [54, 55]. Chemotherapy, uses toxic drug macromolecules to kill cancer cells or stop their proliferation. Drug macromolecules can be delivered to tumor sites using oral, intravenous-bolus, or isolated-infusion methods [66, 73]. Transport of these drug macromolecules to most cancerous cells is impeded due to the increased IFP. IFP elevation within the tumor induces interstitial fluid flow (IFF) from the tumor center toward the tumor edge and transports drug macromolecules and other particles produced by tumor cells toward the tumor periphery, where they accumulate and thus unable to function as desired[8, 97]. IFF

may promote metastasis by applying shear stress to cancerous cells and forcing them to move toward the lymphatic system adjacent to the solid tumor [55, 77].

IFP and transport of macromolecules for an isolated solid tumor was first modeled by Baxter and Jain [5, 6]. They assumed a spherical solid tumor with a homogenous vascular structure located throughout the tumor tissue. They showed that IFP is maximum at the tumor center and suddenly drops to zero at the tumor periphery, concurring with experimental data [9]. They also studied the transport of different drugs under two methods of delivery: continuous and bolus injection. They found that for continuous injection the drug concentration within the tumor increases over time; however, for bolus injection, first the interstitial concentration increases, and then decreases due to plasma clearance. Moreover, the concentration values depend on tumor physiological parameters and drug properties such as the molecular weight of drug macromolecules.

Unlike this model, real tumors show a heterogeneous vascular structure. This heterogeneity arises from angiogenesis at the tumor periphery and vessel collapse within the tumor tissue [52, 32, 10]. Angiogenesis leads to high microvascular density (MVD) at the tumor periphery [88, 32, 35]; whereas within the tumor, the solid stress exerted by cancer cells on vessel walls during tumor growth causes vessel collapse [83] and consequent reduction of MVD.

To consider the effect of angiogenesis and vessel collapse inside solid tumors during tumor growth, many models have been developed for vascular structure. Anderson and Chaplain [2] developed a model for angiogenesis, in which new vessels start to grow from a parent vessel in keeping with a certain probability calculated based on physiological conditions such as VEGF concentration and endothelial cell density. Welter et al. [94, 95, 96] developed remodeling of vascular structure based on phenomena such as co-option of neighboring vasculature to the tumor, tumor growth, and vessel collapse within the tumor.

In recent studies, the spatial and temporal distribution of drug macromolecules are calculated in the presence of heterogeneous vascular structure. Welter and Rieger [97] have studied IFP and drug delivery in a three dimensional arteriole-venous vascular network with simulated angiogenesis, vessel cooperation and regression phenomena [96]. They found that the interplay of diffusion and convection transport mechanisms in this heterogeneous vascular network results in heterogeneous drug distribution. Very recently, Wu et al. [100] utilized a two dimensional rectangular vascular network model, as a pre-existing vascular network, to investigate the transport of therapeutic agents. These vascular models are beneficial when investigating the interplay of different physiological phenomena within the tumor during drug transportation; however, they cannot be applied to a specific patient's tumor model, as tumor microenvironments change widely from one case to another.

Therefore, unlike these vascular models, in this study, we use an novel approach to calculate the spatiotemporal distribution of drug macromolecules within an arbitrary tumor microenvironment.

Association between MVD and many intra-tumor incidents during tumor growth has been revealed by many studies. Weidner [93] has found a strong correlation between MVD and patient survival rates in many types of cancer. Other clinical studies have compared patients with and without metastasis and found higher MVD in patients with this secondary condition [92, 51, 42, 37, 63].

This study explores how MVD, tumor size and the location of vessels affect IFP, IFF, and the distribution of drug macromolecules within tumor microenvironments. First, an drawing-based model of a solid tumor microenvironment is constructed. In this model, a solid tumor is surrounded by normal tissue, with both having a physiologically relevant vascular structure. Then, using Darcy’s law and Starling’s equation, IFP and IFV are calculated for different cases of tumor microenvironment. Finally, an advection-diffusion equation is utilized to calculate tempo-spatial distribution of drug macromolecules within different tumor models. This computational framework can be applied for a wide range of tumor images, in which the vasculature and tumor boundary are completely recognized.

## 3.2 Methods

Distribution of drug macromolecules inside solid tumors depends on the tumor microenvironment and distribution mechanisms. Therefore, a physiologically relevant tumor microenvironment model is necessary, and then using transport phenomena equations, the distribution of drug macromolecules over time can be calculated.

### 3.2.1 Vascular network modeling

When a tumor grows beyond  $1\text{ mm}^3$ , the lack of oxygen at the region far from the tumor periphery, causes the release of certain growth factors, mainly endothelial growth factors (VEGFs) [16, 33]. These growth factors diffuse to the tumor periphery, and by co-opting the vessels proximal to the tumor periphery, cause neovasculature to form [46, 60]. These formations lead to increased microvascular density (MVD) at the tumor periphery. Unlike the vessels at a tumor’s periphery, vessels within the tumor are affected by high density of cancer cells, which exert normal and shear stresses on the vessel walls, resulting in vessel collapse and consequent reduced MVD within the tumor [46, 3, 96, 83].

We have used a schematic tumor microenvironment, as shown in Fig. 3.1, to calculate the distribution drug macromolecules within this microenvironment. This figure depicts a typical shape for a solid tumor, surrounded by normal tissue and is assumed to be an ideal high-resolution image in which tumor boundary and vascular locations are perfectly detectable. Vessels within normal tissue (blue lines) have a regular structure compared to the vessels within the tumor (red lines), which have an abnormal structure. In addition, the heterogeneous distribution of tumor vasculature in Fig. 3.1, represents high MVD at the tumor periphery and low MVD in the area close to the tumor center.

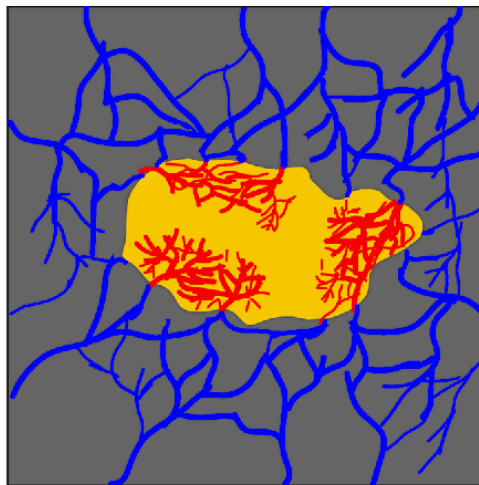


Figure 3.1: A typical solid tumor microenvironment surrounded by normal tissue and its vasculature. Blue lines are vessels in normal tissue and red lines are vessels within the tumor.

### 3.2.2 Transport of fluid and drug macromolecules

Drug macromolecules are distributed inside tissue thorough two different mechanisms: 1) Diffusion: drug macromolecules travel from a high concentration area to a low one. The diffusion flux can be calculated by Fick's law. 2) Convection: drug macromolecules travel with the bulk of fluid flowing within tissue. Since experimental data show fluid flow from the center of tumors outward [5, 6, 7], both diffusion and convection should be considered in macromolecule transport in solid tumors. To calculate the effect of convection on drug distribution, the fluid velocity inside the tumor interstitium should be computed first. Interstitial fluid velocity (IFV) can can be calculate using the Darcy's law, continuity

equation, and Starling’s law, as introduced in [Sec. 2.3.1](#). Then, the IFV values can be used in an advection-diffusion equation (as shown in [Sec. 2.4.1](#)) to calculate spatio-temporal distribution of drug macromolecules.

Two major differences exist between the tumor microenvironment model presented here and the one in [Ch. 2](#): 1) In [Ch. 2](#), we used a mathematical model to construct the tumor microenvironment, but the tumor model here can come from a reconstructed high resolution image, in which tumor and vasculature are well-defined. 2) Using a mathematical model imposes some limitations on the shape and the structure of tumor microenvironment, such as spherical tumor shape and square lattice vascular structure (as shown in [Fig. 2.2](#)), whereas, here, tumors can have any arbitrary shape and size and vascular structure are randomly distributed within tumor and surrounding normal tissue.

Here are the steps required to calculate IFP and concentration profile within an arbitrary tumor microenvironment:

1. Here we assume the tumor image is ideal, which means tumor boundary and vasculature within tumor and surrounding normal tissue are recognized and colored differently (as shown in [Fig. 3.1](#), tumor is yellow, normal tissue is grey, tumor vasculature is red, and normal vasculature is blue). If the tumor image has a low resolution, an extra image-processing step is required to recognize mentioned elements in it and label them with different color.
2. Finite element method (FEM) consisting of triangle elements (as shown in [Fig. 3.2](#)) can be applied to solve IFP and advection-diffusion equations. We use MATLAB PDE toolbox to generate an adaptive mesh where the maximum number of triangles is allowed to be  $10^4$ . The number of triangle elements and their size change during iterations of solving IFP and advection-diffusion equations.
3. Equivalent to image presented in [Fig. 3.1](#) is a 3-D numeric array ( $m \times n \times 3$ ) representing the RGB (Red, Green, Blue) value of each pixel of the image. To determine the parameter values in [Eq. 2.8](#) and [Eq. 2.25](#), we look at the center of triangle elements of generated mesh. If a triangle center is located on a pixel with color blue, red, yellow, or grey, therefore equation parameters of the vessels in normal tissue, vessels in tumor tissue, normal tissue, or tumor tissue will be applied, respectively.

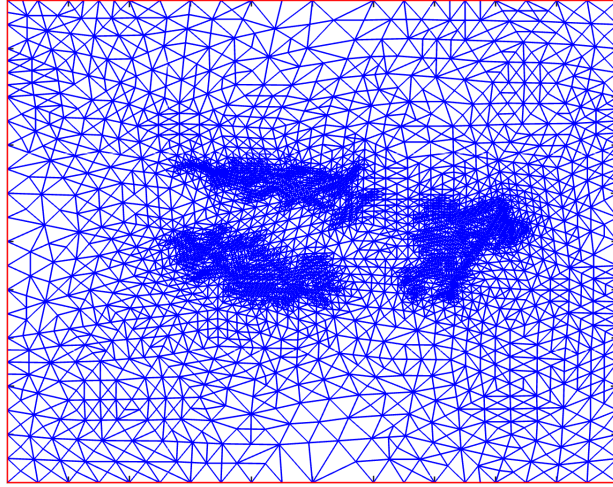


Figure 3.2: Adaptive mesh generated for the tumor model presented in Fig. 3.1.

### 3.3 Results

For the tumor microenvironment presented in Fig. 3.1, the interstitial fluid pressure (IFP), interstitial fluid velocity (IFV), and concentration profile for a specific drug (Fab) [5] are calculated, and then the effects of the microvascular density (MVD), tumor size and vascular location on IFP, IFV, and concentration profile of different tumors are investigated.

#### 3.3.1 Interstitial fluid pressure and macromolecule transport in a solid tumor

To calculate concentration distribution within the tumor, first, it is necessary to calculate the to take into account the convection mechanism of drug transport in the interstitium. The interstitial fluid pressure (IFP) and associated IFV can be calculated from Eq. 2.8 and Darcy's law (Eq. 2.2), respectively. Fig. 3.3 presents the distribution of both the IFP and IFV. This figure demonstrates that IFP is maximum at the region close to the tumor center and slowly reduces toward the tumor periphery, whereas maximum IFV occurs at the tumor periphery, and its value is almost zero at tumor center. Arrows in this figure present the magnitude and direction of interstitial fluid flow, indicating that the interstitial fluid flows from the tumor center toward the periphery.

Snapshots of concentration profile for the bolus injection of Fab drug over time are presented in Fig. 3.4 (see also Video A.1). The data for Fab drug, obtained experimentally

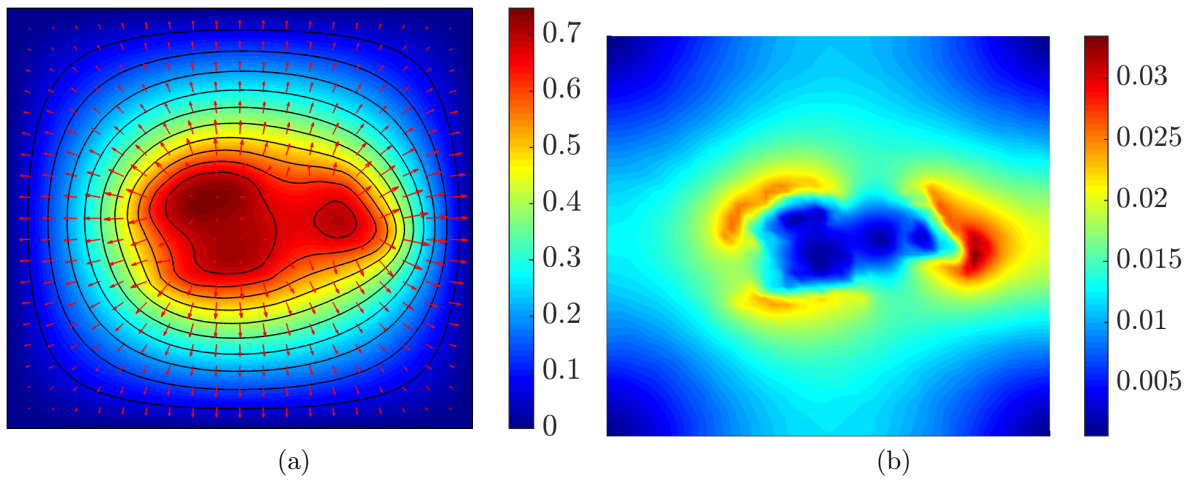


Figure 3.3: (a) IFP and (b) IFV distribution for the tumor in Fig. 3.1. Arrows in (a) show the direction and magnitude of interstitial fluid flow.

by Baxter et al. [6], shows the value  $\tau = 3 \text{ hr}$ , which means that after 3 hr post-injection the drug concentration in plasma decreases to 37% of its initial value. Fig. 3.4 reveals a strong correlation between vascular morphology and concentration distribution of the drug macromolecules early post-injection. The maximum concentration occurs where the maximum density of vessels exists, and the concentration profile correlates with the pattern of vasculature. As this figure shows, drug concentration in the tumor interstitium increases early post-injection but decreases thereafter when the drug concentration diminishes in the plasma.

Shown in Fig. 3.5, the drug concentration reaches its maximum value after 5 hours and then decays exponentially over time such that after 27 hours the maximum value of drug concentration is below 1% of its initial concentration in plasma.

### 3.3.2 Effect of microvascular density on interstitial fluid pressure

Six cases of tumor microenvironment (Fig. 3.6), which have the same tumor size and shape but different MVD inside and the same vascular structure in surrounding normal tissue, were constructed to investigate the effect of MVD on IFP, IFV, and drug macromolecule distribution.

Fig. 3.7 shows the maximum of IFP and the average of IFP for different cases of the tumor microenvironment presented in Fig. 3.6. Fig. 3.7 demonstrates that maximum values

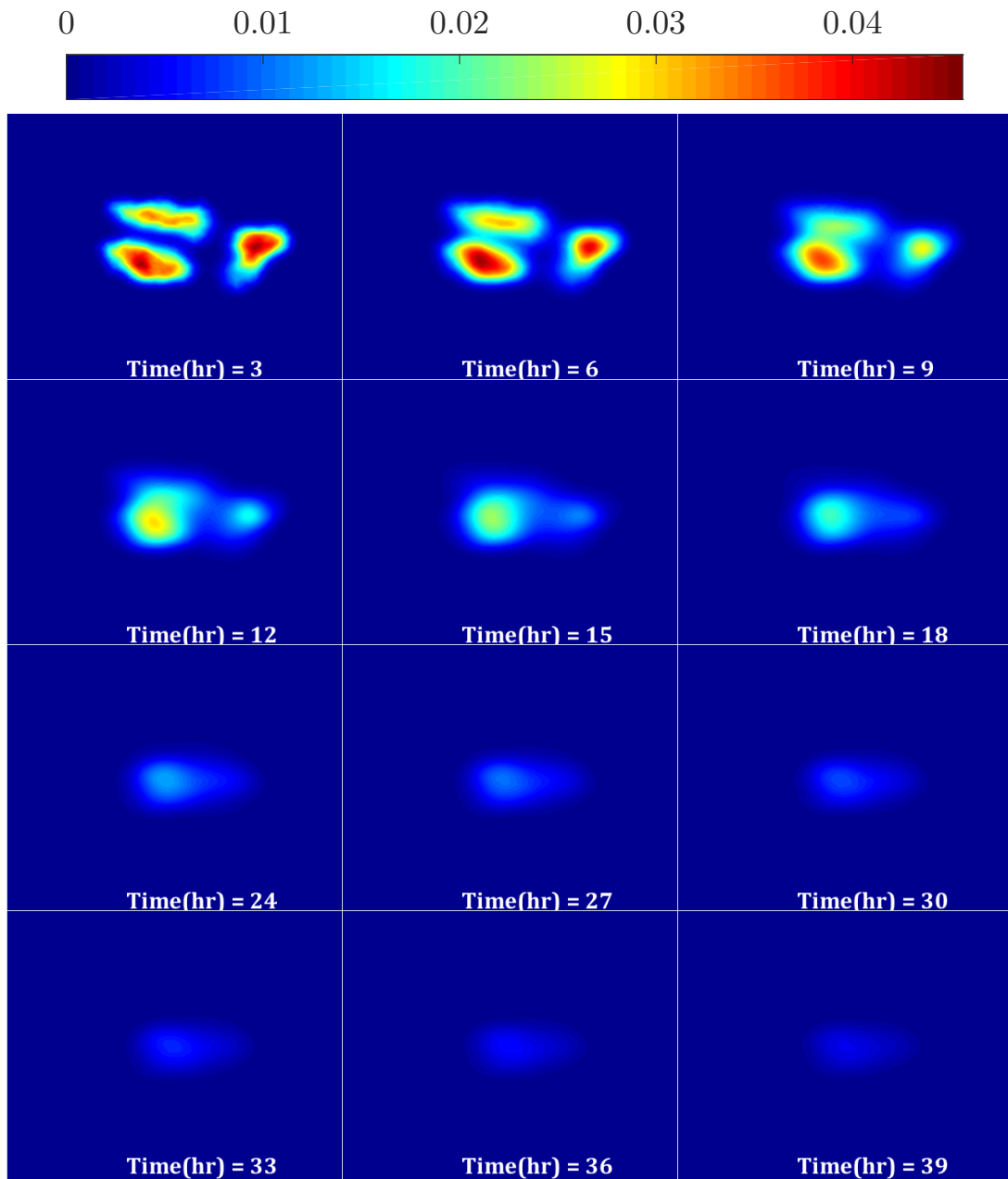


Figure 3.4: Concentration profile of Fab drug within tumor microenvironment presented in Fig. 3.1 at different times.

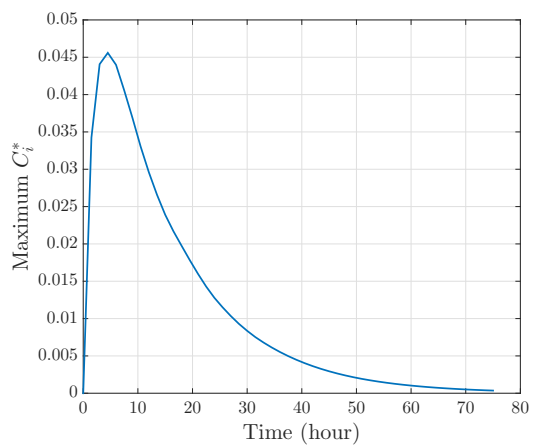


Figure 3.5: Dimensionless maximum concentration profile within the solid tumor over 75 hours.

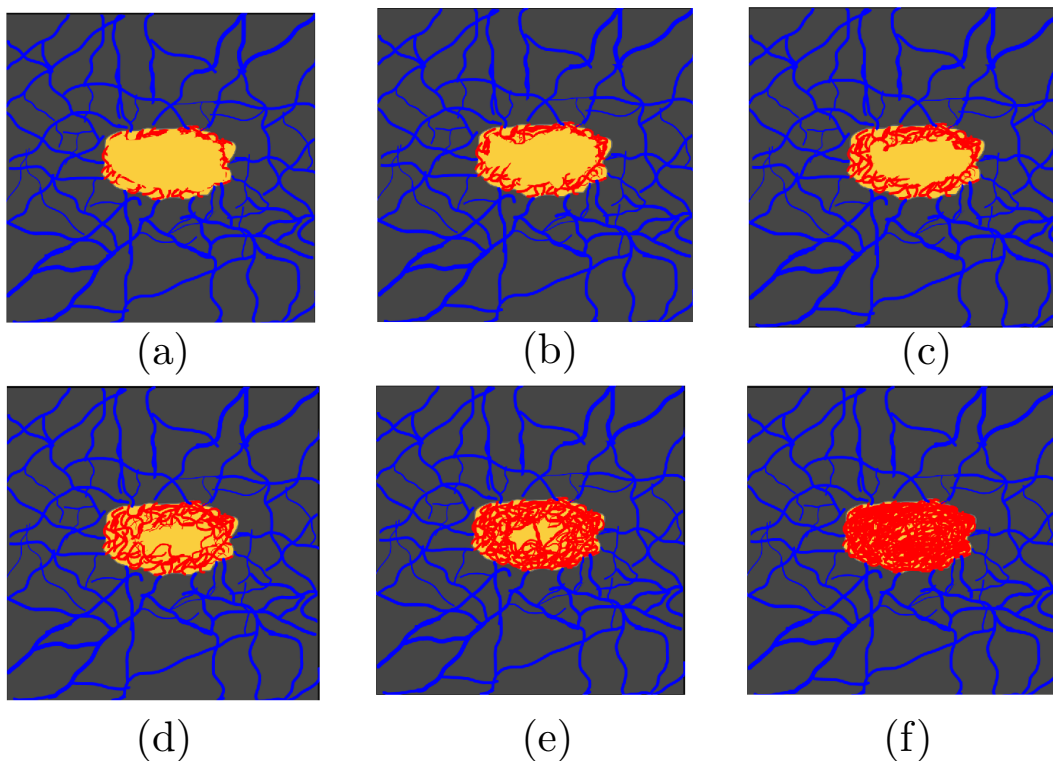


Figure 3.6: Tumors with different MVD values. The MVD values are: (a) 0.14, (b) 0.26, (c) 0.39, (d) 0.56, (e) 0.83, and (f) 0.99.

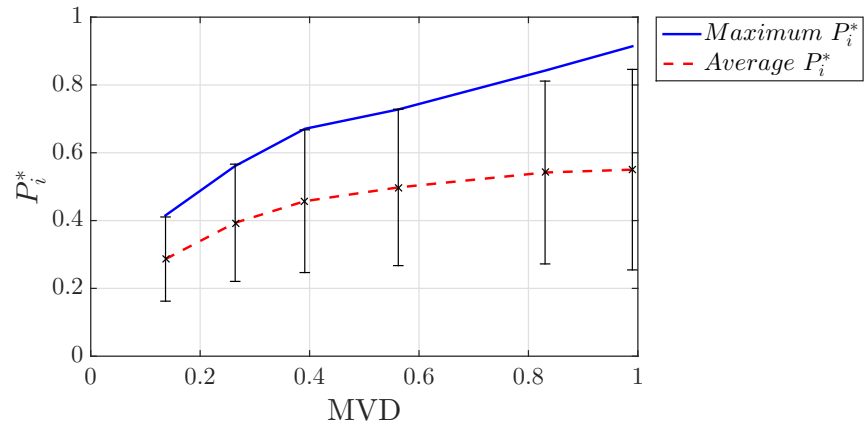


Figure 3.7: Maximum and average Dimensionless IFP for tumors with the same shape and size but different MVDs.

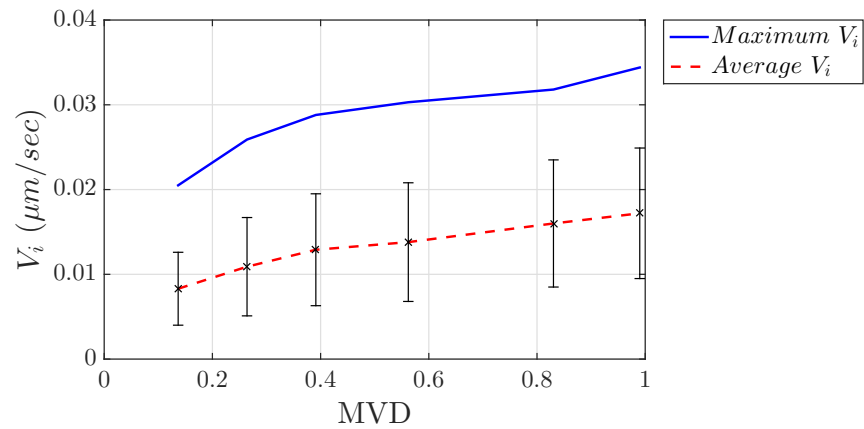


Figure 3.8: Maximum and average IFV ( $\mu\text{m}/\text{sec}$ ) for tumors with the same shape and size but different MVDs.

of IFP increase with increased MVD. For example, an increase in MVD from 0.2 to 0.5 enhances the maximum and average values of IFP by 50%. Similar to the IFP results, Fig. 3.8 demonstrates that IFV also increases with increased MVD, so that an increase in MVD from 0.2 to 0.5 leads to a 50% increase in IFV. Increased IFP and IFV associated with IFP enhances a barrier to the delivery of chemotherapeutic agents, preventing them from reaching most cancerous cells.

The averaged drug concentrations for different MVD values is shown in Fig. 3.9. This figure demonstrates that increased MVD results in an increased concentration of drug macromolecules in solid tumors. Moreover, for all cases, the concentration of macromolecules increases immediately post-injection, peaks after 5 hours, and then starts to decline, and drops to almost zero after 40 hours. The rate of drug concentration decline is not the same for all tumors, being faster in solid tumors with higher values of MVD, due to the higher IFV.

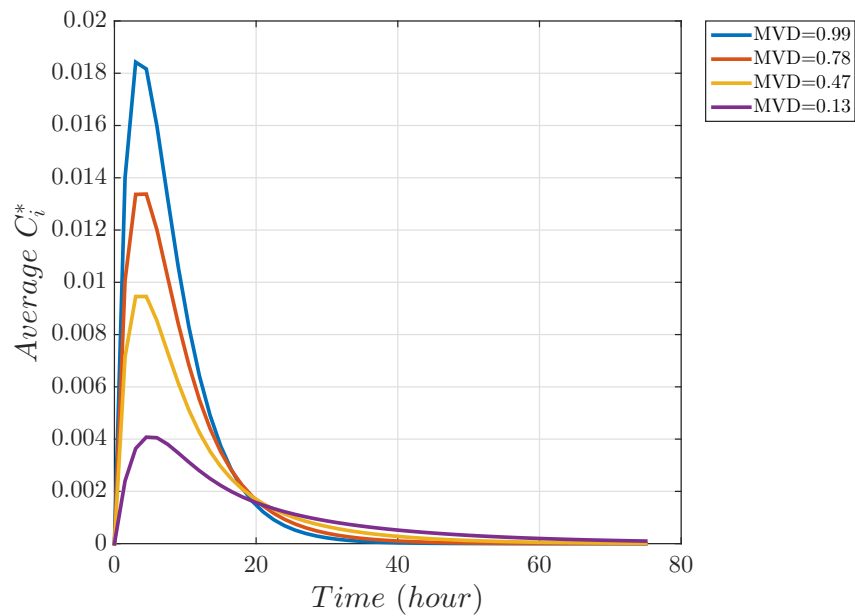


Figure 3.9: Average dimensionless concentration for tumors with different MVDs but the same shape and size.

### 3.3.3 Effect of tumor size with constant MVD on IFP, IFV, and drug concentration distribution

Tumor models (Fig. 3.10) of different sizes but the same shapes and the same vascular structures are constructed to investigate the effect of tumor size on the distribution of drug macromolecules.

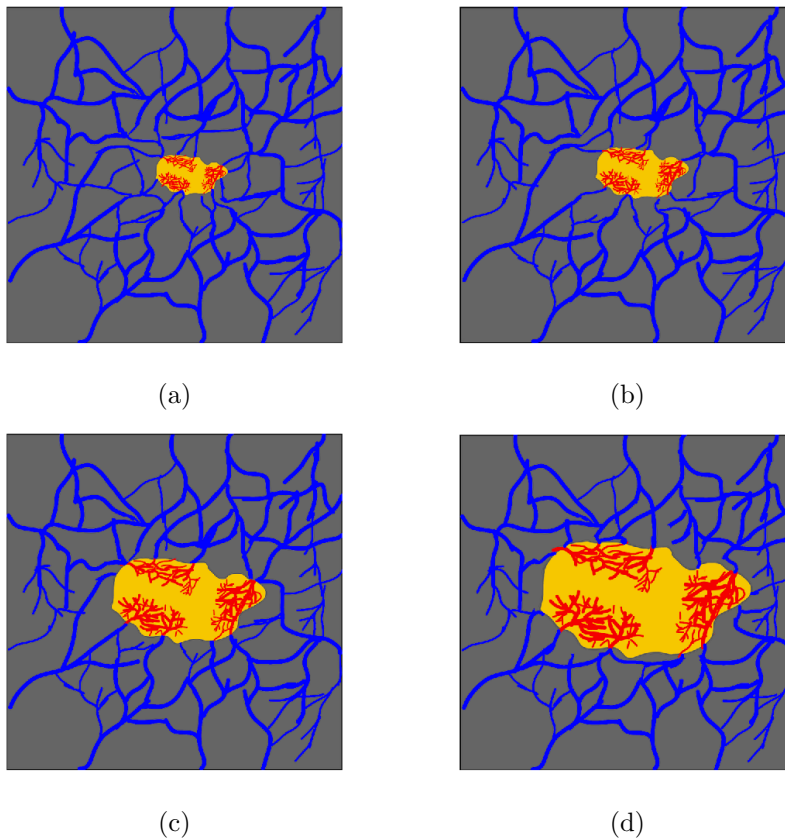


Figure 3.10: Different tumor sizes with the same MVD, vascular network structure, and tumor shape.

Fig. 3.11 and Fig. 3.12 demonstrate that increasing the tumor size raises both IFP and IFV. The average macromolecule concentration for different tumor sizes is shown in Fig. 3.13 (see also Video A.2 for spatiotemporal distributions). This figure shows that bigger tumors with the same MVD are seen to accumulate higher values of drug macromolecules, although they have higher IFV.

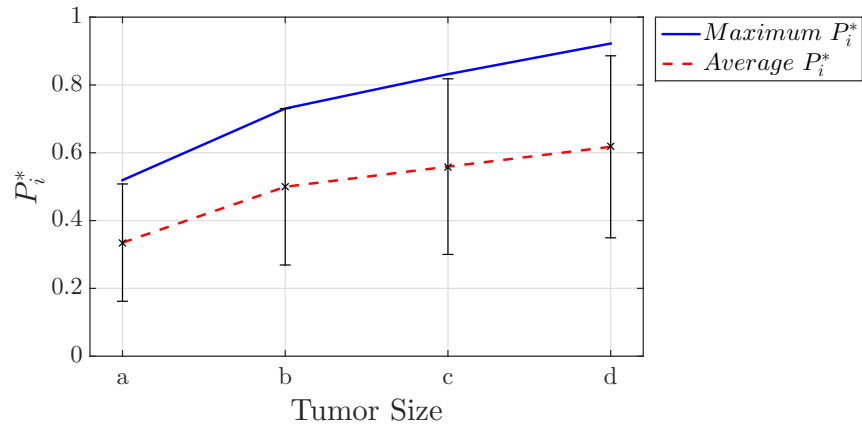


Figure 3.11: Maximum and average dimensionless IFP for tumors with the same MVD, vascular network structure, and tumor shape but different tumor size.

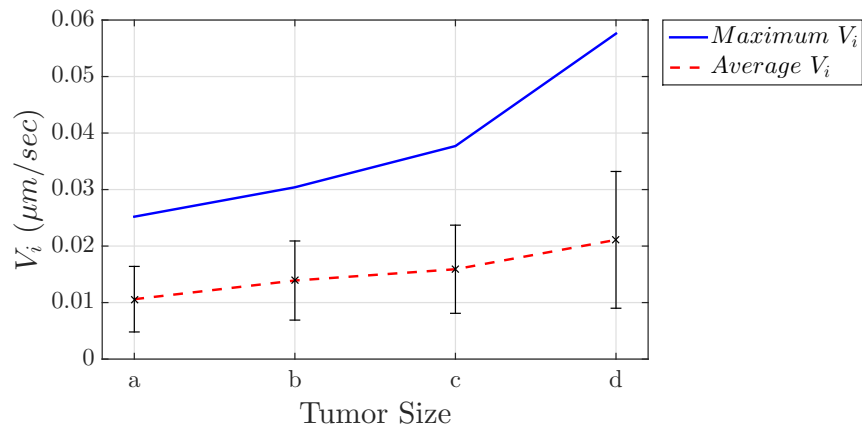


Figure 3.12: Maximum and average IFV ( $\mu\text{m}/\text{sec}$ ) for tumors with the same MVD, vascular network structure, and tumor shape but different tumor size.

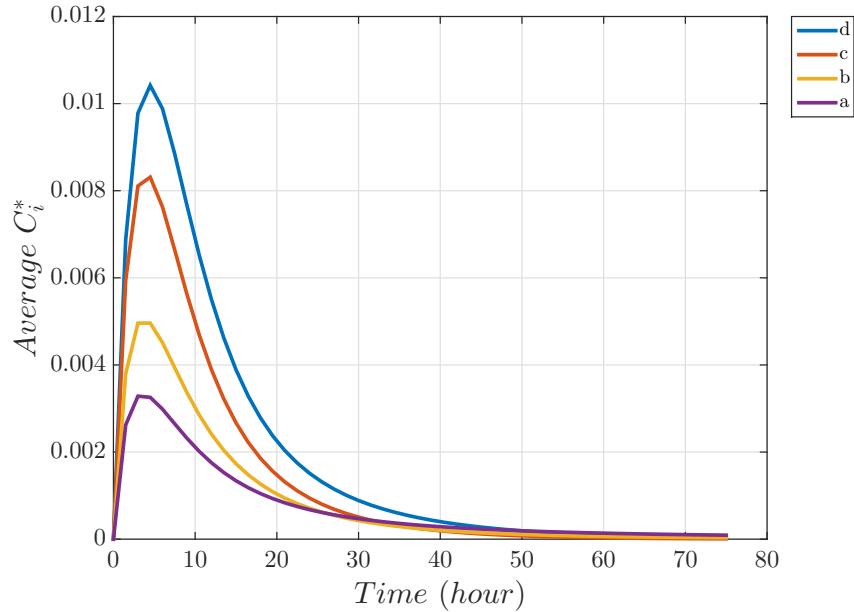


Figure 3.13: Average dimensionless concentration for tumors with different tumor sizes but the same MVDs, shape and vascular structure.

### 3.3.4 Effect of vascular location with constant MVD on IFP, IFV, and distribution of drug macromolecules

To investigate the effect of vascular location on IFP, IFV, and the distribution of drug macromolecules, three tumors with the same shape, size and MVD value, but different vascular structures are modeled (Fig. 3.14). In the first tumor, all vessel locations are close to the tumor periphery. In the second, half of the vessels are located close to the tumor periphery and the other half at its center. In the third, all vessels are located at the region close to the tumor center. IFV profiles for these cases are also presented in Fig. 3.14, demonstrating that the IFV distribution is highly correlated with the vessel locations.

Fig. 3.15 shows the average and the maximum value of IFP. Interestingly, the average value of IFP is the same in all three cases, but the maximum value of IFP increases when most of the vessels are located closer to the tumor center. Fig. 3.16 shows that change in the location of the vasculature has a very small effect on the IFV within the tumor.

Fig. 3.17 shows the average value of macromolecule concentrations over time for these three different tumor microenvironments (Video A.3 also shows the spatio-temporal distribution of macromolecule concentrations over time for these three cases). These figures also demonstrate that although changes in IFV are negligible on average, the concentra-

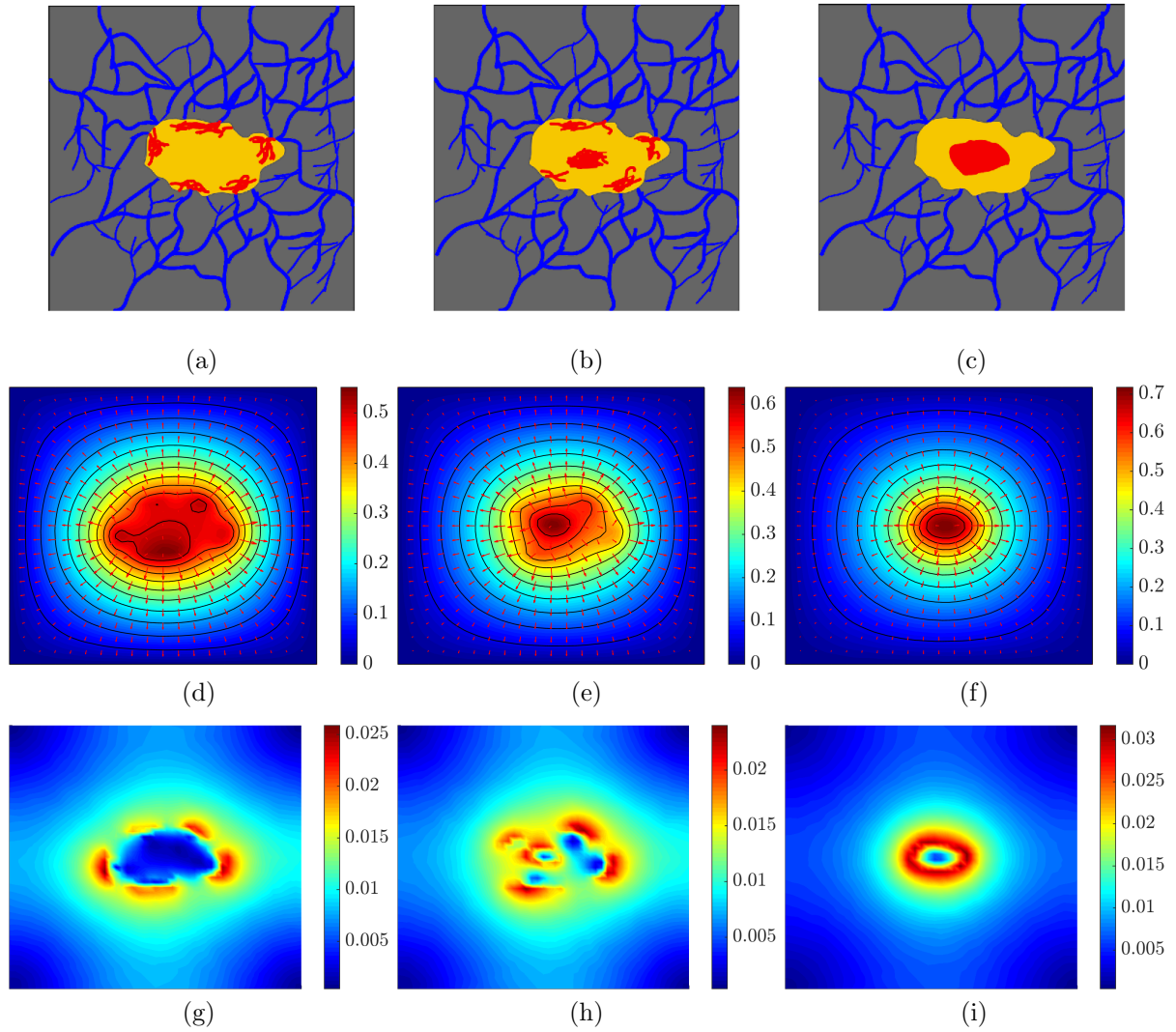


Figure 3.14: (a)–(c) Tumors with different locations of vessels but the same MVD, tumor size and shape, (d)–(f) show IFP , and (g)–(i) show IFV ( $\mu m/sec$ ) distribution for each tumor.

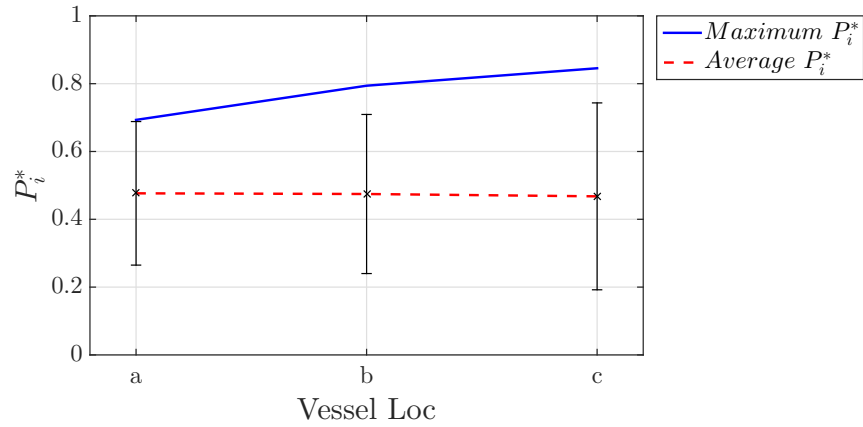


Figure 3.15: Maximum and average dimensionless IFP distribution for tumors with the same size, shape and MVD but different vessel locations.

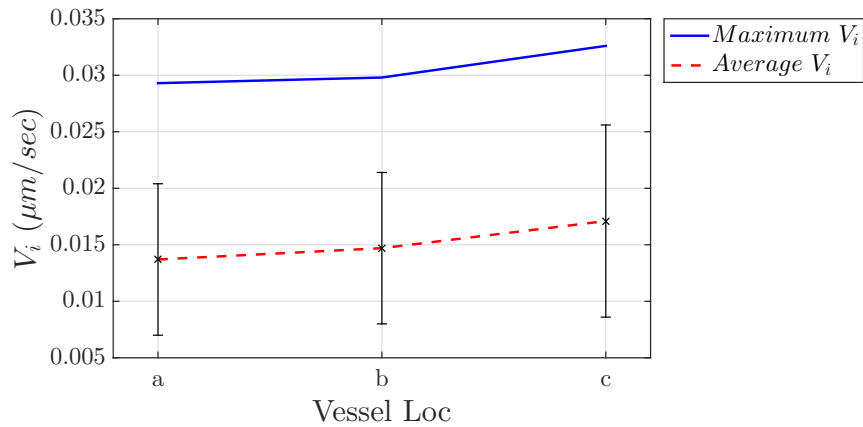


Figure 3.16: Maximum and average IFV ( $\mu\text{m}/\text{sec}$ ) distribution for tumors with the same size, shape and MVD but different vessel locations.

tion average values change significantly. The tumor with the vasculature at the center reaches a higher maximum value of drug concentration; however, 5 hours post-injection, the concentration values drop faster than in the two other cases.

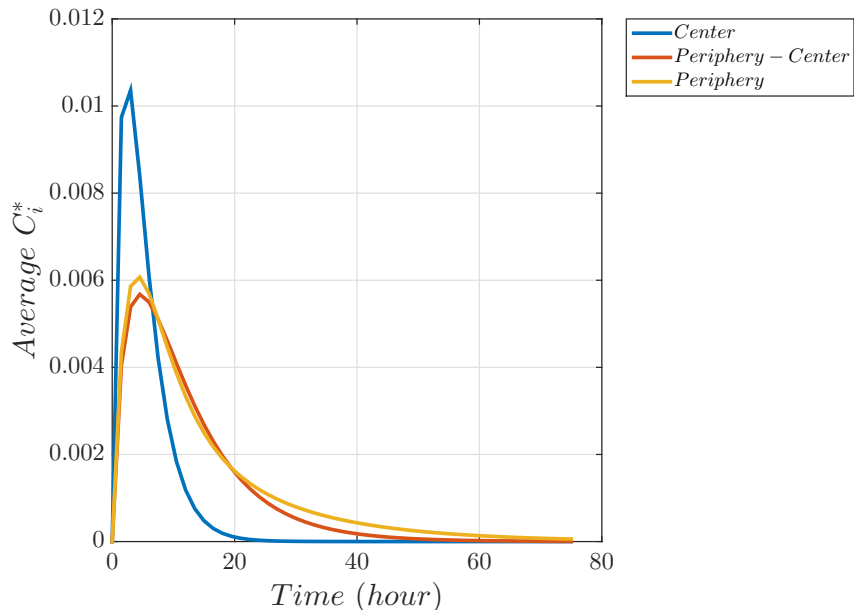


Figure 3.17: Average dimensionless concentration for tumors with the same size, shape and MVD but different vessel locations.

### 3.4 Discussion

Antiangiogenesis drugs decrease microvascular density (MVD) and tumor vessel pore size, resulting in the reduction of interstitial fluid pressure (IFP) [53, 40, 82]. Since this reduction in IFP depends on the tumor and vasculature’s physiological parameters, a quantitative approach that can be applied to a wide range of tumor and vascular types is essential.

Here, we have developed a computational framework to calculate IFP, IFV, and spatio-temporal distribution of macromolecules for general cases of tumor size and shape that have a typical vascular network structure. We found that IFP within the tumor not only depends on the MVD but also changes according to tumor size. IFP increases with increased MVD. For a constant MVD, bigger tumors show higher values of IFP. These findings are in agreement with recently published experimental work, in which Rofstad et al. [77] studied the association between MVD and IFP for R-18 and T-22 human melanoma cell lines.

They found that IFP increases nonlinearly with increased MVD. Moreover, we have used t-test for IFP values within tumors presented in Fig. 3.14 and found that, statistically, the location of vessels within a tumor has no significant effect on IFP on average; however, it can change the distribution of IFP. For the case where most of the vasculature is located at the tumor center, accumulation of fluid in the same region leads to a higher value of IFP at that region.

Comparing IFP distribution in Fig. 3.14 for three cases shows that there is a high correlation between the IFP distribution and the tumor vasculature distribution and that the maximum IFP is close to the region with the highest density of vasculature. This finding adds to the finding of the previous studies [5, 55] that have stated that the maximum IFP occurs at the tumor center. Furthermore, the maximum interstitial pressure is 0.9 when MVD is close to 1 (Fig. 3.7). Comparing this value with that for a spherical tumor with homogenous vasculature [5, 55], where vessels are everywhere inside the tumor, reveals that this difference may be a result of the effect of tumor shape on the IFP distribution and consequently on the maximum value of IFP.

High interstitial fluid velocity (IFV) at the tumor periphery and its outward flow from the tumor center result in drug macromolecule accumulating at the tumor periphery and prevent them penetrating from the vessels located at the tumor periphery to the cancerous cells far from the tumor edge. However, an IFV close to zero for regions far from the tumor periphery shows that if there are functional vessels inside the tumor, drug macromolecules can stay there, with no driving force to wash away them from that region. Therefore, it is important for antiangiogenesis drugs to mostly reduce the vessels close to the tumor periphery and leave vessels far from the tumor periphery intact.

Furthermore, We found that an increase of MVD leads to an increased accumulation of macromolecules. This finding is in agreement with recently published experimental data, in which Ekdawi et al. [29] found a significant positive correlation between liposome concentration, measured by volumetric analysis of CT data, and tumors' MVD. Although tumors with higher MVD present a higher accumulation of macromolecules in their interstitium, they also show a faster drop in drug concentrations about 5 hours post-injection. High MVD leads to increased IFP and associated IFV [67], resulting in faster depletion of macromolecules from tumor microenvironments. Moreover, MVD is not the only factor affecting the distribution of macromolecules; tumor size and vessel locations can also influence it. For the case where all vessels are located at the region close to the center of the tumor, macromolecules accumulate at the tumor center and form higher concentrations than occurring in the two other cases early post-injection. Despite this initially raised concentration, the concentration subsequently drops rapidly owing to high IFV values at the tumor center and a high concentration gradient. In contrast, for tumors with vasculature

at the tumor periphery, macromolecules are distributed more uniformly and stay longer within the tumor interstitium. We also found that the distribution of macromolecules is highly correlated with the pattern of vascular network within solid tumors; higher concentrations of macromolecules were found in locations with higher-density vasculature.

### 3.5 Conclusions

A general framework to calculate the spatio-temporal distribution of therapeutic agents and interstitial fluid velocity (IFV) in a typical tumor microenvironment has been presented. This framework can be applied on a high-resolution image of a specific tumor with its vasculature to follow chemotherapy drug distribution over period of treatment.

In agreement with experimental studies, we found that an increase in microvascular density (MVD) leads to elevation in IFP. Moreover, for a constant MVD, tumor size affects IFP values, and increased tumor size results in IFP elevation. We also found that an increase in both MVD and tumor size leads to higher drug accumulation early post-injection, but faster depletion thereafter. Furthermore, the vessel locations within a tumor affect the distribution of therapeutic agents. When vessels are located more uniformly, drug distribution is also more uniform with longer residence within the tumor interstitium. Furthermore, IFV and drug profile distribution are highly correlated with the vascular network structure, and the maximum of IFP and drug concentration occur at the region with the highest MVD. This observation generalizes the results of previous studies for a solid tumor with a homogenous vascular structure, in which the maximum of IFP occurs at the tumor center. Although the vascular morphology affects the IFP distribution within the tumor, the average value of IFP within the tumor is constant for tumors with constant MVD but different vessel locations. There are some limitations for this model. First, we have neglected the interactions between drug macromolecules and cancer cells, which may result in a higher drug accumulation within the tumor tissue. The advection-diffusion equation can be extended to reflect the effect of drugs that have high binding rates with cancer cells. We have also assumed constant blood pressure within the vascular network and neglected the effect of red blood cells, both of which can have effect on IFV, and therefore on drug macromolecule distribution. A constant hydraulic conductivity is assumed for tumor tissue, which can be modified for cases with heterogeneously compacted tumor tissue. This study provides insights related to the administration of anti-angiogenesis drugs that alter the MVD and vascular structure within tumor microenvironments. Our computational framework can determine how these changes affect chemotherapy and drug distribution within a specific solid tumor.

# Chapter 4

## Determination of Optimal Chemotherapy Dosage in Solid Tumors

### 4.1 Introduction

Tumor microenvironments are heterogenous due to phenomena such as angiogenesis and vessel collapse. Angiogenesis occurs because solid tumors in need of extra oxygen and nutrients send chemical signals to neighboring vessels, stimulating them to form neovasculature towards the tumor edge [16, 17]. In contrast to vessels in normal tissue, these new vessels are weak, leaky, and have a dense abnormal structure. Within tumors, however, the high proliferation of cancer cells and lack of space lead to tightly compacted environment. This compactness applies stresses on vessels and the lymphatic system within a tumor, resulting in their collapse [10, 83]. Leaky vasculature and the lack of lymphatic drainage within solid tumors result in enhanced permeability and retention (EPR) [75, 54]. To take advantage of EPR, liposomes have been widely used to encapsulate therapeutic agents for higher efficiency in drug delivery and less toxicity to normal cells compared with conventional chemotherapy [26]. Encapsulated drugs such as Doxil can penetrate from leaky vessels into tumor tissue and stay there for a long time due to their low diffusivity [102] and the lack of drainage. Eventually, the nanoparticles release the drugs in a controlled way so that they can travel freely within the tumor interstitium, bind to cancer cells and be internalized within them. The amount of drug nanoparticles that reach cancer cells determines the efficacy of treatment; thus determining the correct drug dosage is crucial:

too low a dosage can result in unsuccessful treatment, whereas too high a dosage can be very toxic. Therefore, chemotherapy protocols set limits on anti-cancer drug dosages to minimize toxicity to normal cells while maximizing the annihilation of cancer cells [20]. Chemotherapy regimens define the frequency and dosage of drugs to be delivered [57].

Using randomized clinical and pre-clinical trials to find the most effective regimen for nanoparticle injection is costly and lengthy. Moreover, tumor physiological properties such as vascular structure, vessel permeability and hydraulic conductivity of the interstitium, as well as drug nanoparticle properties such as size, shape and rate of drug release, can also affect the amount of drug that reaching cancer cells [19, 82, 67, 97, 100]. Taking into account all of these factors when attempting to find the most effective regimen is almost impossible in clinical and preclinical trials. However, these limitations of experimental studies can be overcome using mathematical modeling. Several studies have defined finding optimal regimens to be an optimal control problem [65, 64, 86, 85, 1]. They introduced models for tumor growth and also drug toxicity and resistance, with the goal of finding the best injection policy that minimizes the tumor burden over a specific treatment period while satisfying the toxicity and resistance limitations. Although these models give some insights about how different injection approaches alter the effectiveness of chemotherapy, they do not take into account tumor microenvironment heterogeneity and the biophysical properties of therapeutic agents.

Clinical and preclinical studies have demonstrated that the delivery of liposomes to solid tumors occurs differently from one patient to another, even if both have the same type of tumor, owing to high variation in the heterogeneity of tumor microenvironments [27, 43]. Some studies have also shown that the differences in tumor microenvironments, including in microvascular morphology and permeability, result in variations in EPR and liposome accumulation [79, 89, 75]. Due to the crucial role of tumor microenvironments, especially their vascular structure, recent studies have used high resolution imaging such as photoacoustic tomography (PAT), magnetic resonance imaging (MRI), diffusion-weighted magnetic resonance imaging (DW-MRI), and computed tomography (CT) to investigate the effect of tumor physiological properties on different phenomena within tumors, such as angiogenesis [91], the response of vascular structure to anti-angiogenesis therapy [30], and changes in interstitial fluid pressure (IFP) [48, 49, 78].

In this study, we introduce a computational framework for finding the optimal regimen for delivering injected drug nanoparticles to a specific tumor microenvironment. First, a drawing-based approach is utilized to model the tumor microenvironment, assuming to be an ideal tumor image. This tumor model can be produced using high-resolution images of the solid tumor under treatment taking using methods such as photo-acoustic tomography (PAT) [91], magnetic resonance imaging (MRI), and computed tomography (CT). Then, to

consider the effect of different tumor physiological parameters on nanoparticle transport, we use specific transport phenomena equations: Darcy’s law and the continuity equation, to calculate the fluid movement within the tumor interstitium; Starling’s equation, to model the transport of drug nanoparticles across the vessel wall; and the advection-diffusion equation, to calculate the transport of nanoparticles within the tumor tissue, and also their bindings to cancer cell receptors and their internalization. We can then find the optimal dosage schemes, in which drug injections happen consistently at the correctly time intervals to maximize cancer cell eradication over a specific period of treatment, while the dosage are limited such that the toxicity level can be tolerated by the patient. Finally, this framework is applied to two different case studies: conventional chemotherapy and liposome drugs.

## 4.2 Tumor microenvironment model

In setting optimal chemotherapy protocols, drug dosages depend on the tumor microenvironment and the mechanisms of therapeutic agent transport within this microenvironment. This section presents a physiologically relevant tumor model and uses it as the basis for a computational framework that is able to determine the optimal amount of chemotherapy drug to be injected at constant time intervals over a specified period of treatment.

The heterogeneous structure of the vasculature in solid tumors results from different phenomena such as angiogenesis and vessel regression. Growing tumors send chemical signals to neighboring vasculature in normal tissue to form new vessels through which extra oxygen and nutrients can be provided [47, 53, 32, 12]. This phenomenon, called angiogenesis, leads to high microvascular density (MVD) at the tumor periphery. In contrast, within the tumor and far from the tumor edge, the high proliferation of cancer cells apply normal stresses to the vessel walls, leading to vessel collapse [10, 83, 95], and therefore, low MVD at the tumor center [67, 77]. Here, we have utilized a schematic tumor microenvironment (Fig. 4.1) as an image of a tumor and its vasculature. In this figure, the vasculature is heterogeneous and has a regular structure in normal tissue (blue lines) but irregular structure within the tumor (red lines). It also presents the MVD reduction from the tumor periphery toward the tumor center, imitating real tumor microenvironments.

The tumor model presented in Fig. 4.1 is used as a basis to investigate the the optimal chemotherapy regimen for two cases of chemotherapy using free drugs and chemotherapy of drugs encapsulated in liposomes.

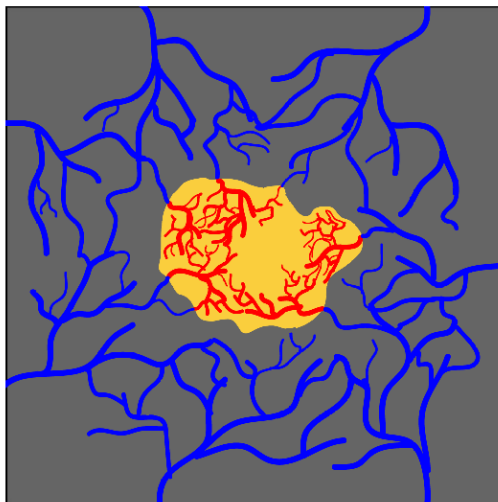


Figure 4.1: A typical tumor microenvironment, including solid tumor, normal tissue and vasculature. Vessels are blue in normal tissue and red within tumor.

### 4.3 Case I: Optimal regimen of conventional chemotherapy

Transport of drug nanoparticles within tumor microenvironments includes multiple steps. After being injected intravenously, drug nanoparticles, suspended in the blood flow, are carried by blood vessels to the tumor site, then extravasate into the tumor interstitium by crossing through the vessel wall. Once they are within tumor tissue, these drug nanoparticles move freely due to the concentration gradient and convection by interstitial fluid flow. They can also bind to cancer cell receptors and then be internalized within them.

#### 4.3.1 Methods

##### Drug transport modeling

Each step of drug transport can be modeled mathematically. When traveling through blood vessels, the concentration of drug nanoparticles decays due to blood clearance [5]. The dynamic of drug concentration inside plasma can be described by the following equation:

$$\frac{dC_p}{dt} = \xi(t) - \frac{1}{\tau}C_p \quad (4.1)$$

where  $C_p$  is the plasma concentration of drug nanoparticles,  $\xi(t)$  is the rate of drug injection ( $M/hr$ ) and  $\tau$  corresponds to drug's half-life in plasma. For numerical purposes, this equation can be written as

$$\delta C_p = u(t) - \frac{1}{\tau} C_p \delta t \quad (4.2)$$

where, using bolus injection,  $u(t) = \xi(t)\delta t$  is the amount of drug enters to plasma at the short time interval of  $\delta t$ .

The transport of the drug nanoparticles within the tumor interstitium, their bindings to cancer cell receptors, and the internalization within cancer cells can be described by following equations [82]:

- Concentration of free drug within interstitium:

$$\frac{\partial C_f}{\partial t} + \nabla \cdot (u_i C_f) = \begin{cases} D_f \nabla^2 C_f - \frac{1}{\phi} K_{on} C_e C_f + K_{off} C_b + \phi_S & \text{for vasculature} \\ D_f \nabla^2 C_f - \frac{1}{\phi} K_{on} C_e C_f + K_{off} C_b & \text{elsewhere} \end{cases} \quad (4.3)$$

- Concentration of drug bound to cancer cell receptors:

$$\frac{\partial C_b}{\partial t} = \frac{1}{\phi} K_{on} C_e C_f - (K_{off} + K_{int}) C_b \quad (4.4)$$

- Concentration of internalized drug

$$\frac{\partial C_{int}}{\partial t} = K_{int} C_b \quad (4.5)$$

where  $u_i$  is the interstitial fluid pressure, which can be calculated using equations introduced in [Sec. 2.3.1](#);  $D_f$  is the diffusion coefficient of the free drug;  $C_f$ ,  $C_b$ ,  $C_{int}$ , and  $C_e$  are the concentration of free drug, bound drug, internalized drug, and cancer cell receptors, respectively;  $K_{on}$ ,  $K_{off}$ , and  $K_{int}$  are rate constants for drug binding to cancer cell receptors, unbinding, and internalization within cancer cells, respectively;  $\phi$  is the tumor volume fraction that can be reached by the drug nanoparticles;  $\phi_S$  is the amount of drug traveling across vessel walls and can be calculated using Starling's equation [5]:

$$\phi_S = L_P \frac{S}{V} (P_V - P_i) (1 - \sigma) \frac{C_p e^{Pe} - C_f}{e^{Pe} - 1} \quad (4.6)$$

where  $Pe = L_P(1 - \sigma)\frac{(P_V - P_i)}{P}$  is the Peclet number, and  $P$  ( $cm/sec$ ) is the vessel permeability.

## Initial and boundary conditions

Initial conditions as well as boundary conditions are necessary to solve [Eq. 4.3](#), [Eq. 4.4](#), and [Eq. 4.5](#). For the initial conditions, the concentrations are zero at the time of first injection:

$$(C_f, C_b, C_{int})|_{t=0} = 0 \quad (4.7)$$

The two boundary conditions for [Eq. 4.3](#) are that the free drug concentration is continuous at the boundary of the tumor and normal tissue and that the concentration is zero at the domain edges:

$$C_f|_{\Omega^-} = C_f|_{\Omega^+} \quad (4.8)$$

$$C_f|_{x=0,L} = C_f|_{y=0,L} = 0 \quad (4.9)$$

The parameter values used in these equations are listed in [Tab. 4.1](#).

## Optimal scheduling of chemotherapy

Therapeutic agents can be delivered to patients by injection of different dosages and frequencies. The goal of chemotherapy regimens is to kill as many cancer cells as possible, with a minimum toxicity to normal cells. The fraction of surviving cells ( $S_F$ ) when the drug doxorubicin is used relates to the internalized drug concentration ( $C_{int}$ ), which is given by [\[81\]](#):

$$S_F = \exp(-10^6 \cdot \omega \cdot C_{int}) \quad (4.10)$$

where  $\omega = 0.4938$ . This equation is fitted based on the experimental data for doxorubicin [\[58\]](#). The number of killed cancer cells based on [Eq. 4.10](#) is  $(1 - S_F)$ . The total time of treatment is assumed to be  $T$ , and the bolus injections with the amount of  $\{u_i\}_{i=1}^n$  are assumed to happen at  $n$  fixed times  $\{t_i\}_{i=1}^n$ , where  $\Delta t = t_i - t_{i-1}$ , the time interval between successive injections, is constant. Therefore,  $u(t)$  is described as

$$u(t) = \begin{cases} u_1 & \text{if } t = t_1 = 0 \\ u_2 & \text{if } t = t_2 \\ \vdots & \\ u_n & \text{if } t = t_n < T \end{cases} \quad (4.11)$$

Table 4.1: Model parameter values used in our computation

Parameter	Tissue	Baseline value	Reference
$L_p [cm/mmHg.s]$	Normal	$4 \times 10^{-10}$	calculated from [81]
	Tumor	$4 \times 10^{-8}$	calculated from [81]
$K [cm^2/mmHg.s]$	Normal	$8.5 \times 10^{-9}$	[84]
	Tumor	$4.1 \times 10^{-8}$	[5]
$S/V [cm^{-1}]$	Normal	70	[74]
	Tumor	200	[45]
$\sigma$	Normal	0.0427	calculated from [81]
	Tumor	$4.6 \times 10^{-4}$	calculated from [81]
$P [cm/s]$	Normal	$2.1 \times 10^{-7}$	calculated from [81]
	Tumor	$3.1 \times 10^{-7}$	calculated from [81]
$\tau [hr]$	Plasma	15	[90]
$D_f [cm^2/sec]$		$3 \times 10^{-6}$	[81]
$K_{on} [M^{-1}s^{-1}]$		$1 \times 10^3$	[82]
$K_{off} [s^{-1}]$		$8 \times 10^{-3}$	[82]
$K_{int} [s^{-1}]$		$5 \times 10^{-5}$	[82]
$C_e [M]$		$1 \times 10^{-5}$	[82]
$\phi$		0.3	[82]

Table 4.2: The value of parameters used in optimization problem

Parameter	value
$T$ [hr]	400
$\Delta t$ [hr]	30
$n$	6
$u_{max}$ [M]	$1 \times 10^{-2}$
$u_{accum}^{max}$ [M.hr]	$7 \times 10^{-4}$

Some constraints can be placed on the amount of drug injected, to guarantee that the toxicity level can be tolerated by the patient under treatment. First, the amount of drug injected should be less than the maximum value  $u_{max}$

$$0 < u(t) < u_{max} \quad \text{for all } 0 < t < T \quad (4.12)$$

Second, the amount of a drug delivered over the period of treatment should be less than the maximum value  $u_{accum}^{max}$

$$\int_0^T \int_R C \, dAdt < u_{accum}^{max} \quad (4.13)$$

where  $C = (C_f + C_b + C_{int})$ , and  $R$  is the tumor microenvironment region. Therefore, the optimization problem is to find  $\{u_i\}_{i=1}^n$  values that maximize the fraction of killed cancer cells after the period of treatment, while satisfying the toxicity constraints presented in Eq. 4.12 and Eq. 4.13:

$$\text{Maximize } J(u_1, \dots, u_n) = (1 - S_F(T)) \quad (4.14)$$

The resulting  $\{u_i\}_{i=1}^n$  values are the optimal drug dosages that should be injected at the times fixed by  $\{t_i\}_{i=1}^n$ .

## Optimization method

We found that the gradient-based and trust-region [68, 13, 61] optimization algorithms do not converge to an optimum solution and stay around the initial guess for this optimal regimen problem. Therefore, to have a higher chance of finding the optimal solution, we use Genetic Algorithm (GA) [34, 22, 31], which is a heuristic optimization algorithm. GA has been used in a wide range of applications such as water resource system designs [104],

DNA sequencing [41], and control engineering [72, 62]. The advantage of GA is a very high chance of finding the best optimal solution. However, its disadvantage is that it is very slow compared with gradient-based algorithms. Global Optimization toolbox of MATLAB is used to implement GA for our optimal regimen problem. In GA algorithm, we use default values from the toolbox except that “the number of generations” and “population size” are set to 100 and 20, respectively.

### 4.3.2 Results

Two approaches for the delivery of therapeutic agents are used here: bolus injection and continuous infusion. To find the optimal dosages for these two approaches, we have utilized the tumor microenvironment presented in Fig. 4.1 as the tumor under treatment. It is assumed that the total time for the treatment ( $T$ ) is 400 hours, and that six injections happen at constant time intervals of 30 hrs,  $t_i = \{0, 30, 60, 90, 120, 150\}$ . To avoid toxicity, we assume that the maximum concentration that can be injected ( $u_{max}$ ) is 0.01  $M$  and that the maximum total accumulated therapeutic agents ( $u_{accum}^{max}$ ) is half of the accumulated drugs when the maximum drug concentrations are applied with each injection, ( $1.4 \times 10^{-3}$ ). The parameters used to find the optimal dosages are listed in Tab. 4.2.

#### Optimal chemotherapy regimen for bolus and continuous infusion

An optimization algorithm has been utilized to find the injection dosages that maximize the fraction of killed cancer cells, but stay in a range that satisfies the toxicity constraints of Eq. 4.12 and Eq. 4.13. The optimized dosages when bolus injection is applied are  $u_i = \{0.54, 0.48, 0.77, 0.15, 0.73, 0.32\} \times 10^{-2}$ , which leads to eradication of 62% of the cancer cells. Moreover, the optimize dosages when continuous infusion is applied are found to be  $u_i = \{0.58, 0, 0.20, 0.64, 0.05, 0\} \times 10^{-2}$ , leading to the same degree of eradication as when bolus injections are applied (62%). The spatio-temporal concentration distributions of therapeutic drugs in tumor tissue, and bound and internalized drugs, when optimal bolus injections are applied, are shown in Fig. 4.2, Fig. 4.3, and Fig. 4.4, respectively (see also Video A.4). It should be noted that all concentration results in this section are normalized (divided by  $u_{max}$ ). Additionally, Fig. 4.5 shows how the fraction of killed cancer cells increases over time and space. To compare the results for bolus injection and continuous infusion, the drug concentration within plasma, the average concentration of the drug within tumor microenvironment, the bound and internalized drugs, as well as the fraction of killed cancer cells over time are shown in Fig. 4.6. This figure demonstrates that the average concentrations of drugs within the tumor have very similar trend to that

Table 4.3: The optimal dosages (normalized to  $u_{max}$ ) applied for bolus injections for different blood half-life values of drugs

$\tau$	$\{u_i^*\}_{i=1}^6$	$1 - S_F(T)$
5	{0.98, 0.96, 0.9963, 0.90, 0.97, 0.94}	0.46
15	{0.54, 0.48, 0.77, 0.15, 0.73, 0.32}	0.62
500	{0, 0, 0.11, 0.12, 0.004, 0.001}	0.59

drug concentrations within plasma for both bolus and continuous injection. In contrast, the average concentration for bound drugs consistently increases over time, until about 150 hours after the first injection, and then decreases. Additionally, the average concentration for the internalized drugs and the fraction of killed cancer cells ascend over time. This figure also reveals that despite the different injected concentrations for bolus and continuous infusion, the bound and internalized drugs show quite similar trends in their average concentration, which leads to the same efficacy.

### Effect of the blood half-life of therapeutic agents on optimal regimens

The shape, size and other biophysical properties of therapeutic agents affect their distribution within tumors and their efficacy. In this section, we investigate how the blood half-life of a drug can result in different optimal dosages and consequent distributions within a tumor microenvironment. The strategy for finding optimal dosages is applied to cases, each with a different blood half-life of  $\tau = \{5, 15, 500\}$  hours. Tab. 4.3 shows the optimal dosages and the fraction of killed cancer cells when bolus injection is used. Average concentrations and the fraction of killed cancer cells over time for different  $\tau$  values are presented in Fig. 4.7. This figure and the table show that the dosages near the maximum allowed concentration ( $u_{max}$ ) are applied for the case with the lowest blood half-life, whereas, the dosages are very small and close to zero for the case with ( $\tau = 500$ ). Despite the very low injected dosages, the drug with ( $\tau = 500$ ) has high bound and internalized concentration values, comparable to those values of drug with ( $\tau = 15$ ), and more than those of drug with ( $\tau = 5$ ). Thus, the optimal dosages results in the highest efficacy for the drug with ( $\tau = 15$ ) and ( $\tau = 500$ ). The figure also shows that the concentrations of drugs within a tumor and bound drugs are in the same range, but are two orders of magnitude bigger than the internalized drug concentrations.

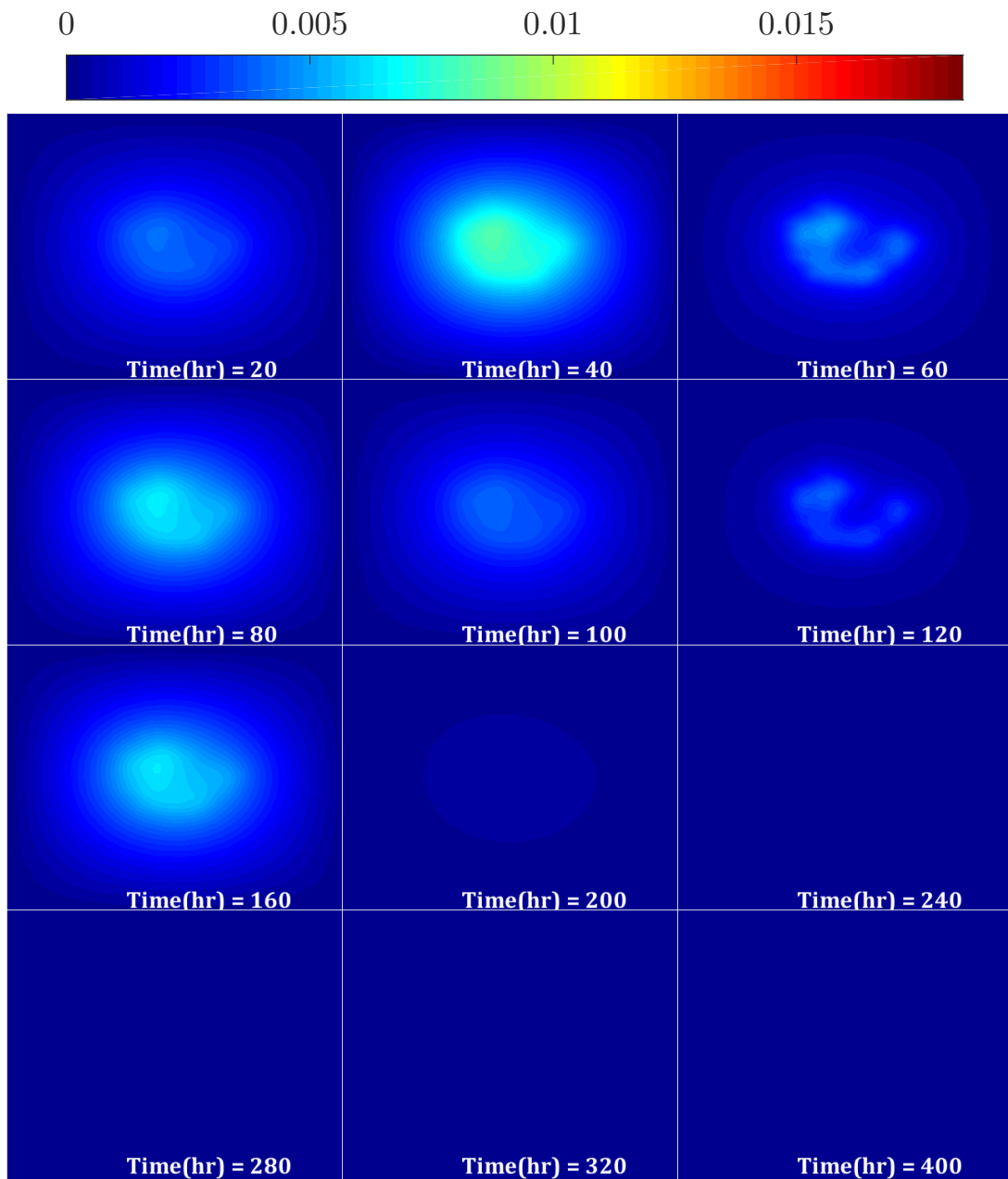


Figure 4.2: Normalized concentration profile of free drugs ( $C_f^*$ ) when optimal bolus injections are applied; injection times (*hour*) are  $t_i = \{0, 30, 60, 90, 120, 150\}$ .

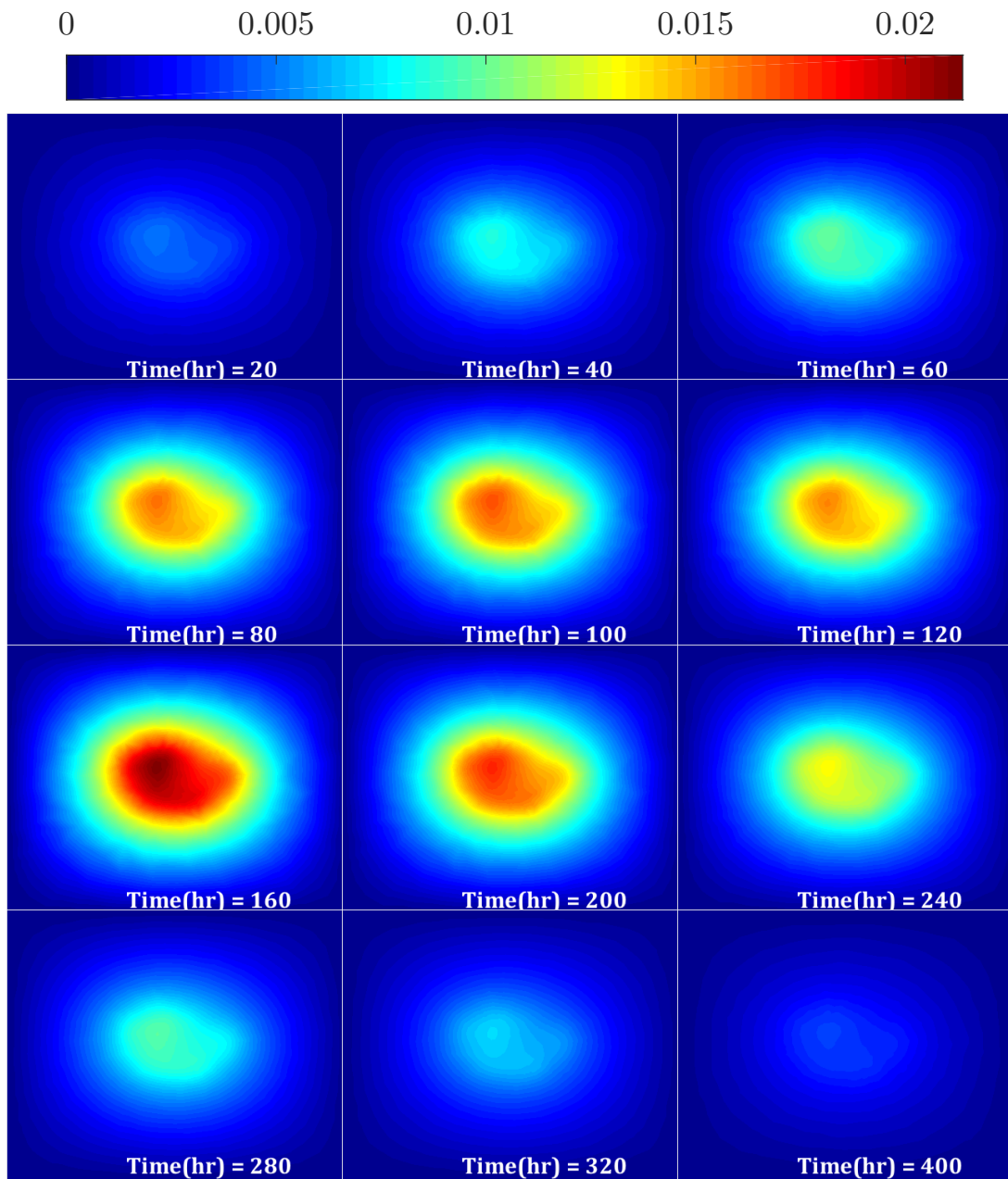


Figure 4.3: Normalized concentration profile of bound drugs ( $C_b^*$ ) when optimal bolus injections are applied; injection times (*hour*) are  $t_i = \{0, 30, 60, 90, 120, 150\}$ .



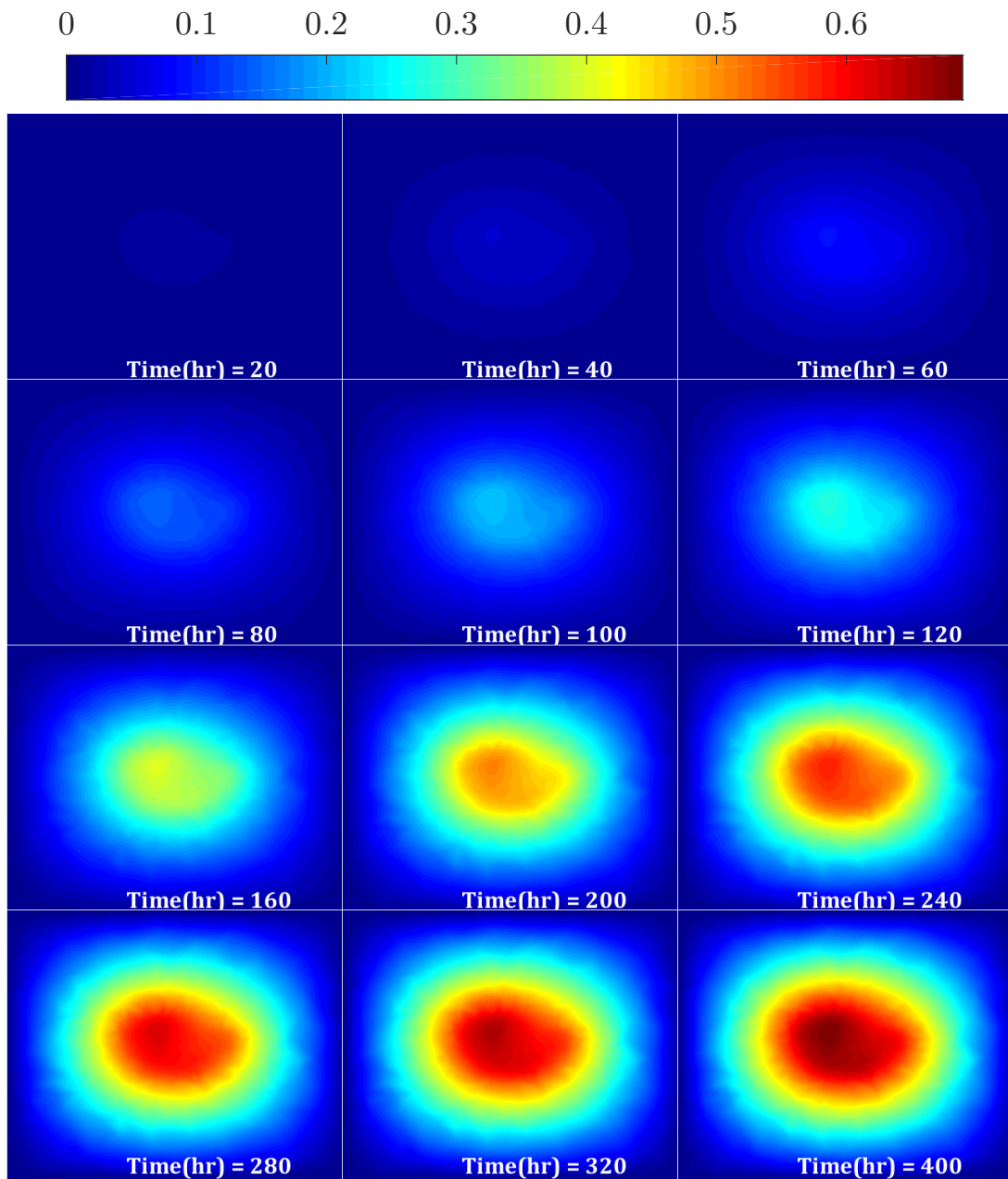


Figure 4.5: Fraction of killed cancer cells when optimal bolus injections are applied; injection times (*hour*) are  $t_i = \{0, 30, 60, 90, 120, 150\}$ .

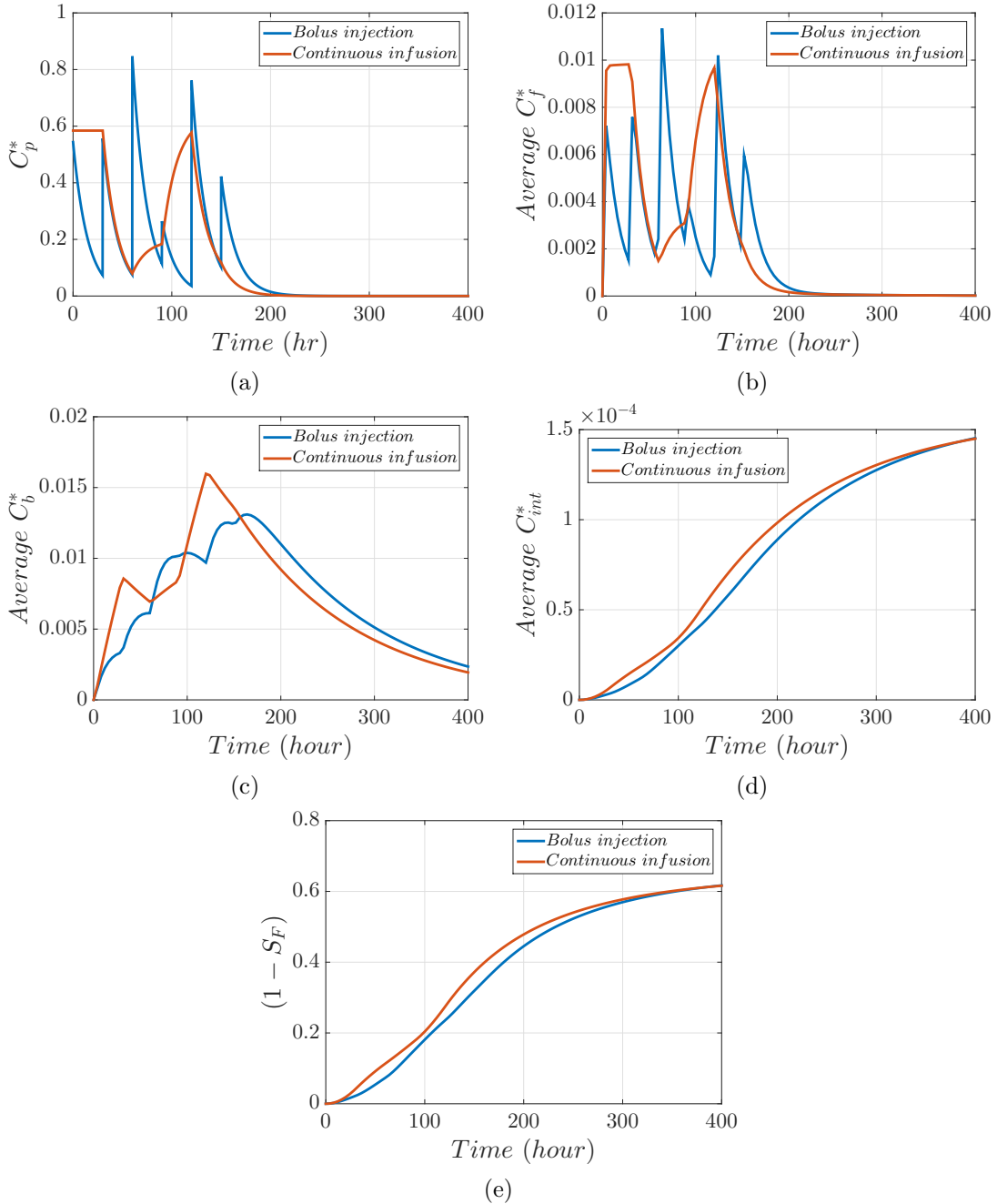


Figure 4.6: Results from optimal regimens for bolus and continuous infusion strategies: (a) normalized drug concentration within plasma, (b) normalized drug concentration within tumor tissue, (c) normalized concentration of bound drugs, (e) normalized concentration of internalized drugs, and (f) fraction of killed cancer cells

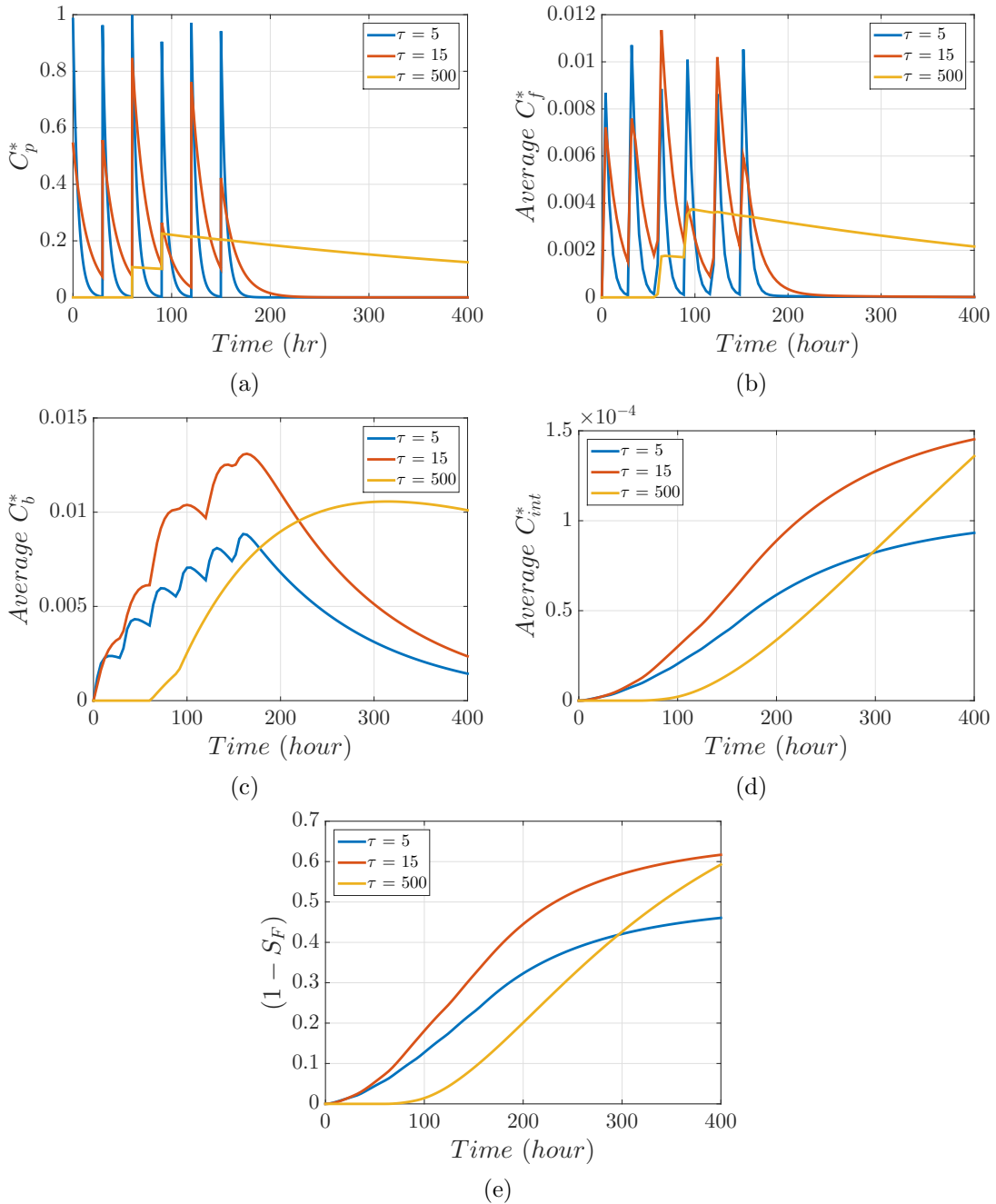


Figure 4.7: Results from optimal regimens for different  $\tau$  values of drugs: (a) drug normalized concentration within plasma, (b) drug normalized concentration within tumor tissue, (c) normalized concentration of bound drugs, (d) normalized concentration of internalized drugs, and (f) fraction of killed cancer cells

Table 4.4: The optimal dosages (normalized to  $u_{max}$ ) applied for bolus injections for different drug diffusion coefficients

$D_f$	$\{u_i^*\}_{i=1}^6$	$1 - S_F(T)$
$1 \times 10^{-8}$	{0.90, 0.99, 0.70, 0.87, 0.38, 0.97}	1
$3 \times 10^{-6}$	{0.54, 0.48, 0.77, 0.15, 0.73, 0.32}	0.62
$1 \times 10^{-4}$	{0.31, 0.93, 0.02, 0.49, 0.82, 0.27}	0.07

### Effect of the diffusivity of therapeutic agents on optimal regimens

One important mechanism of the movement of therapeutic agents within tumor tissue is diffusion. Diffusivity affects the residence time of drugs within tumor tissue and consequently affects the number of bound particles and the concentration of drugs internalized in cancer cells. This section investigates how different drug diffusion coefficients change optimal dosages and drug efficacy. The optimal dosages obtained and the fraction of killed cancer cells at the end of treatment for the drugs with diffusion coefficients  $D_f = \{10^{-8}, 3 \times 10^{-6}, 10^{-4}\}$  are presented in [Tab. 4.4](#). Concentrations of drugs within tumor, bound and internalized drugs, and also the fraction of killed cancer cells over time are shown in [Fig. 4.8](#). The table and figure demonstrate that there are no tangible differences between the optimal dosages obtained. However, the concentration values for the drugs within a tumor, bound and internalized prove that the drug with the lowest diffusion coefficient ( $D_f = 10^{-8}$ ) has the highest drug concentration. Moreover, the drug with the ( $D_f = 10^{-8}$ ) leads to eradication of all cancer cells, while the one with the highest diffusivity ( $D_f = 10^{-4}$ ) kills only 7% of them.

### Effect of binding rate of the therapeutic agents with cancer cell receptors on the optimal regimen

The rates at which drugs bind and unbind to cancer cell receptors impact their internalized concentration in cancer cells and consequent effectiveness. Here, we investigate the results of changing the drug binding rate so:  $K_{on} = \{10, 10^2, 10^3\}$ . The optimal dosages and the efficacy of drugs for these different cases are presented in [Tab. 4.5](#). The average values of drug concentration within plasma, tumor tissue, bound and internalized drug, and the fraction of killed cancer cells over time are shown in [Fig. 4.9](#). The table shows that the increased  $K_{on}$  leads to a reduced dosages of injected drugs. Concentration within the tissue has a trend similar to the concentration within plasma. However, the bound and internalized concentrations are the highest for the the drug with the highest binding rate

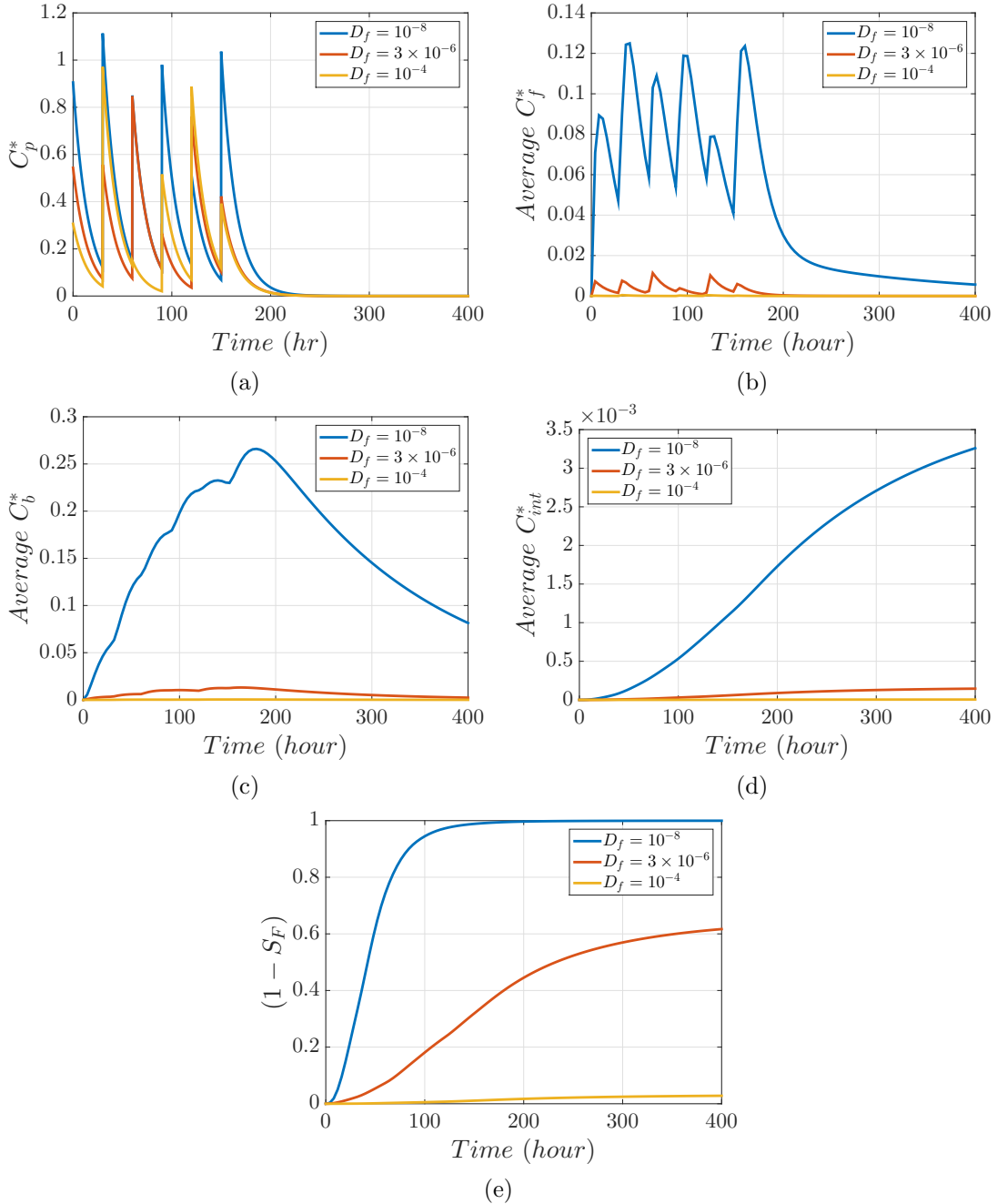


Figure 4.8: Results from optimal regimens for different diffusivity values of therapeutic agents: (a) drug normalized concentration within plasma, (b) drug normalized concentration within tumor tissue, (d) normalized concentration of bound drugs, (e) normalized concentration of internalized drugs, and (f) fraction of killed cancer cells

Table 4.5: The optimal dosages (normalized to  $u_{max}$ ) applied for bolus injections for different drug binding rates

$K_{on}$	$\{u_i^*\}_{i=1}^6$	$1 - S_F(T)$
10	{0.88, 0.90, 1, 0.97, 0.95, 0.99}	0.02
$10^2$	{0.97, 0.98, 0.90, 0.99, 0.76, 0.91}	0.16
$10^3$	{0.54, 0.48, 0.77, 0.15, 0.73, 0.32}	0.62

( $K_{on} = 10^3$ ). Consequently, the drug with the highest binding rate leads to the highest efficacy (62% of killed cancer cells at the end of treatment), while the drug with the lowest binding rate ( $K_{on} = 10$ ) kills only 2% of cancer cells.

### 4.3.3 Discussion

We have developed a method for finding the optimal dosages for therapeutic agents to be injected either using bolus injection or continuous infusion. Previous studies on optimal chemotherapy regimens [69, 28, 44] have examined only the effect of drug concentration within plasma and toxicity effects, and the tumor microenvironment has been considered as a lump, where the mixing of drug with plasma is immediate and delivery to the tumor is instantaneous. However, the physiological properties of tumor microenvironments, such as the hydraulic conductivity of tumors, vascular density, and morphology, impact drug distribution with [9, 71, 97, 67], and therefore, their effects are incorporated in our study. Moreover, drug biophysical properties such as blood half-life and their diffusivity within tumor and normal tissue are integrated into the presented model.

We found that although the optimal dosages for bolus injection and continuous infusion are quite different, they lead to the same fraction of cancer cells being eradicated. Therefore, it can be concluded that if the tumor microenvironment and drug properties are the same, different injection strategies (bolus or continuous) – used with optimal drug dosages – result in the same efficacy. As demonstrated in Fig. 4.7, change in the blood half-life of a drug alters the resulting optimal drug dosages; a higher blood half-life results in lower drug dosages and a lower blood half-life results in higher dosages. However, this change in drug dosages has an insignificant consequence on drug efficacy, as the fraction of killed cancer cells increases by only 3% when drug blood half-life changes from 500 hour to 15 hour. In contrast, Fig. 4.8 indicates that change in the diffusion coefficient of a drug does not alter the optimal applied dosages, but does significantly affect drug efficacy; the fraction of killed cancer cells increases from 7% to 100% when drug the diffusion coefficient

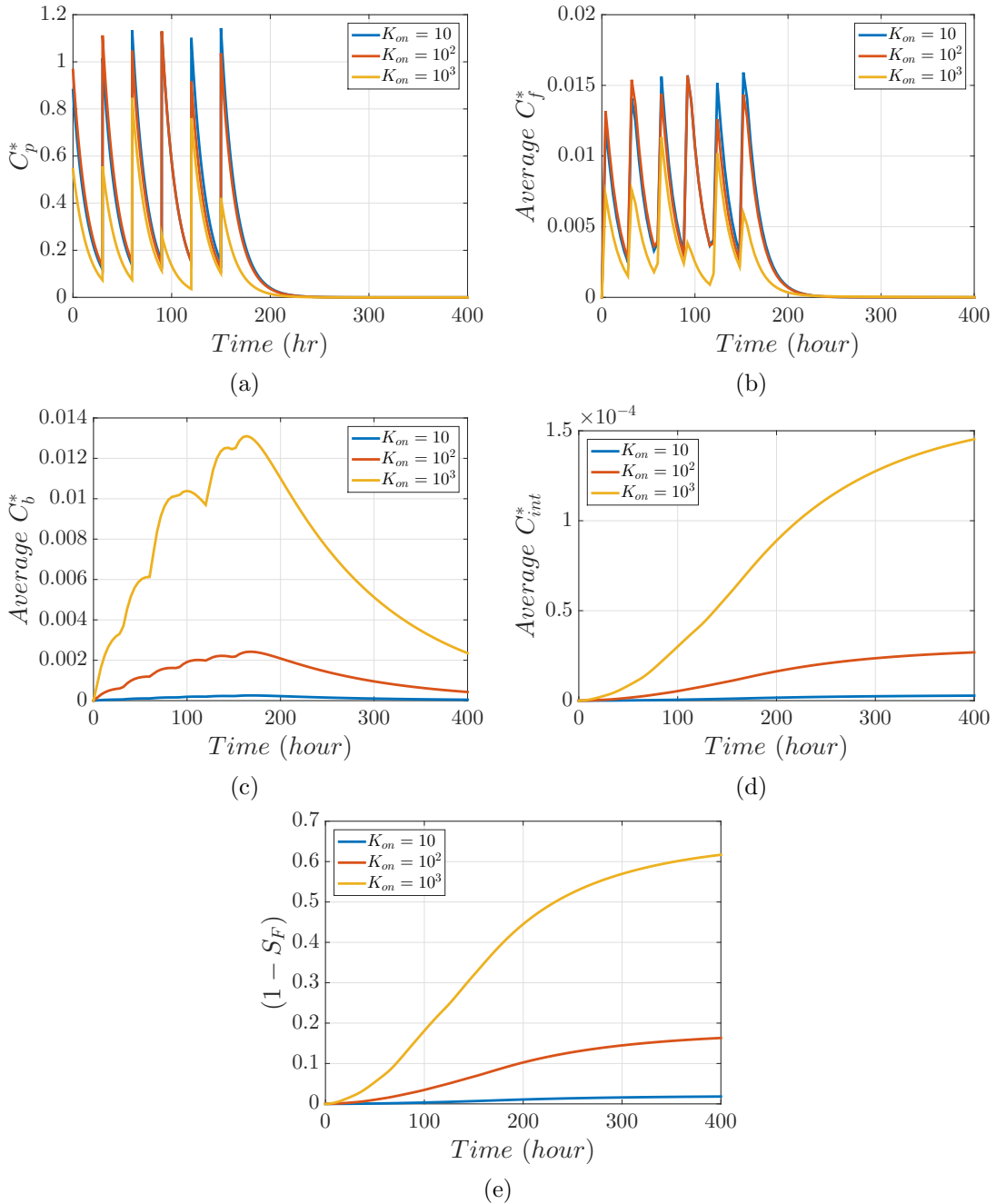


Figure 4.9: Results from optimal regimens for different binding rates of therapeutic agents: (a) drug normalized concentration within the plasma, (b) drug normalized concentration within tumor tissue, (d) normalized concentration of the bound drugs, (e) normalized concentration of the internalized drugs, and (f) fraction of killed cancer cells

decreases from  $10^{-4}$  to  $10^{-8}$ . Moreover, the results demonstrate that an increase in the binding rate of drugs slightly reduces the optimal dosages, but significantly increases drug efficacy, with the fraction of killed cancer cells increasing by 60% when  $K_{on}$  increases from 10 to  $10^3$ . These results concur with the recent experimental study [90] showing that the accumulation of nanoparticles within tumors only weakly depends on the blood half-life but is highly dependent on their bindings with cancer cell receptors.

In this study, the total number of injections and the time interval between them are fixed, however, we suspect that variable time intervals or change in the number of injections may improve drug efficacy for the same tumor microenvironment and drug properties. Moreover, the blood flow complexities within the vascular structure have been ignored here; however, they can affect the distribution of drugs by changing the blood pressure and associated interstitial fluid pressure. This model can be extended further to incorporate these effects and also add more constraints on drug dosages to take into account other important factors such as cancer drug resistance.

#### 4.3.4 Conclusions

One important aspect of chemotherapy effectiveness is to inject the right dosages of therapeutic agents at the right time. These right dosages maximize the eradication of cancer cells but at toxicity levels tolerable by the patient. The distribution of drugs depends on the physiological properties of the tumor microenvironment and drug particle properties; thus, these factors can affect the optimum dosages that should be delivered to a specific patient. Since taking into account most tumor microenvironments and drug properties is not possible thorough clinical and preclinical studies, a mathematical model that incorporates the most effective factors can give helpful insights for designing chemotherapy protocols. In this study, we have developed a computational procedure for finding optimal chemotherapy dosages and personalizing them for delivery to a specific tumor. An image-based approach has been utilized to model the tumor microenvironment. Moreover, the physiological properties of tumor microenvironments, such as vascular permeability, tumor hydraulic conductivity, and the morphology of vasculature, are integrated in our model. Two approaches – bolus injection and continuous infusion – for the delivery of therapeutic agents have been investigated. Results demonstrate that both approaches result in the same efficacy when optimal dosages are injected. Furthermore, drug biophysical properties such as the blood half-life, diffusivity within a tumor, and binding rate with cancer cell receptors have also been investigated to determine their effect on treatment efficacy and optimal dosages. We have demonstrated that even though blood half-life hugely affects optimal dosages, it has a insignificant affect on drug efficacy; whereas the diffusivity and

binding rate of drugs significantly impact their efficacy. This model can be extended further to incorporate more sophisticated cases such those in which the number of injections and the time interval between them are variable.

## 4.4 Case II: Optimal regimen of liposomes

Delivery of liposome drugs has one more consists of one more step than conventional chemotherapy; first, liposomes penetrate through vessel walls and then release their encapsulated therapeutic agents.

### 4.4.1 Methods

Similar to the mathematical modeling for the transport of conventional chemotherapy (Sec. 4.3.1), liposome transport can also be modeled using transport phenomena equations. The penetration of liposome nanoparticles from vascular walls, their transport within the tumor, as well as the release of encapsulated therapeutic agents, their free movement, binding, unbinding and their internalization within cancer cells can be described by the following equations [81, 19]:

- Concentration of liposome nanoparticles within tumor microenvironment:

$$\frac{\partial C_n}{\partial t} + \nabla \cdot (u_i C_n) = \begin{cases} D_n \nabla^2 C_n - K_{rel} C_n + \phi_S & \text{for vasculature} \\ D_n \nabla^2 C_n - K_{rel} C_n & \text{elsewhere} \end{cases} \quad (4.15)$$

- Concentration of free therapeutic agents:

$$\frac{\partial C_f}{\partial t} + \nabla \cdot (u_i C_f) = D_f \nabla^2 C_f + \alpha K_{rel} C_n - \frac{1}{\phi} K_{on} C_e C_f + K_{off} C_b \quad (4.16)$$

- Concentration of therapeutic agents bound to cancer cell receptors:

$$\frac{\partial C_b}{\partial t} = \frac{1}{\phi} K_{on} C_e C_f - (K_{off} + K_{int}) C_b \quad (4.17)$$

- Concentration of internalized therapeutic agents:

$$\frac{\partial C_{int}}{\partial t} = K_{int} C_b \quad (4.18)$$

Table 4.6: Parameter values employed in model equations

Parameter	value	Reference
$D_n$ [ $cm^2/sec$ ]	$7 \times 10^{-8}$	[81]
$K_{rel}$ [ $s^{-1}$ ]	$1 \times 10^{-4}$	[81]
$\phi$	0.08	[82]
$\alpha$	20	[81]

where  $D_n$  is the diffusion coefficient of the liposome nanoparticles and therapeutic agents (drugs);  $C_n$  is the concentration of liposome nanoparticles;  $K_{rel}$  is the rate constant for the release of encapsulated drugs from liposomes; and  $\alpha$  is the number of therapeutic agents encapsulated within each liposome nanoparticle.

Similar to the first case study, Initial and boundary conditions are needed to solve Eq. 4.15, Eq. 4.16, Eq. 4.17, and Eq. 4.18. The concentrations are zero at time zero, just before the first liposome injection:

$$(C_n, C_f, C_b, C_{int})|_{t=0} = 0 \quad (4.19)$$

The boundary conditions for Eq. 4.15 and Eq. 4.16 are, firstly, concentrations are continuous at the boundary ( $\Omega$ ) of tumor and normal tissue, and secondly, concentrations are zero at edges of domain :

$$C_n|_{\Omega^-} = C_n|_{\Omega^+} \quad \text{and} \quad C_f|_{\Omega^-} = C_f|_{\Omega^+} \quad (4.20)$$

$$C_n|_{x=0,L} = C_n|_{y=0,L} = 0 \quad \text{and} \quad C_f|_{x=0,L} = C_f|_{y=0,L} = 0 \quad (4.21)$$

Parameter values used in these equations are listed in Tab. 4.6.

Same optimal regimen method introduced in Sec. 4.3.1 can be applied here to find the best dosages of liposome to be injected. The only difference is that in Eq. 4.13,  $C = (C_n + C_f + C_b + C_{int})$ .

## 4.4.2 Results

To find the optimal dosages to be injected into the tumor microenvironment presented in Fig. 4.1, we assume that the injections happen 6 times, at the consistent time intervals of 30 hours; therefore,  $t_i = \{0, 30, 60, 90, 120, 150\}$ . Since the effect of a drug endures even long after the last injection, it is assumed here that the total treatment time ( $T$ ) is 400 hours. Moreover, we have assumed that that the maximum injected liposome concentration

Table 4.7: The parameter values used in optimization problem

Parameter	value
$T$ [hr]	400
$\Delta t$ [hr]	30
$n$	6
$u_{max}$ [M]	1
$u_{accum}^{max}$ [M.hr]	$1.8925 \times 10^{-4}$

( $u_{max}$ ) is allowed to be 1 to avoid toxicity. When the liposome dosages are injected at the maximum allowable value, the total accumulation of drug within a tumor over a period of treatment is ( $3.78 \times 10^{-4}$ ). To avoid toxicity, it is also assumed that the total drug accumulation over the treatment period must be less than half of ( $3.78 \times 10^{-4}$ ). The summary of parameter values used in this optimization problem are listed in [Tab. 4.7](#). It should be noted that all concentrations presented in this section are normalized to  $u_{max}$ , which is the maximum liposome concentration allowed to be injected.

### Optimal regimen for bolus and continuous infusion strategies

The procedure for finding the optimal regimen presented in [Sec. 4.3.1](#) is applied to two different injection strategies: bolus and continuous infusion. The optimal dosage regimens of liposome nanoparticles for bolus injection were found to be  $u_i = \{0.75, 0.55, 0.63, 0.44, 0.43, 0.19\}$ , and for continuous infusion, to be  $u_i = \{0.98, 0.12, 0, 1, 0.08, 0\}$ . Interestingly, both bolus and continuous infusions result in 34% killed cancer cells within the tumor, meaning that both methods have the same efficacy when optimal drug dosages are used.

For the optimal bolus injections, the spatio-temporal concentration of the liposome nanoparticles, plus the free, bound, and internalized drugs within tumor tissue are shown in [Fig. 4.10](#), [Fig. 4.11](#), [Fig. 4.12](#), and [Fig. 4.13](#), respectively (see also [Video A.5](#)). The spatio-temporal distribution of the fraction of killed cancer cells is also presented in [Fig. 4.14](#) (see also [Video A.5](#)).

The drug concentration within plasma over time and the average concentration values of the liposome nanoparticles, plus the free, bound and internalized drugs, as well as the fraction of killed cancer cells for both bolus and continuous infusion are presented in [Fig. 4.15](#). These figures demonstrate that the concentration of liposome changes similar to liposome concentration within plasma. Moreover, the concentration of liposome nanoparticles within plasma and tumor tissue is almost zero after 200 hours from the beginning of

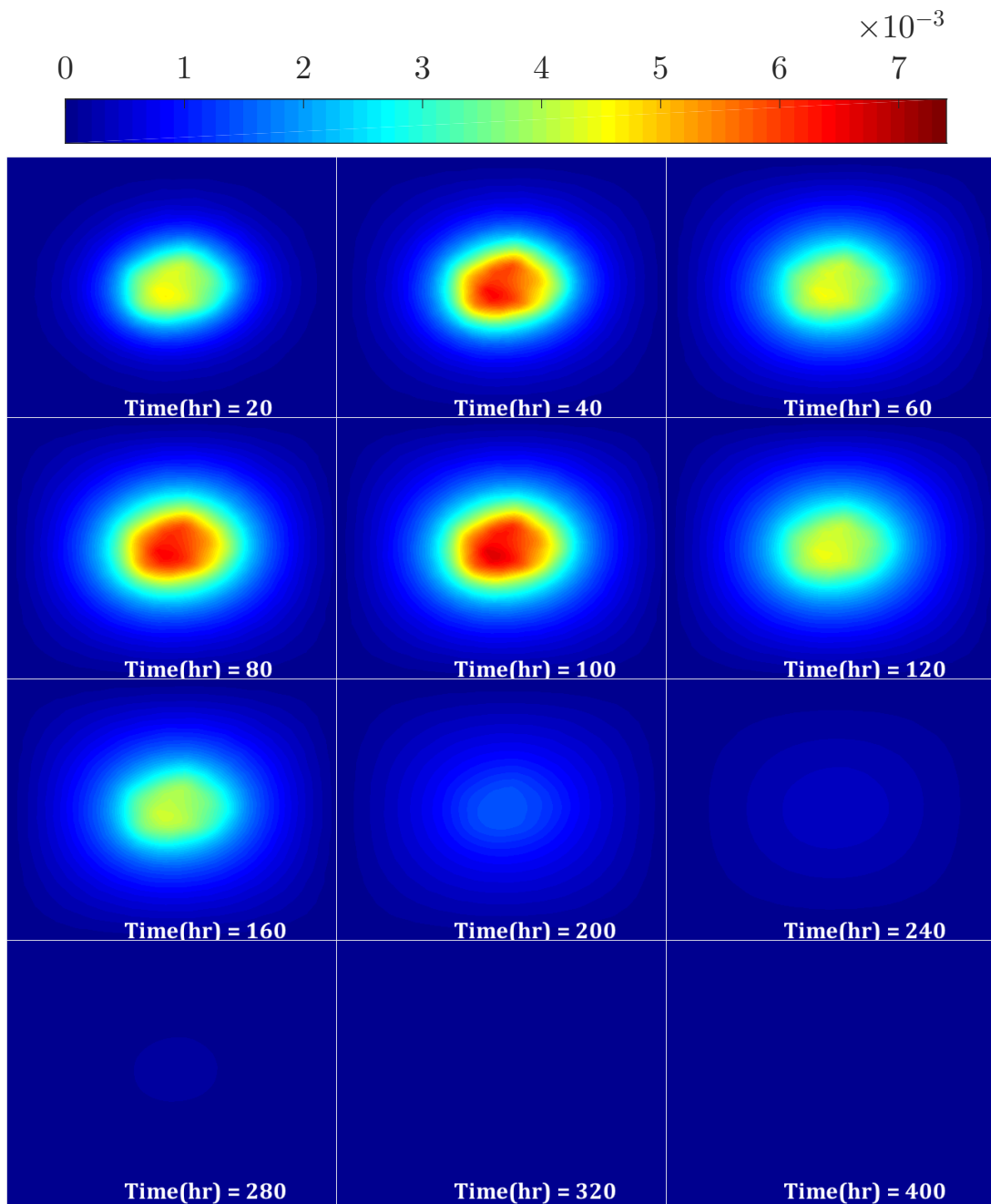


Figure 4.10: Normalized concentration profile of liposome nanoparticles ( $C_n^*$ ) when optimal bolus injections are applied; injection times (*hour*) are  $t_i = \{0, 30, 60, 90, 120, 150\}$ .

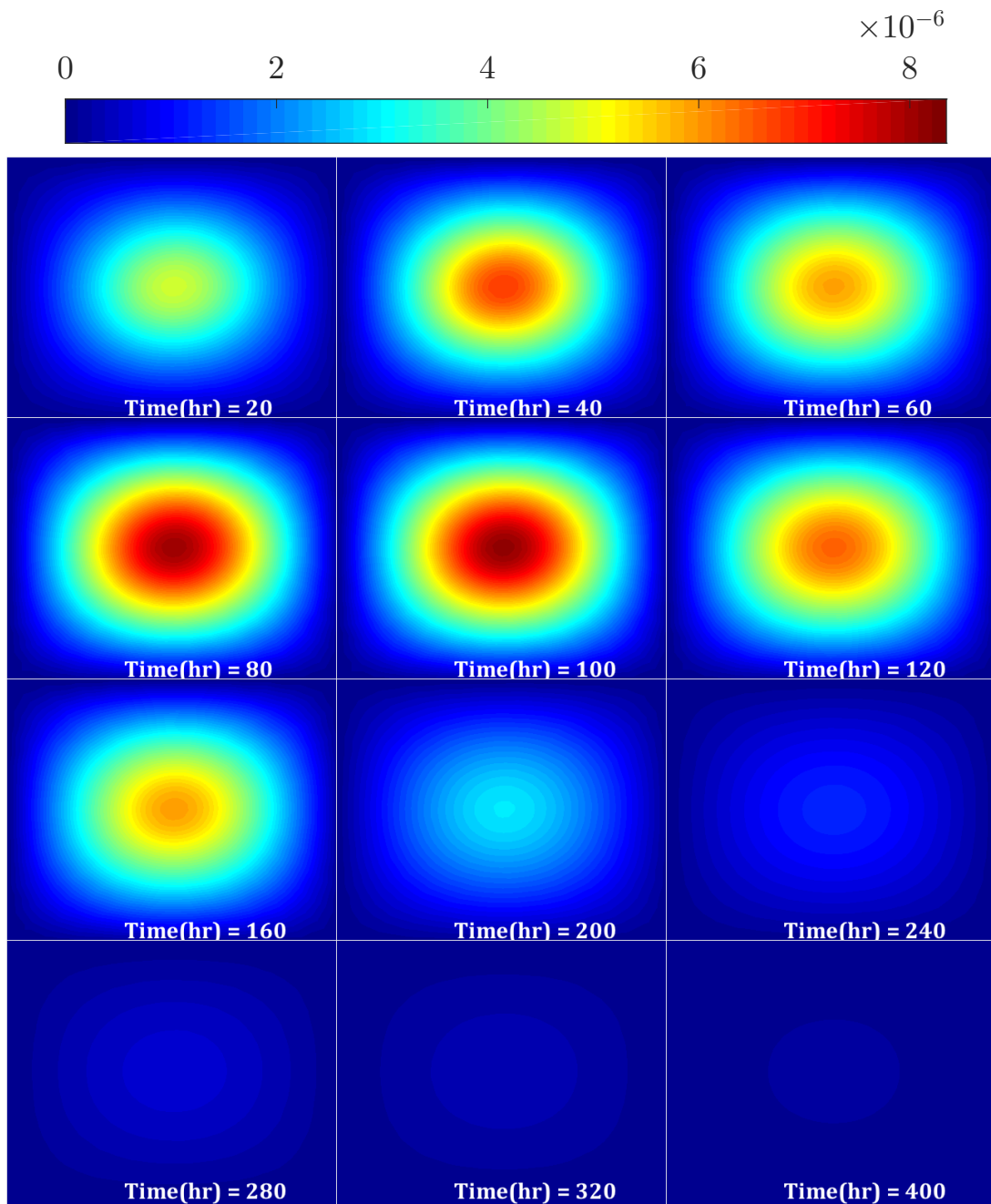


Figure 4.11: Normalized concentration profile of free drugs ( $C_f^*$ ) when optimal bolus injections are applied; injection times (*hour*) are  $t_i = \{0, 30, 60, 90, 120, 150\}$ .

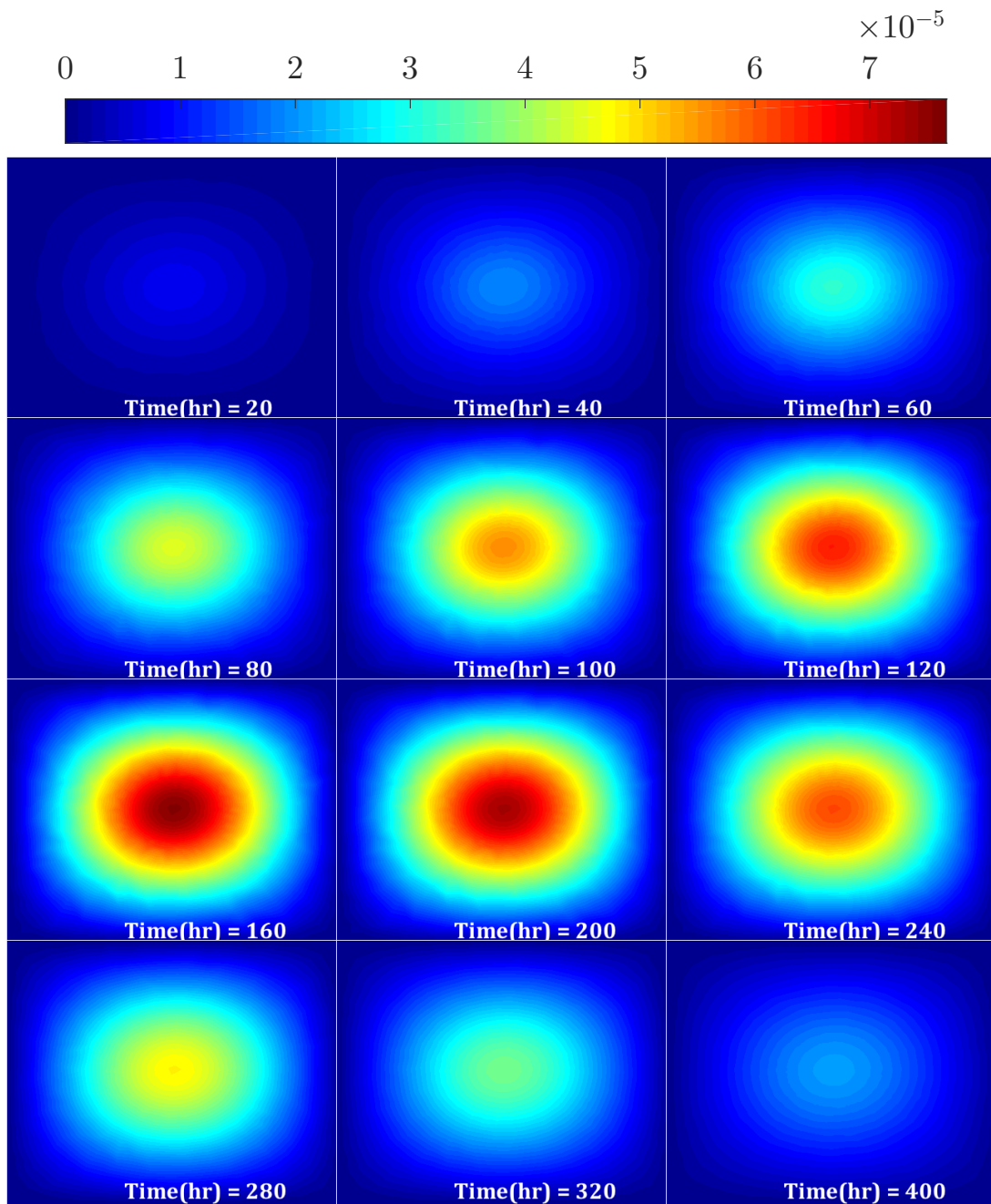


Figure 4.12: Normalized concentration profile of bound drugs ( $C_b^*$ ) when optimal bolus injections are applied; injection times (*hour*) are  $t_i = \{0, 30, 60, 90, 120, 150\}$ .

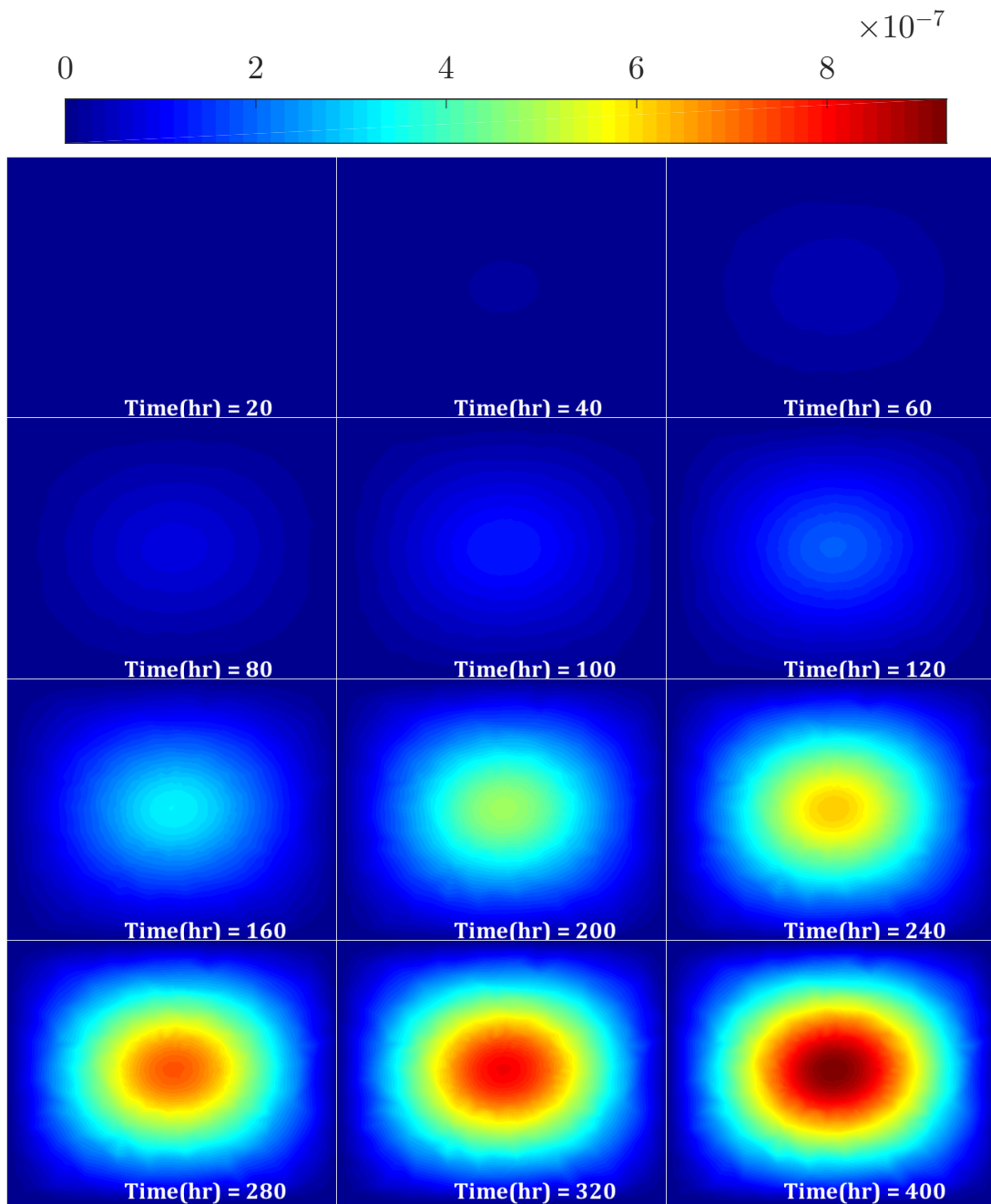


Figure 4.13: Normalized concentration profile of internalized drugs ( $C_{int}^*$ ) when optimal bolus injections are applied; injection times (*hour*) are  $t_i = \{0, 30, 60, 90, 120, 150\}$ .

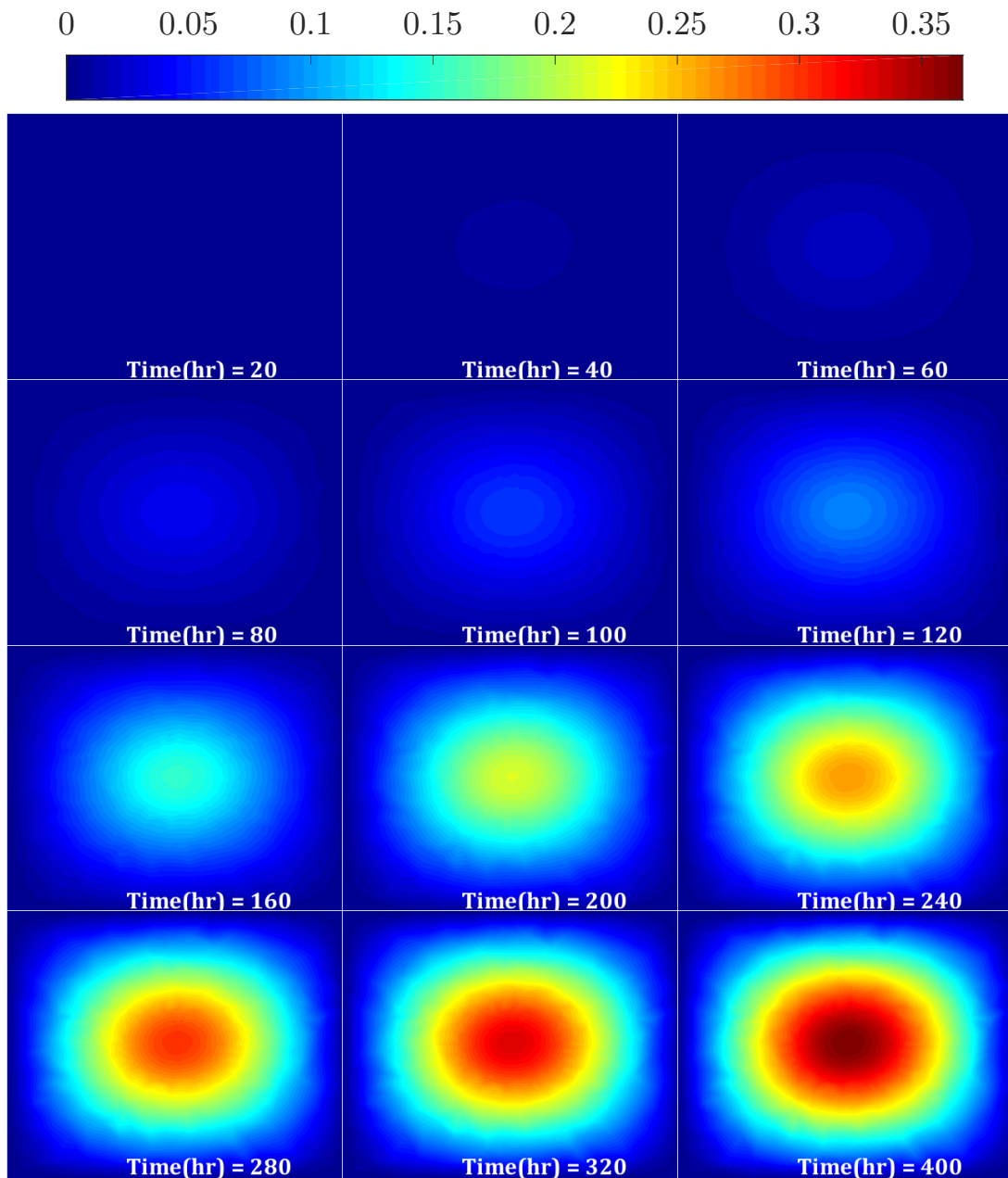


Figure 4.14: The fraction of killed cancer cells ( $1 - S_F$ ) when optimal bolus injections are applied; injection times (*hour*) are  $t_i = \{0, 30, 60, 90, 120, 150\}$ .

treatment. Average concentration values of liposomes ( $C_n^*$ ) and free drugs ( $C_f^*$ ) follow a similar trend; however, the free drug concentration is lower than the liposome concentration by 3 orders of magnitude. Results for bound and internalized concentration reveal that the fluctuation of liposome concentration within plasma are completely damped within the tumor; the bound-drug concentration rises to a maximum after about 200 hours of the first injection, then starts to decline, whereas, the internalized concentration consistently rises. Based on this figure, although the liposome concentrations within the plasma and tumor differ between bolus and continuous infusions, their bound and internalized concentration values are quite similar, resulting in the same efficacy.

### Effect of blood half-life of liposome nanoparticles on optimal regimen

The biophysical properties of liposomes affect how they are distributed in plasma and tumor tissue. Consequently, these properties may influence the dosages that should be applied for highest efficacy. Here, we investigate how blood half-life affects the optimal dosages and the drug efficacy when using bolus injection. The optimal dosages and the resulting fraction of killed cancer cells obtained for different blood half-lives,  $\tau = \{5, 22, 40, 200\}$ , are presented in [Tab. 4.8](#). The average concentration values and the fraction of killed cancer cells over time when the the optimal dosages are applied are also shown in [Fig. 4.16](#). The figure for the liposome concentration within plasma ( $C_p^*$ ) indicates that the optimal regimen results in the highest injected dosages for the liposome with the lowest blood half-life ( $\tau = 5$ ). Moreover, the liposome nanoparticles with the lowest blood half-life ( $\tau = 5$ ) show the lowest concentration values in all forms of drugs (free, bound, internalized), despite their highest injected concentrations. In contrast, the optimal regimen of the liposome with the highest blood half-life ( $\tau = 200$ ) results in the lowest injected concentrations. However, the concentration values associated with the liposome with ( $\tau = 200$ ) arise over time and pass those of liposomes with ( $\tau = 5$ ). [Fig. 4.16](#) indicates that the optimal regimen leads to the highest concentration values within tumors for the liposomes with the blood half-life ( $\tau = 22$ ) and ( $\tau = 40$ ). As a result, these two liposomes show the highest efficacy compared with other cases.

### Effect of diffusivity of liposome nanoparticles on optimal regimen

Another important property of liposome nanoparticles is their diffusivity within tumor tissue. Here, we investigate how the liposome diffusion coefficient affects both treatment efficacy and optimal chemotherapy dosages. The optimal dosages of liposome and the fraction of killed cancer cells at the end of the treatment period for different liposome

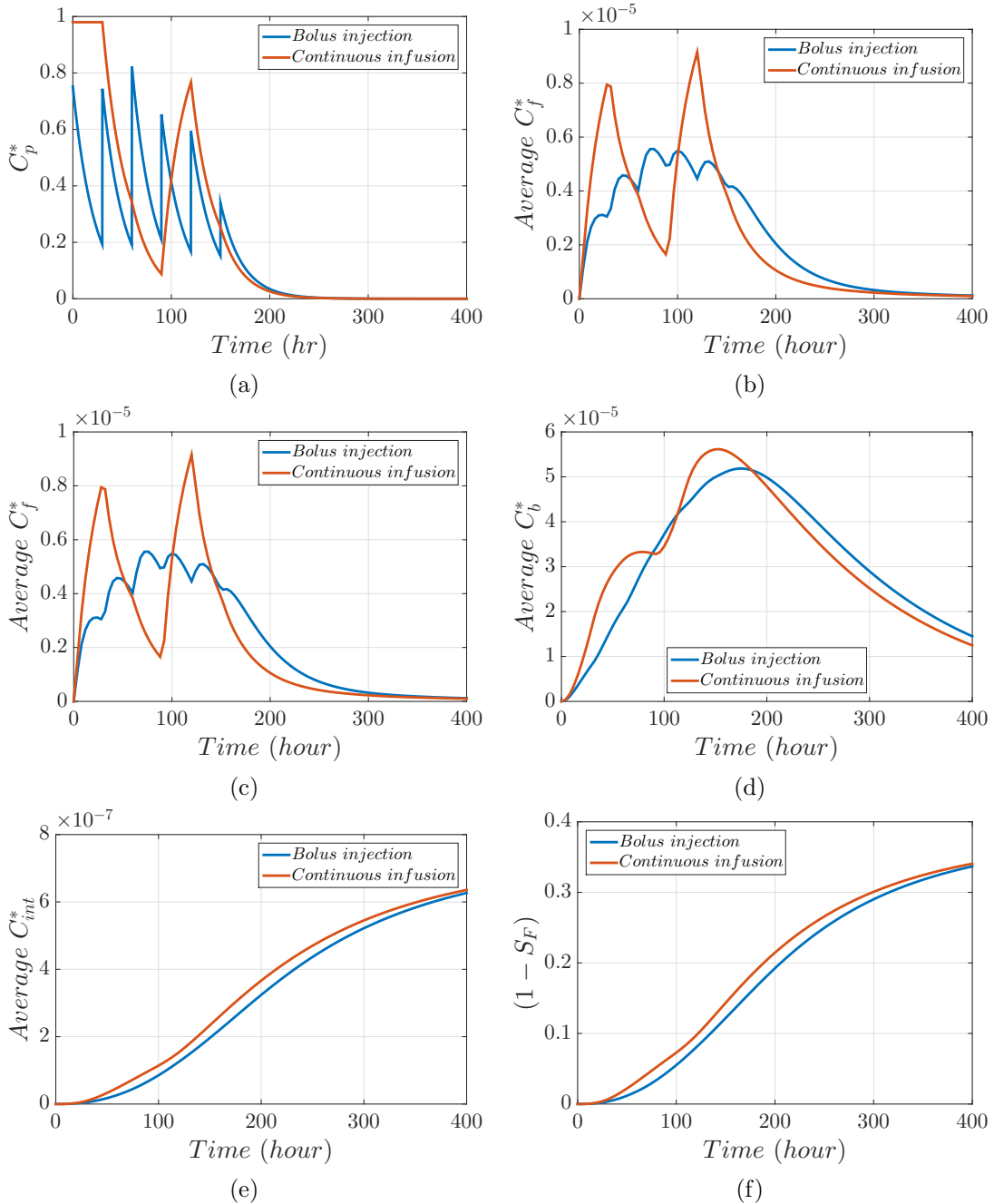


Figure 4.15: Results from optimal regimens for bolus and continuous infusion strategies: (a) liposome concentration within plasma, (b) liposome concentration within tumor tissue, (c) concentration of free drugs, (d) concentration of bound drugs, (e) concentration of internalized drugs, and (f) fraction of killed cancer cells

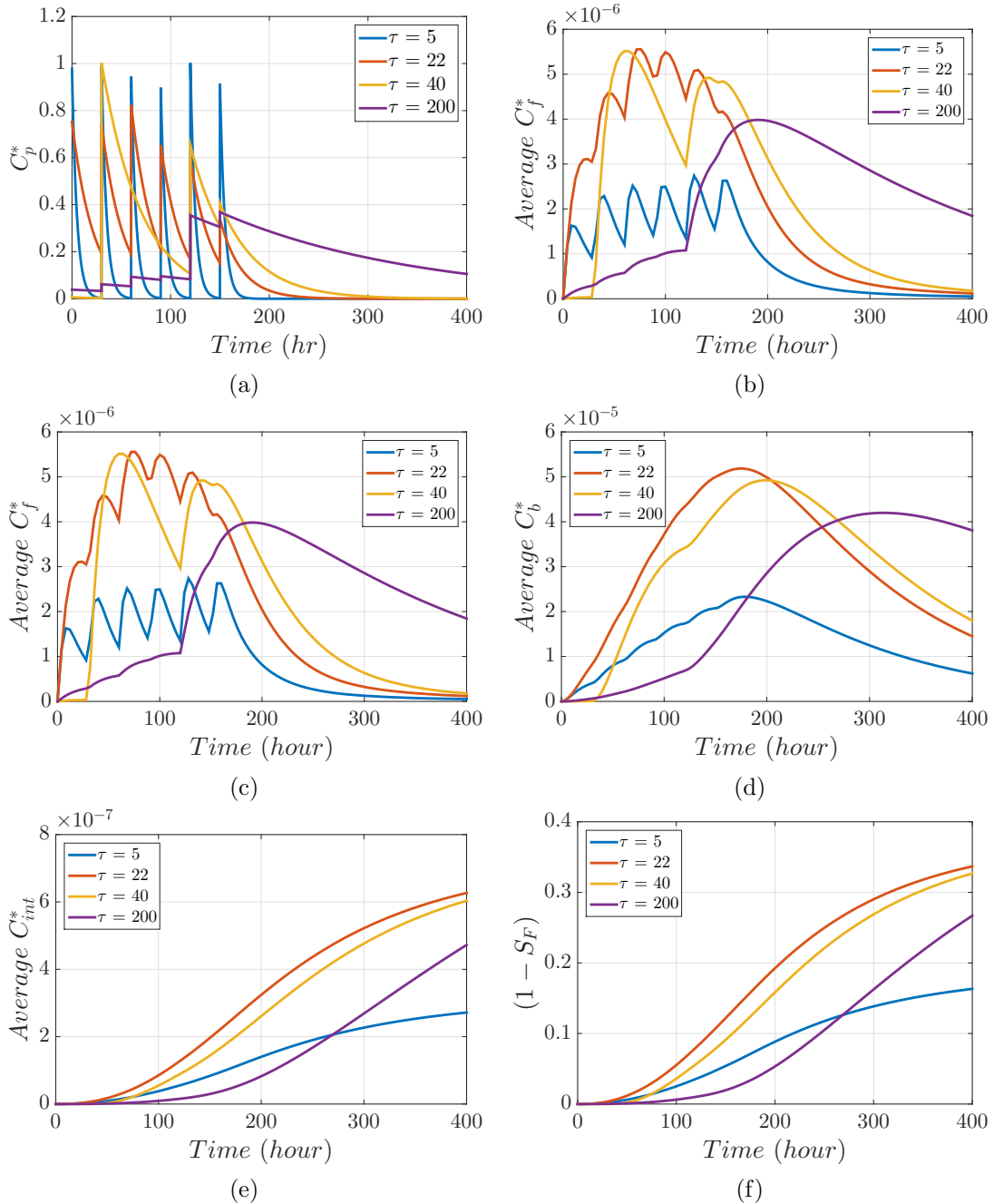


Figure 4.16: Results from optimal regimens for different  $\tau$  values of liposome nanoparticles: (a) liposome normalized concentration within plasma, (b) liposome normalized concentration within tumor tissue, (c) normalized concentration of free drugs, (d) normalized concentration of bound drugs, (e) normalized concentration of internalized drugs, and (f) fraction of killed cancer cells

Table 4.8: The optimal liposome dosages applied for bolus injections for different blood half-life values of drugs

$\tau$	$\{u_i\}_{i=1}^6$	$1 - S_F(T)$
5	{0.98, 0.99, 0.94, 0.89, 1, 0.91}	0.16
22	{0.75, 0.55, 0.63, 0.44, 0.43, 0.19}	0.34
40	{0.006, 1, 0.004, 0, 0.55, 0.10}	0.33
200	{0.04, 0.03, 0.04, 0.02, 0.27, 0.06}	0.27

Table 4.9: The optimal liposome dosages applied for bolus injections for different liposome diffusion coefficients

$D_n$	$\{u_i\}_{i=1}^6$	$1 - S_F(T)$
$1 \times 10^{-9}$	{1, 0.99, 0.96, 0.94, 0.96, 0.94}	0.55
$7 \times 10^{-8}$	{0.75, 0.55, 0.63, 0.44, 0.43, 0.19}	0.34
$1 \times 10^{-5}$	{0.06, 0.12, 0.59, 0.01, 0.21, 0.31}	0.003

diffusion coefficients are presented in [Tab. 4.9](#). The average concentrations and also the fraction of killed cancer cells over time are shown in [Fig. 4.17](#). The plasma concentration profile ( $C_p^*$ ) implies that the optimal regimen suggests the highest injected liposome dosages for the drug with the lowest diffusion coefficient. Moreover, liposome nanoparticles with the highest diffusivity are found to have the lowest concentration within tumor tissue. This low liposome concentration results in very low free, bound and internalized drug concentrations, leading to very low efficacy; while liposome nanoparticles with ( $D_n = 10^{-9}$ ) kill more than 50% of cancer cells, those with ( $D_n = 10^{-5}$ ) eradicate less than 1%.

### 4.4.3 Discussion

We have introduced a computational procedure to find the optimum dosage of liposome nanoparticles to be injected for chemotherapy purposes. Different dosage variables including the number of injections, total treatment period, and different time intervals between each injection, can be investigated using this methodology to find the optimal dosages. Moreover, this method takes into account the physiological properties of tumor microenvironments, such as the hydraulic conductivity of tumor tissue, vascular permeability and morphology, as well as drug nanoparticle properties, including blood half-life and diffusivity.

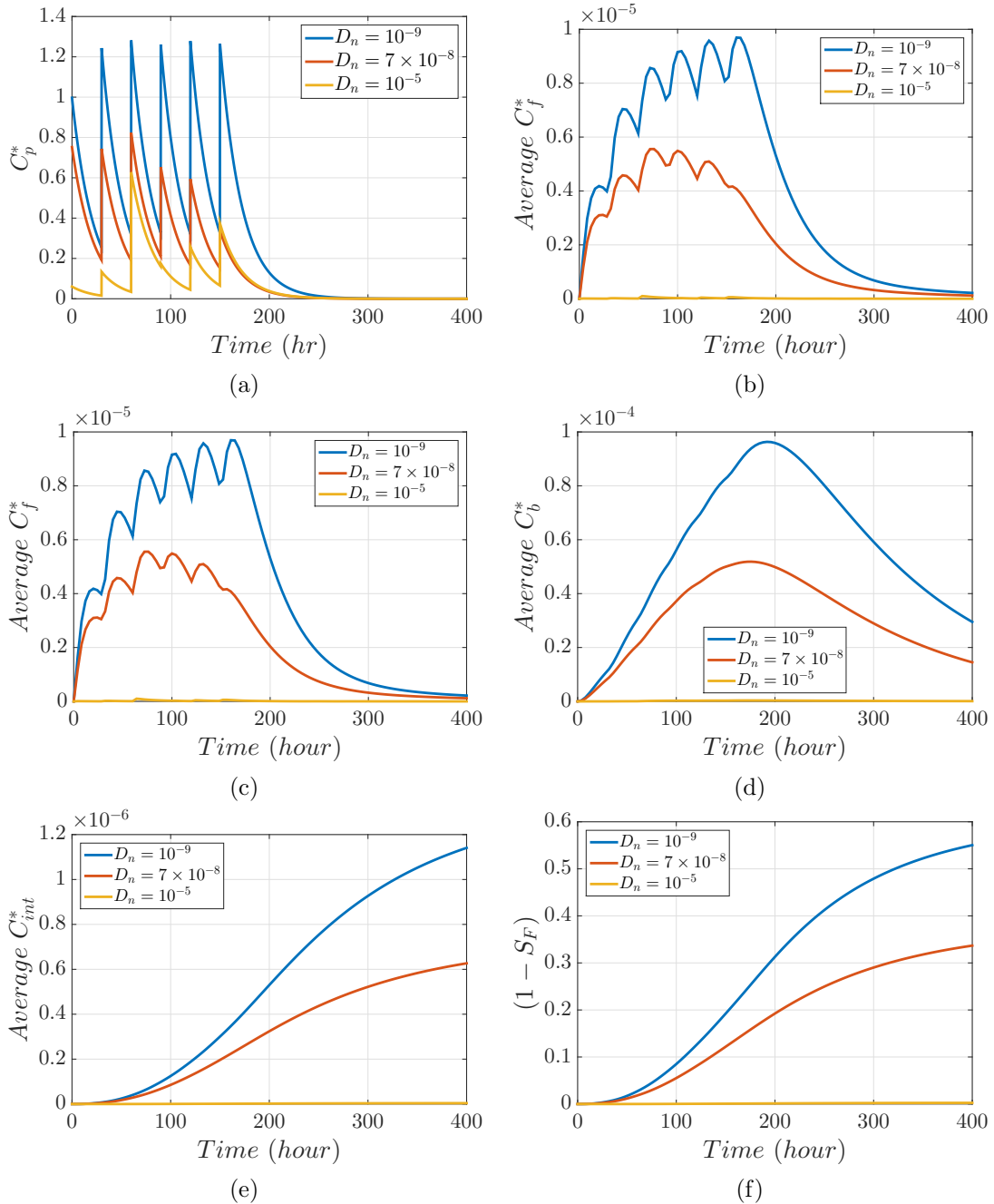


Figure 4.17: Results from optimal regimens for different diffusivity values of liposome nanoparticles: (a) liposome normalized concentration within plasma, (b) liposome normalized concentration within tumor tissue, (c) normalized concentration of free drugs, (d) normalized concentration of bound drugs, (e) normalized concentration of internalized drugs, and (f) fraction of killed cancer cells 83

In this study, we have demonstrated that when bolus injections are applied to a tumor, dosages are in almost in the middle of the acceptable range. In contrast, for continuous infusion, dosages are either close to zero or close to the maximum allowed value. Additionally, although optimal dosages for continuous and bolus injections are different, both lead to the same fraction of killed cancer cells (34%) at the end of the treatment. We also found that a drug's biophysical properties such as the blood half-life and diffusion coefficient affect both optimal dosages and the liposome efficacy. The optimal dosages are highest for the liposome with the lowest blood half-life; liposomes with a low blood half-life clear very fast from the plasma; therefore, higher dosages are required to ensure enough toxicity to kill cancer cells. Although very high dosages are applied for the liposome with the lowest blood half-life, our findings demonstrate that it has the lowest concentration within a tumor. Additionally, [Fig. 4.16](#) reveals that the increase in liposome blood half-life ( $\tau$ ) from 22 to 200 does not improve drug efficacy significantly, a finding that is in agreement with the recent experimental study [90]. In contrast, changes in the diffusion coefficient of liposome nanoparticles significantly affect their concentration distribution within tumors and consequent toxicity to cancer cells ([Fig. 4.17](#)). Liposomes with lower diffusion coefficients stay longer within a tumor, which leads to higher accumulation and also higher chance of their binding to cancer cell receptors and internalization, whereas liposomes with higher diffusivity move faster into surrounding normal tissue, resulting in lower accumulation and efficacy.

In this study, the the number of injections as well as the time intervals between injections were fixed; however, for specific dosages, changes in injection times may improve efficacy. Moreover, increasing or decreasing the number of injections may improve the treatment outcomes. Another limitation of this study is that we have assumed that a perfect high resolution image is provided in which the tumor boundary and vasculature are clearly detectable. However, in most cases, resolution of images is not high enough to detect all capillaries. Therefore before employing the optimal algorithm presented in this study, extra image processing steps are necessary to construct vascular architecture [59, 80]. Finally, the complexities of blood fluid flow within the network of vasculature have been neglected here, although these complexities can affect the transport of fluid and consequently the transport of nanoparticles within tumors.

#### 4.4.4 Conclusions

Many believe that the emergence of personalized treatment will shape the future of medicine. Cancer patients differ in many factors such as tumor type and stage of progress. Even for

the same tumor type, individuals show a variety of tumor microenvironments. One important aspect of personalized treatment is to find the right dosages of drug to be injected at the right times. Here, we have tried to develop a computational basis for finding optimal liposome dosages to apply to a specific patient. This computation algorithm can be applied to a high resolution tumor image taken from the patient. Moreover, our algorithm is personalized to incorporate physiological properties of tumor microenvironments such as the shape and size, and vascular structure of the tumor and the compactness level of cancer cells. Additionally, the algorithm takes into account the parameters that are related to the liposome nanoparticles and encapsulated drugs particles. We have shown that liposome nanoparticle properties such as diffusivity can have a significant impact on drug effectiveness, whereas nanoparticle blood half-life had a negligible effect. Moreover, our findings show that although different injection strategies result in different liposome dosages, these strategies lead to an identical efficacy when drugs are applied in their optimal dosages. Drug toxicity is integrated into our model, but some other important aspects of treatment such as cancer drug resistance, which some believe to be related to the drug dosage, are not included. To develop a more-precise model, the complexity of blood flow in tumor vascular networks can also be incorporated.

# Chapter 5

## Summary and Future Works

### 5.1 Summary

An idealized image-based approach was introduced in this study to investigate the transport of therapeutic agents and the effect of tumor microenvironment physiological properties on fluid flow and drug delivery. We also introduced an approach for finding the optimal dosages of liposome nanoparticles and determining the effect of nanoparticle properties on the optimal dosages.

In [Ch. 2](#), we introduced the computational framework for modeling tumor microenvironments, including their vascular network, fluid flow and macromolecule transportation. Simulation results prove that three factors affect drug distribution in solid tumors: the biophysical properties of drugs, and physiological properties of both the tumor tissue and vasculature. To investigate the interplay of these factors during transport of drug molecules, a tumor and its neighbouring tissue, including the vascular network were modelled, and then fluid flow equations and mass transport equations were derived and simulated. The tumor microenvironment was modelled by incorporating different physiological features such as tumor growth over time, angiogenesis at the tumor periphery, collapse of vessels inside the tumor and vessel dilation. The resulting vascular network reproduces important features of the tumor microenvironment, observed in experimental studies: a regular network in neighbouring normal tissue, an irregular network in the solid tumor, a high density of vasculature at the tumor periphery, and a few thick vessels inside the solid tumor. Experimental studies show that the elevated Interstitial Fluid Pressure (IFP) is the main barrier to drug delivery and causes a heterogenous distribution of drugs. To address the effect of IFP on drug delivery, numerical simulation of the fluid flow in a solid

tumor surrounded by normal tissue was implemented. This simulation demonstrated that the maximum IFP is at the maximum microvascular density inside the tumor. Analyzing parameters of transport equations have proven that the physiological properties of the tumor tissue and vasculature significantly affect IFP. Higher hydraulic conductivity of tumor tissue leads to lower IFP and consequently better drug transportation in tumor tissue. Furthermore, the advection-diffusion equation coupled with a continuity equation, Darcy's law, and Starling's equation were simulated to discover the transportation mechanisms of drug molecules. Two case studies were implemented, drug continuous injection and one time injection (bolus injection). Numerical simulation proved a heterogeneous distribution of drug concentration due to the IFP and heterogeneous vascular structure. This simulation also shows a strong correlation between vascular morphology and drug concentration profile. Furthermore, results demonstrate that the drug residence time, arising from the shape and size of the drug, changes drug effectiveness in killing cancer cells. A higher residence time of drug molecules results in a smaller clearance time by the blood flow, and consequently higher effectiveness against cancer cells. In addition to drug properties, the effects of physiological properties of tumor tissue and vasculature on drug concentration distribution were investigated.

In [Ch. 3](#), we have further extended the method presented in [Ch. 2](#), to calculate IFP and drug delivery within an image of a tumor microenvironment model. The IFP in a very general tumor microenvironment surrounded by normal tissue was calculated in [Ch. 3](#). We found that an increase in microvascular density (MVD) leads to elevated IFP, a result in agreement with experimental studies. For a constant MVD, tumor size affects IFP values, and increased tumor size results in IFP elevation. Furthermore, IFP distribution is correlated with the vascular network structure, and the maximum of IFP occurs at the region with the highest MVD. This observation generalizes the results of previous studies for a solid tumor with a homogenous vascular structure, in which the maximum IFP occurs at the tumor center. Although the vascular morphology affects the IFP distribution within the tumor, the average value of IFP within the tumor is constant for tumors with constant MVD but different vessel locations. We have also introduced a general framework for calculating the spatio-temporal distribution of therapeutic agents in an ideal tumor image model, which can come from a high resolution image. We found a high correlation between the early post-injection concentration profile of drugs and vascular structure. Furthermore, the effect of MVD, tumor size, and vascular location on drug distribution were investigated. High MVD and bigger tumor size were found to increase drug accumulation within the tumor a few hours after injection but result in fast depletion afterwards, when compared with tumors with smaller size or low MVD. Additionally, tumors with more uniformly distributed vessels were found to have more uniformly distributed drugs. Moreover drug

particles stay longer within the interstitium of those tumors.

To find the right drug dosages to apply to a specific patient at the right time, an optimal chemotherapy regimen procedure was developed in [Ch. 4](#). The goal was to find a series of drug dosages that maximize the fraction of killed cancer cells while not exceeding a toxicity level acceptable to the patient under treatment. The model developed in this chapter incorporates the physiological properties of tumor microenvironment as well as drug biophysical properties. Two injection strategies, bolus injection and continuous infusion, were investigated. We found that although the optimal procedure results in completely different dosages for these injection strategies, both lead to the same efficacy at the end of treatment. Investigation of liposome and drug biophysical properties proved that the blood half-life of drugs changes the optimal dosages drastically, however, change in their efficacy was insignificant at the end of treatment. In contrast, the diffusivity of drug and liposome nanoparticles as well as the binding rate of drugs with cancer cell receptors significantly affect treatment efficacy; increased drug binding rate for drugs and decreased diffusivity of drugs and liposomes substantially increase efficacy.

## 5.2 Limitations

Although our computational framework can be applied to a wide range of tumors, several assumptions were made to simplify the problem. The limitation of the methods presented in this work are:

- In all presented models, tumor microenvironment is considered as a 2-D model, while real tumors are 3-D.
- Blood fluid in vasculature is assumed Newtonian, however, the presence of red blood cells makes blood fluid non-Newtonian
- Tumor image is assumed to be ideal, which means the tumor boundary and vascular network are completely detectable. In real images, however, often capillaries cannot be detected very well.
- The blood pressure within tumor image models is considered to be constant. Although, in real tumors, the fluctuation of blood fluid and the random pattern of vascular network result in a very complex blood pressure distribution.

## 5.3 Future work

The main goal of future study of this research is to extend the optimal drug regimen algorithm to incorporate more complex case studies and also extend the idealized image-based tumor model to cover the following gaps in the literature:

- Image-based algorithms used in this study were based on the assumption that a perfect image of a tumor and its microenvironment is available. Although the direction of new imaging techniques makes this assumption true for the near future, most available tumor images are not of high enough resolution to clearly present capillaries and tiny vasculature. Therefore, it is necessary to develop an algorithm that can reconstruct vascular structures. This algorithm should be able to recognize vessels and their connections to other vessels. Furthermore, it should predict the most probable missing vessels and the whole vascular architecture in 2D and 3D.
- More complexity of the tumor microenvironment can be investigated in future studies. Changes in blood vessel diameters along the vascular network, the effect of blood rheology and red blood cells on interstitial fluid pressure (IFP) and on drug delivery, changes in blood viscosity, and fluctuation of blood flow within vascular network can be further investigated. Additionally, a model can be built to merge these phenomena with a real image to accurately predict the transport of drug nanoparticles within a solid tumor.
- The optimal chemotherapy regimen algorithm presented in this study can be further extended to integrate the following complexities:
  - Being able to vary the time interval between injections may improve the chemotherapy outcome. The algorithm can be extended to include the injection times and number of injections as decision variables, to find the best timings and dosages to maximize drug efficacy
  - Drug resistance is one of the crucial problems in drug delivery, and many believe that it might be related to drug concentration and time of exposure. A model for cancer drug resistance can be incorporated in the presented optimal algorithm to determine the most efficient drug regimens.
  - A combination of drugs is usually used for chemotherapy, these may have different toxicities, with different limitations. Our algorithm can be extended to take into account situations where multiple drugs are presented to a patient.

- A tumor microenvironment has a multiscale nature, and a genotype of solid tumors affects cell-signalling of cancerous cells, and conversely, cell-signalling dictates special features in the tumor microenvironment. IFP as a macroscopic phenomena may change the signalling of cells through the shear and normal stresses exerting on cancerous cells. A multiscale model that incorporates cellular interactions and macroscopic features such as elevated IFP can be developed.
- Anti-angiogenesis drugs block VEGF factors secreted by tumor cells and consequently change the vascular structure of the solid tumors over time. One strategy for treating cancer patients is to use the combination of chemotherapy and anti-angiogenesis drugs. A dynamic model can be constructed to incorporate the remodeling of the vascular network when exposed to anti-angiogenesis drugs and also the transport of therapeutic agents within this dynamic microenvironment. This model can help to provide a better understanding of anti-angiogenesis effects and to help a better decision-making about the optimal timings and dosages of anti-angiogenesis and therapeutic drugs.

# APPENDICES

# Appendix A

## Videos from Simulation Results

This chapter includes videos showing the spatio-temporal distributions of drugs for different tumor microenvironments presented in this document <sup>1</sup>.

Video A.1: This video shows the distribution of drug macromolecules over 72 hours (corresponds to [Fig. 3.1](#) and [Fig. 3.4](#)).

---

<sup>1</sup>**Note:** To play these videos, this document must be opened by **Adobe Acrobat** on a computer with installed **Adobe Flash Player**.

(a)

(b)

(c)

(d)

Video A.2: These videos show the concentration distribution of drug macromolecules for tumors with different sizes (correspond to [Fig. 3.10](#) and [Fig. 3.13](#))

(a)

(b)

(c)

Video A.3: These videos show the concentration distribution of drug macromolecules for tumors with different vessel locations (correspond to [Fig. 3.14](#) and [Fig. 3.17](#))

(a)

(b)

(c)

(d)

Video A.4: These videos show the spatio-temporal normalized concentration distribution of (a) free drugs, (b) bound drugs, and (c) internalized drugs, as well as (d) fraction of killed cancer cells (correspond to [Fig. 4.2](#), [Fig. 4.3](#), [Fig. 4.4](#), and [Fig. 4.5](#)).

(a)

(b)

(c)

(d)

(e)

Video A.5: These videos show the spatio-temporal normalized concentration distribution of (a) liposome nanoparticles, (b) free drugs, (c) bound drugs, and (d) internalized drugs, as well as (e) fraction of killed cancer cells. (correspond to [Fig. 4.10](#), [Fig. 4.11](#), [Fig. 4.12](#), [Fig. 4.13](#), and [Fig. 4.14](#))

# References

- [1] Noura Al Moubayed, Andrei Petrovski, and John McCall. Multi-objective optimisation of cancer chemotherapy using smart pso with decomposition. In *Computational Intelligence in Multicriteria Decision-Making (MDCM), 2011 IEEE Symposium on*, pages 81–88. IEEE, 2011.
- [2] Alexander RA Anderson and MAJ Chaplain. Continuous and discrete mathematical models of tumor-induced angiogenesis. *Bulletin of mathematical biology*, 60(5):857–899, 1998.
- [3] James W Baish, Triantafyllos Stylianopoulos, Ryan M Lanning, Walid S Kamoun, Dai Fukumura, Lance L Munn, and Rakesh K Jain. Scaling rules for diffusive drug delivery in tumor and normal tissues. *Proceedings of the National Academy of Sciences*, 108(5):1799–1803, 2011.
- [4] Kathryn Ballard and William Perl. Osmotic reflection coefficients of canine subcutaneous adipose tissue endothelium. *Microvascular research*, 16(2):224–236, 1978.
- [5] Laurence T Baxter and Rakesh K Jain. Transport of fluid and macromolecules in tumors. i. role of interstitial pressure and convection. *Microvascular research*, 37(1):77–104, 1989.
- [6] Laurence T Baxter and Rakesh K Jain. Transport of fluid and macromolecules in tumors. ii. role of heterogeneous perfusion and lymphatics. *Microvascular research*, 40(2):246–263, 1990.
- [7] Laurence T Baxter and Rakesh K Jain. Transport of fluid and macromolecules in tumors: iii. role of binding and metabolism. *Microvascular research*, 41(1):5–23, 1991.

- [8] Laurence T Baxter and Rakesh K Jain. Transport of fluid and macromolecules in tumors. iv. a microscopic model of the perivascular distribution. *Microvascular research*, 41(2):252–272, 1991.
- [9] Y Boucher, L T Baxter, and R K Jain. Interstitial pressure gradients in tissue-isolated and subcutaneous tumors: implications for therapy. *Cancer Res*, 50(15):4478–84, Aug 1990.
- [10] Yves Boucher and Rakesh K Jain. Microvascular pressure is the principal driving force for interstitial hypertension in solid tumors: implications for vascular collapse. *Cancer research*, 52(18):5110–5114, 1992.
- [11] ROBERT A Brace and ARTHUR C Guyton. Interaction of transcapillary starling forces in the isolated dog forelimb. *American Journal of Physiology-Heart and Circulatory Physiology*, 233(1):H136–H140, 1977.
- [12] Timothy Browder, Catherine E Butterfield, Birgit M Kräling, Bin Shi, Blair Marshall, Michael S OReilly, and Judah Folkman. Antiangiogenic scheduling of chemotherapy improves efficacy against experimental drug-resistant cancer. *Cancer research*, 60(7):1878–1886, 2000.
- [13] Richard H Byrd, Robert B Schnabel, and Gerald A Shultz. Approximate solution of the trust region problem by minimization over two-dimensional subspaces. *Mathematical programming*, 40(1-3):247–263, 1988.
- [14] HM Byrne and MAJ Chaplain. Mathematical models for tumour angiogenesis: numerical simulations and nonlinear wave solutions. *Bulletin of Mathematical Biology*, 57(3):461–486, 1995.
- [15] Yan Cai, Shixiong Xu, Jie Wu, and Quan Long. Coupled modelling of tumour angiogenesis, tumour growth and blood perfusion. *Journal of Theoretical Biology*, 279(1):90–101, 2011.
- [16] Peter Carmeliet and Rakesh K Jain. Angiogenesis in cancer and other diseases. *Nature*, 407(6801):249–257, 2000.
- [17] Peter Carmeliet and Rakesh K Jain. Principles and mechanisms of vessel normalization for cancer and other angiogenic diseases. *Nature reviews Drug discovery*, 10(6):417–427, 2011.

- [18] Mark AJ Chaplain and AM Stuart. A model mechanism for the chemotactic response of endothelial cells to tumour angiogenesis factor. *Mathematical Medicine and Biology*, 10(3):149–168, 1993.
- [19] Vikash P Chauhan, Triantafyllos Stylianopoulos, John D Martin, Zoran Popović, Ou Chen, Walid S Kamoun, Mounqi G Bawendi, Dai Fukumura, and Rakesh K Jain. Normalization of tumour blood vessels improves the delivery of nanomedicines in a size-dependent manner. *Nat Nanotechnol*, 7(6):383–8, Jun 2012.
- [20] S E Clare, F Nakhlis, and J C Panetta. Molecular biology of breast cancer metastasis. the use of mathematical models to determine relapse and to predict response to chemotherapy in breast cancer. *Breast Cancer Res*, 2(6):430–5, 2000.
- [21] David G Covell, Jacques Barbet, Oscar D Holton, Christopher DV Black, RJ Parker, and John N Weinstein. Pharmacokinetics of monoclonal immunoglobulin g1, f (ab ) 2, and fab in mice. *Cancer research*, 46(8):3969–3978, 1986.
- [22] Jack L Crosby et al. *Computer simulation in genetics*. 1973.
- [23] FE Curry, VH Huxley, and IH Sarelius. *Techniques in the microcirculation: measurement of permeability, pressure and flow*. Elsevier Science, 1983.
- [24] Balázs Döme, Mary JC Hendrix, Sándor Paku, József Tóvári, and József Tímár. Alternative vascularization mechanisms in cancer: Pathology and therapeutic implications. *The American journal of pathology*, 170(1):1–15, 2007.
- [25] Balázs Döme, Sándor Paku, Beáta Somlai, and József Tímár. Vascularization of cutaneous melanoma involves vessel co-option and has clinical significance. *The Journal of pathology*, 197(3):355–362, 2002.
- [26] D C Drummond, O Meyer, K Hong, D B Kirpotin, and D Papahadjopoulos. Optimizing liposomes for delivery of chemotherapeutic agents to solid tumors. *Pharmacol Rev*, 51(4):691–743, Dec 1999.
- [27] Michael Dunne, Jinzi Zheng, Joshua Rosenblat, David A Jaffray, and Christine Allen. Apn/cd13-targeting as a strategy to alter the tumor accumulation of liposomes. *J Control Release*, 154(3):298–305, Sep 2011.
- [28] Alberto dOnofrio, Urszula Ledzewicz, Helmut Maurer, and Heinz Schättler. On optimal delivery of combination therapy for tumors. *Mathematical biosciences*, 222(1):13–26, 2009.

- [29] Sandra N Ekdawi, James MP Stewart, Michael Dunne, Shawn Stapleton, Nicholas Mitsakakis, Yannan N Dou, David A Jaffray, and Christine Allen. Spatial and temporal mapping of heterogeneity in liposome uptake and microvascular distribution in an orthotopic tumor xenograft model. *Journal of Controlled Release*, 207:101–111, 2015.
- [30] Kyrre E Emblem, Kim Mouridsen, Atle Bjornerud, Christian T Farrar, Dominique Jennings, Ronald J H Borra, Patrick Y Wen, Percy Ivy, Tracy T Batchelor, Bruce R Rosen, Rakesh K Jain, and A Gregory Sorensen. Vessel architectural imaging identifies cancer patient responders to anti-angiogenic therapy. *Nat Med*, 19(9):1178–83, Sep 2013.
- [31] David B Fogel. Evolutionary computation. the fossil record. selected readings on the history of evolutionary algorithms. *New York: The Institute of Electrical and Electronic Engineers*, 1998.
- [32] Judah Folkman. Angiogenesis: an organizing principle for drug discovery? *Nat Rev Drug Discov*, 6(4):273–86, Apr 2007.
- [33] Peter Fraisl, Massimiliano Mazzone, Thomas Schmidt, and Peter Carmeliet. Regulation of angiogenesis by oxygen and metabolism. *Dev Cell*, 16(2):167–79, Feb 2009.
- [34] Alex Fraser, Donald Burnell, et al. Computer models in genetics. *Computer models in genetics.*, 1970.
- [35] DAI Fukumura, Dan G Duda, Lance L Munn, and Rakesh K Jain. Tumor microvasculature and microenvironment: Novel insights through intravital imaging in pre-clinical models. *Microcirculation*, 17(3):206–225, 2010.
- [36] Y C Fung. Stochastic flow in capillary blood vessels. *Microvasc Res*, 5(1):34–48, Jan 1973.
- [37] G Gasparini, N Weidner, S Maluta, F Pozza, P Boracchi, M Mezzetti, A Testolin, and P Bevilacqua. Intratumoral microvessel density and p53 protein: correlation with metastasis in head-and-neck squamous-cell carcinoma. *Int J Cancer*, 55(5):739–44, Nov 1993.
- [38] Leonard E Gerlowski and Rakesh K Jain. Microvascular permeability of normal and neoplastic tissues. *Microvascular research*, 31(3):288–305, 1986.

- [39] Ralf Gdde and Haymo Kurz. Structural and biophysical simulation of angiogenesis and vascular remodeling. *Developmental Dynamics*, 220(4):387–401, 2001.
- [40] Shom Goel, Dan G Duda, Lei Xu, Lance L Munn, Yves Boucher, Dai Fukumura, and Rakesh K Jain. Normalization of the vasculature for treatment of cancer and other diseases. *Physiol Rev*, 91(3):1071–121, Jul 2011.
- [41] C Gondro and BP Kinghorn. A simple genetic algorithm for multiple sequence alignment. *Genetics and Molecular Research*, 6(4):964–982, 2007.
- [42] C H Graham, J Rivers, R S Kerbel, K S Stankiewicz, and W L White. Extent of vascularization as a prognostic indicator in thin ( $\leq 0.76$  mm) malignant melanomas. *Am J Pathol*, 145(3):510–4, Sep 1994.
- [43] K J Harrington, S Mohammadtaghi, P S Uster, D Glass, A M Peters, R G Vile, and J S Stewart. Effective targeting of solid tumors in patients with locally advanced cancers by radiolabeled pegylated liposomes. *Clin Cancer Res*, 7(2):243–54, Feb 2001.
- [44] John M Harrold and Robert S Parker. Clinically relevant cancer chemotherapy dose scheduling via mixed-integer optimization. *Computers & Chemical Engineering*, 33(12):2042–2054, 2009.
- [45] Duane E Hilmas and Edward L Gillette. Morphometric analyses of the microvasculature of tumors during growth and after x-irradiation. *Cancer*, 33(1):103–110, 1974.
- [46] J Holash, P C Maisonpierre, D Compton, P Boland, C R Alexander, D Zagzag, G D Yancopoulos, and S J Wiegand. Vessel cooption, regression, and growth in tumors mediated by angiopoietins and vegf. *Science*, 284(5422):1994–8, Jun 1999.
- [47] J Holash, S J Wiegand, and G D Yancopoulos. New model of tumor angiogenesis: dynamic balance between vessel regression and growth mediated by angiopoietins and vegf. *Oncogene*, 18(38):5356–62, Sep 1999.
- [48] Tord Hompland, Christine Ellingsen, Kanthi Galappathi, and Einar K Rofstad. Dwmri in assessment of the hypoxic fraction, interstitial fluid pressure, and metastatic propensity of melanoma xenografts. *BMC Cancer*, 14:92, 2014.
- [49] Tord Hompland, Kristine Gulliksrud, Christine Ellingsen, and Einar K Rofstad. Assessment of the interstitial fluid pressure of tumors by dynamic contrast-enhanced

- magnetic resonance imaging with contrast agents of different molecular weights. *Acta Oncol*, 52(3):627–35, Apr 2013.
- [50] Trachette L Jackson. *Modeling Tumor Vasculature: Molecular, Cellular, and Tissue Level Aspects and Implications*. Springer, 2012.
- [51] T M Jaeger, N Weidner, K Chew, D H Moore, R L Kerschmann, F M Waldman, and P R Carroll. Tumor angiogenesis correlates with lymph node metastases in invasive bladder cancer. *J Urol*, 154(1):69–71, Jul 1995.
- [52] Rakesh K Jain. Normalization of tumor vasculature: an emerging concept in antiangiogenic therapy. *Science*, 307(5706):58–62, Jan 2005.
- [53] Rakesh K Jain. Normalizing tumor microenvironment to treat cancer: bench to bedside to biomarkers. *J Clin Oncol*, 31(17):2205–18, Jun 2013.
- [54] Rakesh K Jain, Emmanuelle di Tomaso, Dan G Duda, Jay S Loeffler, A Gregory Sorensen, and Tracy T Batchelor. Angiogenesis in brain tumours. *Nat Rev Neurosci*, 8(8):610–22, Aug 2007.
- [55] Rakesh K Jain, Ricky T Tong, and Lance L Munn. Effect of vascular normalization by antiangiogenic therapy on interstitial hypertension, peritumor edema, and lymphatic metastasis: insights from a mathematical model. *Cancer Res*, 67(6):2729–35, Mar 2007.
- [56] Seong Hoon Jang, M Guillaume Wientjes, Dan Lu, and Jessie L-S Au. Drug delivery and transport to solid tumors. *Pharmaceutical research*, 20(9):1337–1350, 2003.
- [57] J Johnson, A Monks, MG Hollingshead, and EA Sausville. Preclinical aspects of cancer drug discovery and development. *Cancer Chemotherapy and Biotherapy. Philadelphia, PA, Lippincott Williams & Wilkins*, pages 17–36, 2001.
- [58] David J Kerr, Anne M Kerr, R Ian Freshney, and Stanley B Kaye. Comparative intracellular uptake of adriamycin and 4'-deoxydoxorubicin by nonsmall cell lung tumor cells in culture and its relationship to cell survival. *Biochemical pharmacology*, 35(16):2817–2823, 1986.
- [59] Eugene Kim, Spyros Stamatelos, Jana Cebulla, Zaver M Bhujwalla, Aleksander S Popel, and Arvind P Pathak. Multiscale imaging and computational modeling of blood flow in the tumor vasculature. *Ann Biomed Eng*, 40(11):2425–41, Nov 2012.

- [60] Eugene S Kim, Anna Serur, Jianzhong Huang, Christina A Manley, Kimberly W McCrudden, Jason S Frischer, Samuel Z Soffer, Laurence Ring, Tamara New, Stephanie Zabski, et al. Potent vegf blockade causes regression of coopted vessels in a model of neuroblastoma. *Proceedings of the National Academy of Sciences*, 99(17):11399–11404, 2002.
- [61] Jeffrey C Lagarias, James A Reeds, Margaret H Wright, and Paul E Wright. Convergence properties of the nelder–mead simplex method in low dimensions. *SIAM Journal on optimization*, 9(1):112–147, 1998.
- [62] Yun Li, Kim Chwee Ng, David J Murray-Smith, Gary J Gray, and Ken C Sharman. Genetic algorithm automated approach to the design of sliding mode control systems. *International Journal of Control*, 63(4):721–739, 1996.
- [63] P Macchiarini, G Fontanini, M J Hardin, F Squartini, and C A Angeletti. Relation of neovascularisation to metastasis of non-small-cell lung cancer. *Lancet*, 340(8812):145–6, Jul 1992.
- [64] R B Martin, M E Fisher, R F Minchin, and K L Teo. Low-intensity combination chemotherapy maximizes host survival time for tumors containing drug-resistant cells. *Math Biosci*, 110(2):221–52, Jul 1992.
- [65] R B Martin, M E Fisher, R F Minchin, and K L Teo. Optimal control of tumor size used to maximize survival time when cells are resistant to chemotherapy. *Math Biosci*, 110(2):201–19, Jul 1992.
- [66] Rebecca J McClaine, Joseph S Giglia, Syed A Ahmad, Stephanie J McCoy, and Jeffrey J Sussman. Quality of life outcomes after isolated limb infusion. *Annals of surgical oncology*, 19(5):1373–1378, 2012.
- [67] M Mohammadi and P Chen. Effect of microvascular distribution and its density on interstitial fluid pressure in solid tumors: A computational model. *Microvasc Res*, Jun 2015.
- [68] Jorge J Moré and Danny C Sorensen. Computing a trust region step. *SIAM Journal on Scientific and Statistical Computing*, 4(3):553–572, 1983.
- [69] Seema Nanda, Helen Moore, and Suzanne Lenhart. Optimal control of treatment in a mathematical model of chronic myelogenous leukemia. *Mathematical biosciences*, 210(1):143–156, 2007.

- [70] P A Netti, L T Baxter, Y Boucher, R Skalak, and R K Jain. Time-dependent behavior of interstitial fluid pressure in solid tumors: implications for drug delivery. *Cancer Res*, 55(22):5451–8, Nov 1995.
- [71] P A Netti, S Roberge, Y Boucher, L T Baxter, and R K Jain. Effect of transvascular fluid exchange on pressure-flow relationship in tumors: a proposed mechanism for tumor blood flow heterogeneity. *Microvasc Res*, 52(1):27–46, Jul 1996.
- [72] K Chwee Ng, Y Li, DJ Murray-Smith, and KC Sharman. Genetic algorithms applied to fuzzy sliding mode controller design. 1995.
- [73] EM Noorda, RHJ van Kreijl, BC Vrouenraets, OE Nieweg, M Muller, BBR Kroon, and NK Aaronson. The health-related quality of life of long-term survivors of melanoma treated with isolated limb perfusion. *European Journal of Surgical Oncology (EJSO)*, 33(6):776–782, 2007.
- [74] JR Pappenheimer, EM Renkin, and LM Borrero. Filtration, diffusion and molecular sieving through peripheral capillary membranes. *Am. J. Physiol*, 167(13):2578, 1951.
- [75] Uma Prabhakar, Hiroshi Maeda, Rakesh K Jain, Eva M Sevick-Muraca, William Zamboni, Omid C Farokhzad, Simon T Barry, Alberto Gabizon, Piotr Grodzinski, and David C Blakey. Challenges and key considerations of the enhanced permeability and retention effect for nanomedicine drug delivery in oncology. *Cancer Res*, 73(8):2412–7, Apr 2013.
- [76] Bengt Rippe, Akira Kamiya, and Björn Folkow. Simultaneous measurements of capillary diffusion and filtration exchange during shifts in filtration-absorption and at graded alterations in the capillary permeability surface area product (ps). *Acta Physiologica Scandinavica*, 104(3):318–336, 1978.
- [77] Einar K Rofstad, Kanthi Galappathi, and Berit S Mathiesen. Tumor interstitial fluid pressure — a link between tumor hypoxia, microvascular density, and lymph node metastasis. *Neoplasia*, 2014.
- [78] Trude G Simonsen, Jon-Vidar Gaustad, Marit N Leinaas, and Einar K Rofstad. High interstitial fluid pressure is associated with tumor-line specific vascular abnormalities in human melanoma xenografts. *PLoS One*, 7(6):e40006, 2012.
- [79] L Simpson-Herren, P E Noker, and S D Wagoner. Variability of tumor response to chemotherapy. ii. contribution of tumor heterogeneity. *Cancer Chemother Pharmacol*, 22(2):131–6, 1988.

- [80] Spyros K Stamatelos, Eugene Kim, Arvind P Pathak, and Aleksander S Popel. A bioimage informatics based reconstruction of breast tumor microvasculature with computational blood flow predictions. *Microvasc Res*, 91:8–21, Jan 2014.
- [81] Triantafyllos Stylianopoulos, Eva-Athena Economides, James W Baish, Dai Fukumura, and Rakesh K Jain. Towards optimal design of cancer nanomedicines: Multi-stage nanoparticles for the treatment of solid tumors. *Ann Biomed Eng*, Feb 2015.
- [82] Triantafyllos Stylianopoulos and Rakesh K Jain. Combining two strategies to improve perfusion and drug delivery in solid tumors. *Proc Natl Acad Sci U S A*, 110(46):18632–7, Nov 2013.
- [83] Triantafyllos Stylianopoulos, John D Martin, Matija Snuderl, Fotios Mpekris, Saloni R Jain, and Rakesh K Jain. Coevolution of solid stress and interstitial fluid pressure in tumors during progression: implications for vascular collapse. *Cancer Res*, 73(13):3833–41, Jul 2013.
- [84] Edward A Swabb, James Wei, and Pietro M Gullino. Diffusion and convection in normal and neoplastic tissues. *Cancer research*, 34(10):2814–2822, 1974.
- [85] G W Swan. Role of optimal control theory in cancer chemotherapy. *Math Biosci*, 101(2):237–84, Oct 1990.
- [86] GEORGE W Swan. Tumor growth models and cancer chemotherapy. *Cancer modeling*, 83:91–179, 1987.
- [87] Melody A Swartz and Mark E Fleury. Interstitial flow and its effects in soft tissues. *Annu Rev Biomed Eng*, 9:229–56, 2007.
- [88] Melody A Swartz, Noriho Iida, Edward W Roberts, Sabina Sangaletti, Melissa H Wong, Fiona E Yull, Lisa M Coussens, and Yves A DeClerck. Tumor microenvironment complexity: emerging roles in cancer therapy. *Cancer Res*, 72(10):2473–80, May 2012.
- [89] Melody A Swartz and Amanda W Lund. Lymphatic and interstitial flow in the tumour microenvironment: linking mechanobiology with immunity. *Nat Rev Cancer*, 12(3):210–9, Mar 2012.
- [90] Edward A Sykes, Juan Chen, Gang Zheng, and Warren C W Chan. Investigating the impact of nanoparticle size on active and passive tumor targeting efficiency. *ACS Nano*, 8(6):5696–706, Jun 2014.

- [91] Lihong V Wang and Song Hu. Photoacoustic tomography: in vivo imaging from organelles to organs. *Science*, 335(6075):1458–62, Mar 2012.
- [92] N Weidner, P R Carroll, J Flax, W Blumenfeld, and J Folkman. Tumor angiogenesis correlates with metastasis in invasive prostate carcinoma. *Am J Pathol*, 143(2):401–9, Aug 1993.
- [93] Noel Weidner. Chapter 14. measuring intratumoral microvessel density. *Methods Enzymol*, 444:305–23, 2008.
- [94] M Welter, K Bartha, and H Rieger. Emergent vascular network inhomogeneities and resulting blood flow patterns in a growing tumor. *Journal of theoretical biology*, 250(2):257–280, 2008.
- [95] M Welter, K Bartha, and H Rieger. Vascular remodelling of an arterio-venous blood vessel network during solid tumour growth. *J Theor Biol*, 259(3):405–22, Aug 2009.
- [96] M Welter and H Rieger. Physical determinants of vascular network remodeling during tumor growth. *Eur Phys J E Soft Matter*, 33(2):149–63, Oct 2010.
- [97] Michael Welter and Heiko Rieger. Interstitial fluid flow and drug delivery in vascularized tumors: a computational model. *PLoS One*, 8(8):e70395, 2013.
- [98] Curt A Wiederhielm. Dynamics of capillary fluid exchange: A nonlinear computer simulation. *Microvascular research*, 18(1):48–82, 1979.
- [99] Jie Wu, Shixiong Xu, Quan Long, Michael W Collins, Carola S König, Gaiping Zhao, Yuping Jiang, and Anwar R Padhani. Coupled modeling of blood perfusion in intravascular, interstitial spaces in tumor microvasculature. *J Biomech*, 41(5):996–1004, 2008.
- [100] Min Wu, Hermann B Frieboes, Mark A J Chaplain, Steven R McDougall, Vittorio Cristini, and John S Lowengrub. The effect of interstitial pressure on therapeutic agent transport: Coupling with the tumor blood and lymphatic vascular systems. *J Theor Biol*, 355:194–207, Aug 2014.
- [101] Min Wu, Hermann B Frieboes, Steven R McDougall, Mark A J Chaplain, Vittorio Cristini, and John Lowengrub. The effect of interstitial pressure on tumor growth: coupling with the blood and lymphatic vascular systems. *J Theor Biol*, 320:131–51, Mar 2013.

- [102] F Yuan, M Leunig, S K Huang, D A Berk, D Papahadjopoulos, and R K Jain. Microvascular permeability and interstitial penetration of sterically stabilized (stealth) liposomes in a human tumor xenograft. *Cancer Res*, 54(13):3352–6, Jul 1994.
- [103] Lin Zhang, Nuo Yang, Jin-Wan Park, Dionyssios Katsaros, Stefano Fracchioli, Gaoyuan Cao, Ann O'Brien-Jenkins, Thomas C Randall, Stephen C Rubin, and George Coukos. Tumor-derived vascular endothelial growth factor up-regulates angiopoietin-2 in host endothelium and destabilizes host vasculature, supporting angiogenesis in ovarian cancer. *Cancer Res*, 63(12):3403–12, Jun 2003.
- [104] Stephen X Zhang and Vladan Babovic. A real options approach to the design and architecture of water supply systems using innovative water technologies under uncertainty. *Journal of Hydroinformatics*, 14(1), 2012.